Charles University in Prague

The First Faculty of Medicine

Study program: Medical Biophysics

UNIVERZITA KARLOVA
1. lékařská fakulta

Mgr. Andrea Gálisová

Alternative methods for visualization of pancreatic islets

Alternativní metody zobrazení pankreatických ostrůvků

Doctoral Thesis

Thesis Supervisor: doc. Ing. Daniel Jirák, PhD.

Thesis Consultant: Mgr. Vít Herynek, PhD.

Prague, 2018

Enclosure

I declare that I prepared the thesis independently and I mentioned all references and literature sources. I also state that the thesis has not been used for obtaining another or similar academic degrees.

I agree with the permanent depository of the thesis in the database Theses.cz for checking the similarity of theses.

Prohlášení

Prohlašuji, že jsem závěrečnou práci zpracovala samostatně a že jsem řádně uvedla a citovala všechny použité prameny a literaturu. Současně prohlašuji, že práce nebyla využita k získání jiného nebo stejného titulu.

Souhlasím s trvalým uložením elektronické verze mé práce v databázi systému meziuniverzitního projektu Theses.cz za účelem soustavné kontroly podobnosti kvalifikačních prací.

In Prague/V Praze …….

Andrea Gálisová

Identification record:

GÁLISOVÁ, Andrea. *Alternative methods for visualization of pancreatic islets [Alternativní metody zobrazení pankreatických ostrůvků]*. Prague, 2018. 127 pages and 7 appendices. Dissertation thesis. Charles University in Prague, The First Faculty of Medicine, Institute for Clinical and Experimental Medicine. Thesis Supervisor Jirák Daniel.

Identifikační záznam:

GÁLISOVÁ, Andrea. *Alternativní metody zobrazení pankreatických ostrůvků [Alternative methods for visualization of pancreatic islets]*. Praha, 2018. 127 stran a 7 příloh. Dizertační práce. Univerzita Karlova, 1. lékařská fakulta, Institut klinické a experimentální medicíny. Vedoucí práce Jirák Daniel.

Abstract

Transplantation of pancreatic islets (PIs) represents an alternative treatment for type 1 diabetes mellitus. Post-transplant monitoring of islets by a reliable imaging method may contribute to the improvement of the transplantation outcome. In this thesis, novel visualization approaches for PIs were tested using magnetic resonance (MR) and optical imaging on phantoms and experimental animals, including Chemical Exchange Saturation Transfer (CEST) MR, fluorine (^{19}F) MR, bioluminescence and fluorescence imaging.

MR imaging based on frequency-selective method CEST was performed on islets labeled with Eu-/Yb-based chelates. Labeled islets possessed low MR signal in phantoms, what would have been unsatisfactory for *in vivo* applications. Moreover, viability and function of labeled islets was impaired reflecting limited applicability of these agents for islet labeling and visualization.

Genetically modified bioluminescent islets showed suitable properties for longitudinal tracking of their post-transplant fate at an artificial transplant site - subcutaneously implanted polymeric scaffolds. Using multimodal imaging (MR and bioluminescence), the optimal timing for transplantation of islets into the scaffolds was assessed in diabetic rats. Islets transplanted into scaffolds using the optimized timing scheme were sufficiently vascularized and functional.

Finally, we developed a trimodal imaging platform for islets transplanted in scaffolds in rats. Bioluminescent islets labeled with multimodal nanoparticles were specifically visualized by ^{19}F MR and sensitively by fluorescence imaging. A correlation between the bioluminescence and the ^{19}F MR signals was found indicating the fast clearance of nanoparticles from the transplantation site after cell death. This finding addresses one of the major issues with intracellular imaging labels and proved that the proposed imaging model is reliable for reflecting the status of transplanted PIs *in vivo*.

Keywords: magnetic resonance imaging, optical imaging, contrast agents, cell labeling, pancreatic islet, transplantation

Abstrakt

Transplantace pankreatických ostrůvků (PIs) představuje alternativní metodu léčby diabetu 1. typu. Monitorování transplantovaných PIs pomocí vhodné zobrazovací metody může přispět k zlepšení výsledků transplantace. V předkládané disertační práci jsme testovali nové způsoby zobrazení PIs pomocí magnetické rezonance (MR) a optického zobrazování, konkrétně MR metodu založenou na přenosu saturace magnetizace přes chemickou výměnu (Chemical Exchange Saturation Transfer - CEST), fluorovou (^{19}F) MR a optické zobrazování.

Frekvenčně selektivní CEST metoda byla použita pro zobrazování PIs značených pomocí dvou CEST kontrastů. Na MR obrazech jsme detekovali pouze slabý signál ze značených ostrůvků, které byly navíc poškozené. Tyto výsledky ukazují, že tento typ kontrastů není vhodný pro značení a zobrazování pankreatických ostrůvků.

V druhém experimentu jsme monitorovali geneticky modifikované bioluminiscenční ostrůvky transplantované do arteficiálních skeletů implantovaných do podkoží, které představují alternativní transplantační místo. Multimodálním zobrazováním (MR a bioluminiscence) jsme určili optimální časování transplantačních kroků. Ostrůvky transplantované diabetickým potkanům podle optimalizovaného protokolu byly dostatečně prokrvené a funkční.

Vyvinuli jsme také nový trimodální zobrazovací model pro PIs transplantované ve skeletech. Značené bioluminiscenční ostrůvky byly zobrazené pomocí specifického ^{19}F MR zobrazování a senzitivního fluorescenčního zobrazování. Důležitým výsledkem je korelace ^{19}F MR a bioluminiscenčního signálu, která ukazuje, že po destrukci PIs jsou nanočástice z transplantačního místa odstraněna a proto nepřispívají k falešně pozitivním výsledkům. Experimenty potvrdili, že navrhovaný zobrazovací model je vhodný pro sledování transplantovaných ostrůvků *in vivo*.

Klíčová slova: magnetická rezonance, optické zobrazování, kontrastní látky, buněčné značení, pankreatické ostrůvky, transplantace

Acknowledgment

First of all, I would like to express my gratitude to my supervisor Dr. Daniel Jirák for great scientific support, encouragement, opportunities and help in many aspects during my study. Especially I would like to thank for his humor during work and travels and for all his (or common) funny stories.

My great thanks belong also to Dr. Vít Herynek for his helpful guidance, support, scientific ideas, nice images and tea times.

I would like to thank to Dr. Milan Hájek for his guidance and the opportunity to work in the MR group and to be a part of the Beta Train project. My gratitude goes also to the Beta Train fellows for their scientific help, motivation, unforgettable time and friendships, mostly to Rita Ribeiro for her help during my secondment in Leuven.

I would like to thank also to the colleagues from our MR group for their support and (not only) scientific discussions, especially to Markéta Jirátová. I also thank to my colleagues from the Laboratory of Langerhans islets for their help with experiments and to the colleagues from the Faculty of Natural Sciences and the Radbound Medical Center in Nijmegen for preparation of contrast agents.

I would like to acknowledge the Beta Train project (7^{th} EU Framework Program, No. 289932) and the Charles University Grant Agency (project No. 253215) for their financial support of experiments related to this thesis.

I like to thank also to my brothers and friends, who supported me during my studies and helped me when it was needed.

My greatest gratitude belongs to my mother and father for their support and love.

Content

Appendix

List of Abbreviations

^{1}H	hydrogen isotope
^{19}F	fluorine isotope
AUC	area under curve
BLI	bioluminescence
BCM	beta cell mass
CA	contrast agent
CCD	charge-coupled device
CEST	chemical exchange saturation transfer
CNR	contrast to noise ratio
CPMG	Carr-Purcell-Meiboom-Gill sequence
CT	computer tomography
DCE	dynamic contrast enhanced
DIACEST	diamagnetic chemical exchange saturation transfer
DM	diabetes mellitus
DOTA	tetraazacyclododecane-tetraacetic acid
DTPA	diethylene triamine pentaacetic
FLI	fluorescence
FOV	field of view
HYPERCEST	hyperpolarized chemical exchange saturation transfer
IBMIR	immediate blood-mediated inflammation reaction
ICG	indocyanine green
k_{EX}	exchange rate constant
LIPOCEST	lipid chemical exchange saturation transfer
LUC+	luciferase positive
LUC-	luciferase negative
MR	magnetic resonance
MRI	magnetic resonance imaging
MSCs	mesenchymal stem cells
MVD	microvascular density
NA	number of acquisitions
NP	nanoparticles

PARACEST	paramagnetic chemical exchange saturation transfer
PEG	polyethylene glycol
PET	positron emission tomography
PFCE	perfluoro-15-crown-ether
PFC	perfluorocarbon
PIs	pancreatic islets
PLGA	poly lactic-co-glycolic acid
PLGA-NP	PLGA-based nanoparticles
R_1	longitudinal relaxation rate
R_2	transversal relaxation rate
ROI	region of interest
RF	radiofrequency pulse
r_1^{OS}	outer sphere relaxation
r_1^{IS}	inner sphere relaxation
SNR	signal to noise ratio
SPECT	single photon emission computer tomography
SPION	superparamagnetic iron oxide nanoparticles
T1DM	type 1 diabetes mellitus
T2DM	type 2 diabetes mellitus
T_1	longitudinal relaxation time
T_2	transversal relaxation time
TA	transfection agent
TE	echo time
TF	turbo factor
TR	repetition time
Tx	transplantation
VEGF	vascular endothelial growth factor
WASSR	water saturation shift referencing

1 Introduction

Imaging methods have become an important tool for monitoring the outcome of cellular therapies such as transplantation of pancreatic islets intended for diabetes treatment. Although intrahepatic islet transplantation can restore insulin independence, its persistence is limited, the graft can be rejected after certain time and the procedure is often associated with partial damage of the liver tissue, blood-mediated inflammation or hypoxia. To elucidate the processes related to islet post-transplant fate or to test novel sites for PIs transplantation, the use of imaging methods is of a great help. Precise monitoring of islet distribution, mass and viability by a reliable method could finally contribute to optimization of transplantation protocols and improvement of transplantation outcomes.

Visualization of transplanted islets is conditioned by labeling with contrast agents or by genetic engineering of islets in order to create contrast between the transplanted islets and the host tissue. Each imaging method provides different information and is accompanied by various limitations as low spatial resolution (radionuclide imaging), specificity (proton (^{1}H) magnetic resonance imaging (MRI)), sensitivity (fluorine (^{19}F) MRI) or signal attenuation (optical methods). More complex information might offer combination of multiple imaging methods (multimodal imaging).

The most widely used and clinically implemented agents for islet labeling are superparamagnetic iron oxides nanoparticles (SPIONs), which are suitable for visualization by ^{1}H MRI. However, highly sensitive SPIONs offer low imaging specificity and only relative quantification of islet number. Moreover, clinically approved SPIONs were withdrawn from the European market and nowadays, there is no proper agent allowing non-invasive, sensitive and specific tracking of transplanted islets. Due to the lack of proper visualization method for transplanted PIs, this thesis aimed to test alternative probes and approaches for imaging of transplanted PIs. Novel contrast agents for MRI (based on chemical exchange saturation transfer (CEST) and fluorine-containing probes for ^{19}F MRI) and fluorescence imaging were tested, as well as genetically modified cells trackable by bioluminescence imaging.

The thesis is divided into the theoretical and experimental part. In the **Chapter 3**, application of current methods for visualization of transplanted islets is reviewed. Alternative approaches are introduced as CEST, ^{19}F MRI and optical imaging. The **Chapter 4** is divided into three main subsections that are focused on testing of the particular agents and approaches for visualization of pancreatic islets. Each chapter contains description of materials and

methods, results, discussion and summary. In the **Chapter 4.1**, novel frequency-selective CEST agents owing the possibility of discrimination between various cell groups were tested; in the **Chapter 4.2**, genetically modified bioluminescent PIs were implemented in order to track viability of islets transplanted at an alternative transplantation site (polymeric scaffolds) and in combination with MRI, timing of transplantation steps was optimized; in the **Chapter 4.3**, multimodal nanoparticles intended for tracking by ^{19}F MR and optical imaging were tested for longitudinal examination of transplanted PIs in scaffolds. Summary and overall conclusions that imply from the data are listed in the **Chapter 5**.

2 Aims

The aim of the proposed thesis is pre-clinical examination and validation of alternative visualization approaches for pancreatic islets by MRI and optical imaging. Feasibility of the novel contrast mechanisms is tested in order to improve monitoring of the transplanted graft and enhance the transplantation outcome. The specific aims are following:

1) Testing of frequency-selective MR contrast agents based on Chemical Exchange Saturation Transfer (CEST) for labeling of pancreatic islets.

Due to a possibility of simultaneous visualization of various CEST agents in one MR experiment, we hypothesized that the transplanted islets of different size or treated by different drugs could be distinguished using MRI, what could help to improve medical intervention and increase the transplantation outcome.

2) Visualization of transplanted pancreatic islets bioluminescence imaging.

The second task of the thesis is to implement bioluminescence for long-term *in vivo* tracking of localization and viability of transplanted islets at an alternative transplant site (polymeric scaffolds). The purpose of this study is optimization of the transplantation protocol in the scaffolds using a multimodal approach (MRI and bioluminescence).

3) Visualization of pancreatic islets labeled with multimodal nanoparticles using ^{19}F MRI and optical imaging.

The third task is optimization of labeling of pancreatic islets with multimodal nanoparticles that are trackable by ^{19}F MR and fluorescence imaging. Optimized labeling route should be implemented for longitudinal multimodal *in vivo* visualization (^{19}F MRI, fluorescence, bioluminescence) of pancreatic islets transplanted in artificial scaffolds.

3 Theoretical part

3.1 Diabetes mellitus

Diabetes mellitus (DM) is a chronic metabolic disease characterized by dysfunction of insulin production and glucose homeostasis leading to elevated blood glucose level (hyperglycemia) and causing serious health complications including nephropathy, retinopathy, vascular and heart pathologies.

Insulin is an endocrine hormone secreted by pancreatic islets (PIs) (islets of Langerhans), which promotes glucose utilization in fat, liver and skeletal muscle cells. PIs are highly vascularized clusters of several types of cells in the pancreas, which secrete hormones: glucagon (alpha cells), insulin (beta cells), somatostatin (delta cells), pancreatic polypeptide (gamma or PP cells) and ghrelin (epsilon cells) (Fig. 3.1). In type 1 diabetes mellitus (T1DM), beta cells are destroyed or non-functional what leads to impaired insulin production. T1DM is caused by an autoimmune T-cell mediated reaction against beta cells causing a gradual or absolute insulin deprival (Atkinson et al. 2014). Type 2 diabetes (T2DM) is not directly dependent on beta cell mass and insulin production (although beta cells might be impaired) as it results from insulin resistance at a receptor level in association with relative insulin deficiency (Olokoba et al. 2012).

Despite of a tremendous research, there are no approved agents able to stop the autoimmune destruction of beta cells (van Belle et al. 2011). The mostly used therapy for both T1DM and T2DM is exogenous insulin supplementation by multiple daily injections. Although subcutaneous insulin injections can keep glycemia in the physiological range, the administered insulin do not mimic physiologic secretion due to a delayed kinetics (sluggish on and delayed off) compared with that from pancreatic beta cells (Harlan 2016) and do not prevent diabetes-associated complications. An insulin overdose caused by improper physiological regulation of exogenously administered insulin may lead to hypoglycemic states (Mc Crimmon & Sherwin 2010). Some T1DM patients often suffer on recurrent hypoglycemia or impaired awareness of hypoglycemia manifested by loss of consciousness, seizures and coma (Fiallo-Scharer et al. 2011), what could be a life-threating issue as it is associated with significant morbidity and mortality.

T1DM can be treated not only by insulin supplementation, but also by replacement of insulin producing tissue – pancreas or isolated pancreatic islets. Especially in T1DM patients prone to hypoglycemia unawareness, transplantation of PIs represents an alternative cure.

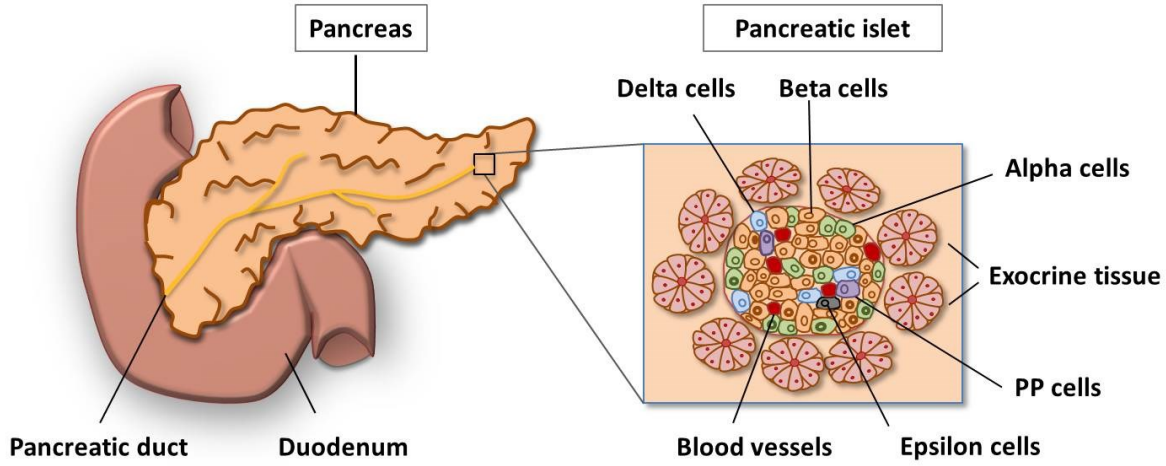

Fig. 3.1. Pancreas and pancreatic islets. Pancreas is an internal organ situated below stomach and connected to duodenum by a pancreatic duct. Human pancreatic cells are clustered into pancreatic islets consisting of approximately 20% of alpha cells, 70% of beta cells, <10% of delta cells, <5% of gamma cells and <1% of epsilon cells. Each islet is surrounded by exocrine tissue.

3.2 Transplantation of pancreatic islets

Transplantation of isolated PIs can restore normal insulin level with physiological regulation and thus prevent hypoglycemic episodes (Shapiro et al. 2017). The source of islets can be the recipient's pancreas after total pancreatomy (auto-transplantation) or from the cadaver's pancreas of a donor (allo-transplantation). In clinical practice, PIs are isolated from the pancreas in several steps starting by enzymatic digestion followed by several purification steps (Fig. 3.2) (Ricordi et al. 1989; Meiringeng et al. 2009). The initial outcomes of Tx PIs were low (<10% of normoglycemic patients) (Pyzdrowski et al. 1992; Largiader et al. 1980); however after improvements in islet isolation (purification and development of the Ricordi chamber) (Ricordi et al. 1989) and implementation of a glucocorticoid-free immunosuppressive protocol (known as Edmonton protocol) (Shapiro et al. 2000), insulin independence improved to approximately 44 – 70% at 3 years after PIs transplantation (Barton et al. 2012; Moassessfar et al. 2015). The outcomes are still not optimal and there is scarcity of cadaveric donors; therefore novel approaches for minimization of transplanted mass as well as novel transplantation sites that would prolong normoglycemia independence are examined.

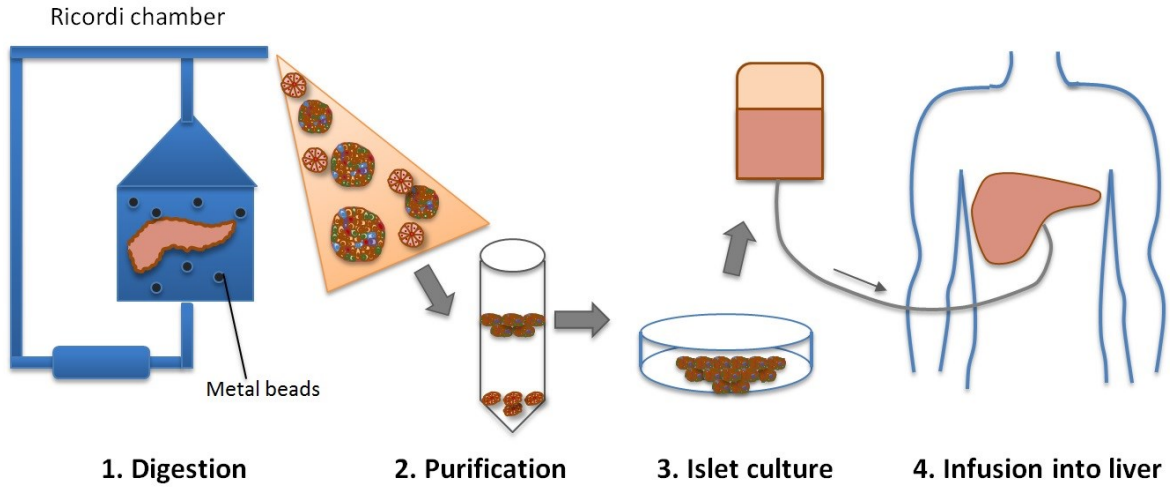

Fig. 3.2. Clinical transplantation of pancreatic islets. Digestion and purification of isolated pancreatic islets is followed by intrahepatic islet transplantation by injection through the portal vein. The pancreas is firstly infused with collagenase solution through a catheter inserted into the main pancreatic duct. Then, the tissue is transferred into the Ricordi chamber, where it is digested at 37 °C using metal beads and exocrine tissue is continuously being removed. Then, the islets are collected and washed in several steps prior transplantation. Purified islets are usually transplanted by injection into the hepatic portal venous system of a recipient through a percutaneous catheter under radiological navigation (Rheinheimer et al. 2015).

3.2.1 Transplantation sites for pancreatic islets

The most common and clinically applicable site for PIs transplantation is the liver at the present time. Because transplanted islets microembolize liver vessels, islets become highly vascularized what allows them to have good access to nutrients and to detect the blood glucose level directly (Shapiro et al. 2000). On the other hand, intrahepatic transplantation can be accompanied by various limitations that contribute to immediate or later-term graft loss and function impairment. Non-specific inflammation caused by direct contact of the donor islets with the blood so called immediate blood-mediated inflammatory reaction (IBMIR) (Naziruddin et al. 2014) together with islets hypoxia, drugs and toxins in the portal vein blood, lack of nutrients, insufficient vascularization and immune rejection (Korsgren et al. 2008) contribute to massive immediate destruction of 50 – 70% islets (Delaune et al. 2017). A rapid decline of transplanted mass within two post-transplant weeks was reported in both animal (Jirák et al. 2009) and human studies (Saudek et al., 2010). Besides the loss of mass and function of the transplanted islets, the liver tissue can be also impaired by ischemia

(Sakata et al. 2014) and thrombosis (Kawahara et al. 2011). Another drawback of intrahepatic PIs transplantation is impossibility of graft biopsy in the case of complications.

Because of accompanying obstacles of intrahepatic PIs transplantation, recent research has been directed also to search for alternative transplantation sites. An ideal site should provide minimal direct contact of the blood with islets to avoid IBMIR reaction, it should be highly vascularized, have access to physiological insulin delivery and provide an easy accessibility for implantation, further examination or retrieval (Cantarelli & Piemonti 2011). Several transplant sites, such as the muscle, kidney capsule, omentum, peritoneal cavity, eye chamber, bone marrow and subcutaneous space are being under examination, mostly in animal research (Harlan et al. 2009). Wide interest has been paid to the embedding of islets into the immunoisolative alginate capsules without need of immunosuppression (Vaithilinqam 2011; Lim & Sun 1980); however with limited vascularization (Chaikof 1999). One of the promising directions is incorporation of islets into the artificial capsules, scaffolds or micro/macro-devices as e.g., stainless-steel scaffolds (Pileggi et al. 2006), synthetic polymers (Kříž, Greg, et al. 2012; Gala-Lopez et al. 2016), a macrochamber with a semi-permeable immune barrier (Ludwig et al. 2012) or a pre-vascularized space created by a removable catheter (Pepper, Gala-Lopez, et al. 2015).

In the Institute for Clinical and Experimental Medicine (IKEM), scaffolds made from a polymeric silon mesh are being tested. Scaffolds can be implanted in the peritoneum or subcutaneously allowing an easy access and a possibility of removal. Subcutaneous implantation offers minimally invasive surgery and a possibility to monitor the islets easily. Visualization of transplanted PIs in the scaffolds by imaging methods is simple because PIs are not distributed and scattered in a large volume compared to transplantation into the liver. Moreover, optical imaging of PIs in the subcutaneously implanted scaffolds is possible due to a short optical path and low attenuation of the optical signal. Moreover, for vascularization enhancement, mesenchymal stem cells (MSCs) (Kříž, Greg, et al. 2012; Fabryova et al. 2014) that secrete multiple anti-inflammatory, immunomodulatory and trophic factors, including vascular endothelial growth factor (VEGF) may be added to the scaffolds (Boomsma & Geenen 2012).

3.3 Imaging of pancreatic islets

In order to optimize transplantation procedure, the transplanted mass should be monitored. The most common clinical tests that evaluate therapeutic interventions and improve treatment outcome are measurement of blood glucose level, glycosylated hemoglobin Hb1Ac, C-peptide or insulin secretion; however these methods are only indirect and they cannot determine whether the graft failure is caused by loss of beta cell mass or its function; and they often detect dysfunction after significant loss of islets mass. Another possibility is the use of imaging methods. Imaging of tissues/cells on the cellular or molecular level (so-called molecular imaging) holds a high potential for improvement and development of cellular therapies.

Visualization of transplanted islets could assess localization, survival and quantitative or functional changes of the transplanted mass over time, and thus directly elucidate the processes of islet engraftment and rejection. Monitoring of transplanted graft might help to assign a proper post-transplant treatment and prevent graft impairment. Moreover, imaging methods could also contribute to research of novel transplantation sites and approaches, e.g., optimization of a transplantation protocol or testing of different material intended for construction of the artificial scaffolds.

Several non-invasive imaging tools have been proposed for experimental visualization of native or transplanted PIs recently: magnetic resonance imaging (MRI), optical imaging, positron emission tomography (PET), single photon emission computer tomography (SPECT), computer tomography (CT) and ultrasound. Each method holds its own advantages and disadvantages in manner of sensitivity, spatial resolution, time consumption, penetration depth, or cost (Tab. 3.1).

Method	Spatial resolution	Sensitivity	Depth	Time	Cost
MRI	10 - 100 µm	µM - mM	No limit	Min - hours	$$$
CT	50 µm	mM	No limit	Sec	$$
US	<50 µm	mM	mm	Sec	$
PET/SPECT	1 - 2 mm	pM - nM	No limit	Min	$$/$$$
Fluorescence	1 - 2 mm	pM	< 1 cm	Sec - min	$
Bioluminescence	mm	< fM	cm	Min	$$

Tab. 3.1. Overview of small animal imaging methods. Comparison of typical spatial resolution, imaging sensitivity, penetration depth, time consumption and costs of several imaging techniques used for small animals. $ < 100 K, $$ 100 - 300 K, $$$ > 300 K (Weissleder 2002).

3.3.1 Labeling and targeting procedures for pancreatic islets

The size of one pancreatic islet is approximately 50 – 500 μm, which is below resolution of most of *in vivo* imaging methods. Signal of native PIs (cells in general) does not differ from the surrounding tissue under *in vivo* conditions. For PIs visualization, contrast should be created by cell labeling with contrast agents or genetic manipulation. In general, an ideal contrast agent for cellular labeling should

- be chemically stable and easily synthesized
- stay internalized in a cell or bounded on the cell surface
- be non-toxic and with no adverse effect on islet function
- be highly sensitive and specific
- allow precise quantification.

The aim of PIs labeling is to incorporate a contrast probe into the cells or on the cell surface in the highest possible concentration without compromising islet viability and functionality. PIs can be labeled both *in vitro* and *in vivo*. *In vivo* labeling represents intravenous administration of a probe specific for target cells, e.g., a radiolabeled tracer for PET imaging (Sakata et al. 2013). *In vitro* cell labeling can be classified as (i) non-specific that leads to incorporation of an agent in any cells; (ii) specific that targets only the desired cell type. Transplanted PIs can be also visualized by genetic targeting (reporter genes).

Non-specific labeling

Non-specific labeling includes endocytosis, enhanced endocytosis (with transfection agents) and physical methods, such as electroporation.

Endocytosis

Endocytosis represents an energy-requiring process (active transport) of internalization of ions and biomolecules by cell membrane invaginations. During labeling, a cell membrane engulfs a contrast agent from the culture medium within a certain period of time. Labeling efficiency depends on the agent size, shape, charge and surface chemistry, as well as cell type, incubation time, and amount of a contrast agent in the culture medium. Cell labeling by endocytosis is simple and effective for certain agents.

Most of the experimental and clinical studies have implemented endocytosis as a cell labeling mechanism, e.g., using superparamagnetic iron oxide nanoparticles (SPION) for PIs (Jirák et al. 2004). In general, longer incubation times lead to incorporation of higher amount of a contrast agent in the deeper structure of an islet (Berkova et al. 2008). Labeling by endocytosis is not specific and all types of cells within an islet could be labeled.

There are various types of endocytosis, namely receptor-mediated endocytosis, macropinocytosis, phagocytosis and clathrin-/caveloae-independent endocytosis.

- ***Receptor-mediated endocytosis*** is a mechanism of selective intracellular uptake of nanoscale materials via receptors. Optimal diameter of probes for receptor-mediated endocytosis is approximately 24 - 50 nm (Gao et al. 2005). Nanoparticles are coated with the plasma membrane proteins in the culture medium and then internalized via *clathrin* or *caveolae*. Firstly, a ligand (contrast agent) binds to a receptor, then the complex diffuse through the cell membrane and create clathrin-/ caveloae-coated pits that lately form the cytoplasmatic vesicles and endosomes. Clathrin is a membrane protein that can be found in almost all cell types, while caveolae is less frequent.
- ***Macropinocytosis*** represents absorption of extracellular fluids containing the contrast agents smaller than 10 nm through invagination of the cell membrane that creates intracellular endosomes. For example, pancreatic islets have been labeled with lanthanide chelates using pinocytosis (Biancone et al. 2007).
- ***Phagocytosis*** is an actin-dependent process of uptake of molecules larger than 0.5 μm in the phagocytic cells (macrophages, dendritic cells, neutrophils) (Oh & Park 2014).
- ***Enhanced endocytosis***. Agents with low labeling potential due to negative (or only slightly positive) surface charge need to be encapsulated or coated by positively charged compounds in order to enhance their binding efficiency to the negatively charged cell membrane. For this purpose, various positively charged coatings for the contrast agents have been implemented, e.g., poly Lactic-co-Glycolic Acid (PLGA) or phospholipid bilayer (Fröhlich 2012; Srinivas, Cruz, et al. 2010). Another approach is to use positively charged transfection agents (TAs) that bound preferably on the cell surface and enhance endocytosis. The most common TAs for PIs are polyamines (poly-L-lysine), lipid-based agents (lipofectamine) or polycationic peptides (protamine sulfate) (Arbab et al. 2004). However cell labeling with TAs is effective, the use of TAs ameliorate cell viability and its application in clinics is limited.

Physical methods

- ***Electroporation*** is based on application of electric pulses to the cells that create the reversible pores in the cell membrane. After application of voltage, permeability and conductivity of plasmatic membrane is increased allowing higher incorporation of a contrast agent in the cells. Electroporation is a fast and effective labeling method; however viability of the labeled cells could be affected. Labeling by electroporation was referred to be more effective compared to endocytosis because the probes are internalized directly into cytoplasm and not to endosomes that can "quench" water exchange (Terreno et al. 2006). Labeling of PIs by electroporation has been already performed in several experimental studies using iron oxide particles (Tai et al. 2006; Foster et al. 2005).
- ***Microporation*** is a modified electroporation technique that uses higher voltage compared to conventional electroporation due to different electrode geometry. The cells are placed in a small pipette tip that serves as an electroporation space supplemented with a gold-coated electrode. An uniform electric field is created vertically with minimal heat production, metal ion dissolution or oxide production (Lim et al. 2010).

Hypotonic swelling

Cell labeling can be performed also by using a hypotonic shock. Cells that are incubated in hypoosmotic medium swell and their cell membranes become leaky (Di Gregorio et al. 2013) allowing the inflow of water with a contrast agent directly into cytoplasm. Hypotonic swelling has been implemented for labeling of cells by lanthanide chelates (Di Gregorio et al. 2013; Ferrauto et al. 2014).

Specific labeling

Specific labeling allows labeling of selected cells via attachment of a targeting vector, e.g., antibodies, peptides, amino acids, conjugated to the contrast agent to target molecules and receptors on the cell surface (Bulte et al. 2004). This labeling approach has high specificity and effectiveness (Shapiro et al. 2007); however it depends on expression (density) of a target molecule on the cell surface, stability of the ligand-molecule complex, and it can often lead to insufficient imaging signal (Kim et al. 2007). PIs were labeled with the magnetic beads pre-coated with beta cell specific antibodies (Dynabeads, Dynal Biotech UK) and visualized both *in vitro* and *in vivo* in an animal model by MRI (Koblas et al. 2005).

Specific targeting - reporter genes

The cells can be genetically modified to produce a protein or enzyme of interest, which can be directly or indirectly tracked by imaging methods. A reporter probe accumulates only in the cells in which the inserted gene (called reporter gene) is expressed. The most common products of reporter genes for cell tracking are fluorescent proteins (green or red fluorescent protein), radiolabeled peptides or bioluminescent enzymes (luciferase). PIs are usually transduced with lentiviral or adenoviral vector that carries a required gene under control of a promoter, e.g., beta cell specific insulin promoter (Fowler et al. 2005; Chen et al. 2006). Luciferase expressing PIs are routinely used for visualization by bioluminescence. Although reporter genes have an important role in investigation of transplanted islets, the method is not applicable in clinics due to genetic manipulation.

3.3.2 Magnetic resonance imaging

In this thesis, mostly MRI is implemented and therefore its basic principle will be briefly described in the following section. Nuclear magnetic resonance (NMR or MR) is an outstanding non-invasive analytical and imaging method with a broad range of applications ranging from chemistry and biology to advanced medical imaging and molecular imaging. Molecular imaging using MR technique possesses the advantages of non-invasiveness, high spatial resolution and a possibility of using different contrast mechanisms. The use of ^{1}H MR contrast agents can also increase contrast and sensitivity; however absolute quantification, low specificity and lack of information about the functional status of transplanted cells represent a limitation of conventional ^{1}H MR.

MR phenomenon can be explained by quantum theory and can be found in various excellent works (de Graaf 2007). Because the complexity of MR principle is beyond the aim of this thesis, only a brief and simplified description will be given to understand the basics of MR mostly in connection to the use of contrast agents and specialized techniques, which were implemented within this thesis (^{19}F MRI, CEST).

MR principle is based on interaction of nuclear magnetic moments with external radiofrequency (RF) magnetic field. Only the isotopes with non-zero magnetic moment and angular momentum (non-zero spin) that contain odd number of protons and/or odd number of neutrons, e.g., ^{1}H, ^{13}C, ^{19}F, ^{31}P, ^{23}Na, are capable of MR interaction.

Hydrogen (proton ^{1}H in nucleus) has the highest clinical applicability due to its high concentration in organic compounds and especially in water that is abundant in biological tissues. Moreover, hydrogen has high MR sensitivity due to its highest gyromagnetic moment. On the other hand, fluorine ^{19}F has only negligible content in biological tissues, what allows specific detection of fluorine contrast agents. MR properties of chosen isotopes are listed in Tab. 3.2.

Nuclei	Magnetic moment [$5*10^{-27}$ A.m^2]	Gyromagnetic ratio [MHz/T]	Biological abundance
^{1}H hydrogen	2.8	42.6	88 M
^{23}Na sodium	2.2	11.3	80 mM
^{31}P phosphorus	1.1	17.3	75 mM
^{19}F fluorine	2.6	40.1	4 μM

Tab. 3.2. MR isotopes. Magnetic moment, gyromagnetic ratio and natural abundance of the most common isotopes used for detection by MRI (de Graaf 2007).

After placing into a static magnetic field, nuclear magnetic moments start to precess at Larmor frequency, while the axis of precession is either parallel or antiparallel to the direction of B_0; however the phase of the rotations is random. Larmor frequency is dependent on gyromagnetic ratio and $\vec{\boldsymbol{B}}_{\boldsymbol{0}}$ according to the formula

$$\vec{\boldsymbol{\omega}} = \gamma \times \vec{\boldsymbol{B}}_{\boldsymbol{0}} \tag{3.1}$$

where γ is gyromagnetic ratio, $\vec{\boldsymbol{B}}_{\boldsymbol{0}}$ – magnetic induction of the static external magnetic field and $\boldsymbol{\omega}$ is Larmor frequency (for MR nuclei in the range of radio waves [MHz]).

The vector of equilibrium magnetization $\vec{\boldsymbol{M}}_{\boldsymbol{0}}$ is parallel to $\vec{\boldsymbol{B}}_{\boldsymbol{0}}$ (longitudinal magnetization) and it is not measurable because it is indistinguishable from $\vec{\boldsymbol{B}}_{\boldsymbol{0}}$. By application of additional magnetic field $\vec{\boldsymbol{B}}_{\boldsymbol{1}}$ with the Larmor frequency and perpendicular to $\vec{\boldsymbol{B}}_{\boldsymbol{0}}$, the spins absorb energy causing the vector of magnetization out of $\vec{\boldsymbol{B}}_{\boldsymbol{0}}$ direction. When the magnetic field $\vec{\boldsymbol{B}}_{\boldsymbol{1}}$ is switched off, the vector of macroscopic magnetization returns to equilibrium in a process called relaxation and the system releases energy into the surrounding environment. The return of magnetization into the equilibrium can be detected by a receiver coil, where the signal is induced as so-called free induction decay (FID).

3.3.2.1 Basics of MRI contrast mechanism

Relaxation contains two independent processes - longitudinal (T_1) and transversal (T_2) relaxation that are characterized by T_1 and T_2 (T_2*) relaxation time, respectively. ***T_1* (or spin-lattice) longitudinal relaxation** represents the recovery of the vector of magnetization in the *z*-axis M_z into the equilibrium (in direction of $\vec{\boldsymbol{B}}_{\mathbf{0}}$) and it can be expressed by exponential decay equation with T_1 as a first-order time constant:

$$M_Z = M_0 \,.\, (1 - e^{-\frac{t}{T_1}}) \tag{3.2}$$

T_1 is a longitudinal relaxation time required for M_z to reach 63% of the equilibrium value M_0. T_1 relaxation represents energy exchange between excited spins and the surrounding (lattice) spins caused by dipolar interactions of spins with surrounding spins or interaction with paramagnetic compounds. Energy emission is stimulated by magnetic fields of another proton or electron on the same molecule of a nearby molecule that fluctuate near the Larmor frequency. Equilibrium is achieved again after a relatively long time (approximately $5 \times T_1$).

Immediately after RF irradiation, the spins are phased coherently and after switching off $\vec{\boldsymbol{B}}_{\mathbf{1}}$, the spins starts to dephase and the vector of magnetization in *xy*-plane is decreasing in a process called ***T_2* (or spin-spin) transversal relaxation** due to inhomogeneities of the local magnetic fields created by the magnetic moments. T_2 (transversal) relaxation time represents the time when the vector of magnetization in the *xy*-plane M_{xy} reaches 37% of the equilibrium value. T_2 relaxation follows an exponential decay according to:

$$M_{xy} = M_0 \,.\, e^{-\frac{t}{T_2}} \tag{3.3}$$

Free induction decay is not affected by T_1 and T_2 relaxation processes only; it strongly depends on inhomogeneities of the static magnetic field. An exponential decrease of M_{xy} during free induction decay is then described by a relaxation time T_2*, which corresponds to both outer non-uniformity of the magnetic field and spin-spin interaction.

Contrast in MR images is thus generated not only by different proton concentration, but mainly by different relaxation times of tissues due to different chemical composition. Relaxation times of biological tissues are usually in the range of hundreds ms (T_1) or tens ms (T_2) in dependence on magnetic field strength, temperature, chemical constitution, rotation and vibrational movements of molecules, their size etc.

3.3.2.2 Conventional ^{1}H MR contrast agents

By application of the RF pulses at specific time points according to the relaxation times, the compounds can be distinguished due to their different MR signal. The purpose of MR contrast agents (CA) is shortening of relaxation processes of water protons and increasing of the difference of MR signal intensities between the tissues. Relaxation rates R_1 or R_2 are inverses of T_1 and T_2 relaxation times respectively, and they represent the "speed" of the relaxation process. The ability of CA to affect T_1 or T_2 is characterized by relaxivity, which is defined as a relaxation rate R_1 or R_2 normalized to the CA concentration. Relaxivity is usually expressed in $mM^{-1}.s^{-1}$.

$$\frac{1}{T_{iOBS}} = \frac{1}{T_{iS}} + r_i.[CA] \qquad \text{i=1, 2,} \qquad (3.4)$$

where $\frac{1}{TiOBS}$ is the observed relaxation time in the presence of CA and $\frac{1}{TiS}$ is the solvent (tissue) relaxation time in absence of CA. [CA] refers to the CA concentration.

Conventional CAs for MRI can either influence the relaxation time (T_1, T_2) or modulate the local magnetic field inhomogeneities (T_2*) of the surrounding spins. Depending on their predominant effect on relaxation, they can be classified as T_1 (positive) or T_2 (negative) MR contrast agents according to the ratio r_2/r_1. In general, the paramagnetic ions facilitate both T_1 and T_2 relaxation with more dominant impact on T_1 relaxation (r_2/r_1 is up to 2), and superparamagnetic agents influence mostly T_2/T_2* relaxation (r_2/r_1 can reach 50) (Vargas & Chen 2010).

T_1 MR contrast agents

T_1 contrast agents enhance energy exchange between the spins and the surrounding and thus shorten T_1 relaxation time (increase contrast on T_1-weighted MR images). A paramagnetic ion (lanthanide, e.g., gadolinium Gd^{3+}, or metals, e.g., manganese Mn^{2+}) with unpaired electrons produces a strong magnetic moment capable of inducing magnetic relaxation in nearby nuclei (mostly protons in surrounding water and lipids) as a result of dipolar interactions. Lanthanide ions have to be bounded to a ligand (chelate), e.g., tetraazacyclododecane-tetraacetic acid (DOTA) or diethylene triamine pentaacetic acid (DTPA), to avoid release of a toxic Gd^{3+} ion. In such a structure, water molecules in ^{1}H MR can interact with the magnetic moment of Gd^{3+} by direct interaction in the close proximity of

Gd^{3+} ion in a crevice of the ligand (inner sphere relaxation r_1^{IS} – 0.25 nm) or indirectly by bounding on the second shell (second sphere relaxation r_1^{SS} – 0.4 - 0.5 nm) or just diffusing by (outer sphere relaxation r_1^{OS}) (Merbach et al. 2001). The inner-sphere relaxivity has the main contribution to relaxivity of the paramagnetic molecules and it depends on CA concentration [CA], the number of water molecules coordinated to the paramagnetic centre q, the mean residence lifetime τ_M of the bound water protons and the relaxation time T_{1M} of the coordinated protons (Solomon 1955) (Fig. 3.4 A). The relaxivity r_1^{IS} is given as

$$r_1^{IS} = \frac{q*[CA]}{55.5 * (T_{1M} + \tau M)} \quad (3.5)$$

At the magnetic field strengths typical for the clinical MRI scanners (0.5 – 1.5 T), T_{1M} is dominated by the molecular re-orientation (rotational correlation) time τ_R. The slower the re-orientation (thumbles) of molecule is, the faster the relaxation rate.

T_1 contrast agents for PI labeling

Cells labeled with paramagnetic CAs are visible as hyperintense spots on T_1-weighted MR images (positive contrast) without distortion of the magnetic field. The main limitation of T_1 CA is insufficient sensitivity, which is much lower compared to superparamagnetic iron oxides nanoparticles. Moreover, lanthanide chelates are small molecules (nm) that easily diffuse out of cells after labeling by endocytotis, which may cause loss of signal. The only study demonstrating *in vivo* visualization of PIs labeled with GdHPDO3A was published in 2007 (Biancone et al. 2007) (Fig. 3.4 C). Although the labeled islets were visualized as the hyperintense spots under the kidney capsule and in the liver of mice, sensitivity and persistence of visualization was low. For improvement of imaging sensitivity (relaxivity), more Gd^{3+} ions can be incorporated in one molecule, such as in cyclodextrines, that were implemented for PIs labeling and *in vitro* visualization (Kotková et al. 2010) (Fig. 3.4 B). Several studies showed MRI visualization of PIs encapsulated with Gd chelates (Arifin et al. 2013).

There are also agents that generate contrast due to a response to changes in physiologic environment or activity: accessibility to water (relaxivity), proton exchange rate, pH or temperature (Moats et al. 1997; Nivorozhkin et al. 2001). Responsive agents have been used also for indirect detection of beta cell mass. Because zinc (Zn) is co-released with insulin upon glucose stimulation, it can serve as a marker of beta cells or the probes can be targeted to zinc transporters. For example, a Zn^{2+}-activated gadolinium based agent (chelate with Gd^{3+}

and activable Zn^{2+}) can change its coordination geometry (relaxivity) upon Zn^{2+} binding and thus the probe is trackable by MRI (Major et al. 2007). Similarly, manganese ions Mn^{2+} enter the beta cells through voltage-gated calcium channels upon glucose stimulation so the presence of Mn^{2+} measured by manganese enhanced MRI can indirectly reflect beta cell function (Antkowiak et al. 2012).

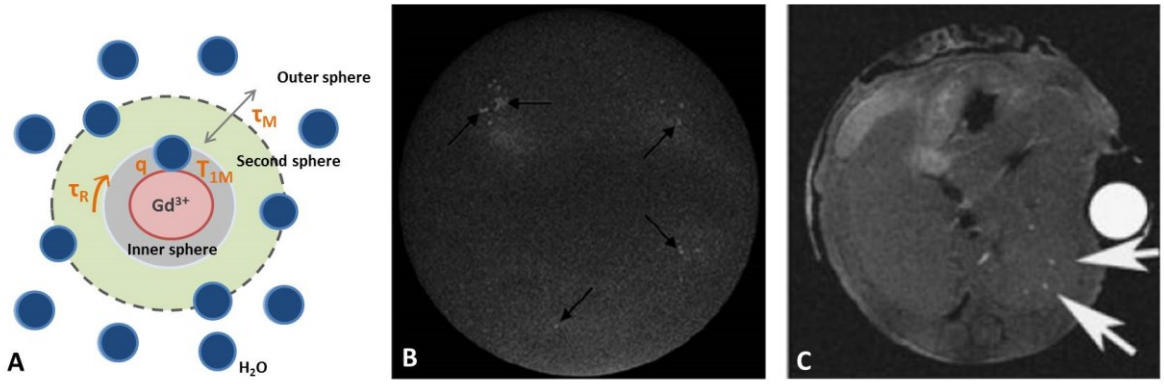

Fig. 3.4. T_1 MR contrast agents. A schematic illustration of the relaxometric mechanism for T_1 MR contrast agents (A). *In vitro* MRI visualization of PIs labeled with Gd-cyclodextrines (B) (Kotková et al. 2010). T_1-weighted images of PIs labeled with GdHPDO3A after transplantation into the liver (C); the image adapted from (Biancone et al. 2007).

Other approaches using T_1 CAs

Paramagnetic compounds are also useful for examination of neovascularization using dynamic contrast enhanced (DCE) MR method. This technique is capable to assess perfusion and vessel permeability related to vascularization after intravascular administration of a T_1 contrast agent. Hathout et al. showed that the MR signal enhancement correlates with the number of vessels around transplanted islets (Hathout et al. 2009).

T_2/T_2* MR contrast agents

T_2/T_2* CAs cause shortening of T_2/T_2* relaxation time and thus decreasing of MR signal intensity on T_2/T_2*-weighted MR images. Most of the T_2/T_2* contrast agents contain a superparamagnetic particle that induces a large magnetic moment in a static magnetic field, which disturbs the local magnetic fields of protons. Therefore, the MR signal is decreased and the labeled cells are visible as hypointense spots on T_2/T_2*-weighted images.

T_2/T_2* CAs have only minor application in clinical practice, although they are broadly used in the experiments, including cell labeling. Typically used T_2 contrast agents are superparamagnetic iron oxide nanoparticles (SPIONs), which consist of crystalline magnetic iron oxide core (composite of magnetite (Fe_3O_4) and maghemite (gamaFe_2O_3); size between 4 and 10 nm) and a hydrophilic surface coating that prevents agglomeration, reduces toxicity and alters pharmacokinetics and biodistribution (Tsourkas & Josephson 2010). The widely used coating for SPIONS is polysaccharide dextran/carboxydextran, which is non-toxic, electrically neutral and metabolic inert. There are also other tested coating materials as poly-L-lysine, polyvinylpyrrolidone, chitosan, heparin, silica etc. (Pongrac et al. 2016).

SPIONs have been extensively studied for tracking of various cell types including PIs. The most common used SPIONs for labeling of pancreatic islets are ferucarbotran, carboxydextran coated ferumoxide particles - Resovist® (size ≈ 60 nm) and dextran-coated ferumoxide particles – Feridex®/Endorem® (size ≈ 80-180 nm).

The first proof of tracking of the SPIO-labeled (Resovist®) islets *in vivo* was performed in 2004 in an animal model of intrahepatic islet transplantation in the Institute for Clinical and Experimental Medicine (IKEM) in Prague (Jirák et al. 2004) (Fig. 3.5 A). The grafts were tracked for 22 weeks after transplantation and the blood glucose level of diabetic rats was normalized. MRI tracking of SPION-labeled PIs revealed also changes of post-transplant PIs mass in syngeneic, allogeneic and xenogeneic animal models (Jirák et al. 2009). All transplant groups showed a dramatic signal loss within one week after transplantation, while in the second week the groups significantly differed. Moreover, using SPIONs for islet labeling, the islet graft impairment can be detected by MRI in advance of functional failure (Kříž, Jirák, et al. 2012). Importantly, several studies confirmed that SPIONs labeling did not affect islet viability and functionality (Berkova et al. 2008). The feasibility and safety of visualization of SPION-labeled transplanted islets was also confirmed in the clinical trials with T1DM patients (Saudek et al. 2010; Toso et al. 2008) (Fig. 3.5 B). In 2010, a clinical study with 8 T1DM patients was performed in IKEM, from which 5 patients reached insulin independence. Decrease of numbers and area of the hypointense spots (early and late graft loss) on the T_2-weighted MR images correlated with the results obtained in animal experiments (Jirák et al. 2009).

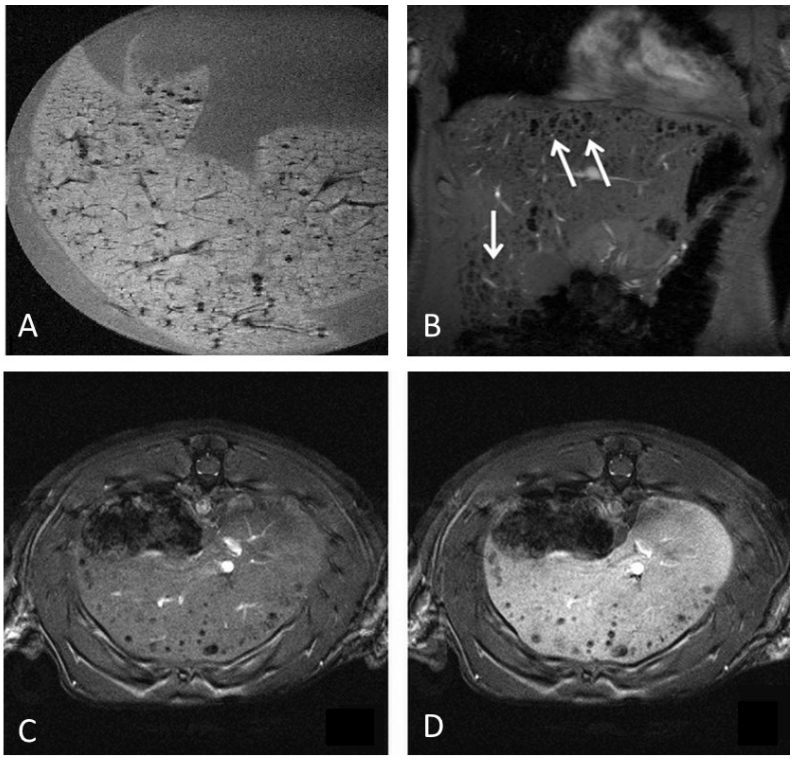

Fig. 3.5. T_2 contrast agents. Example of MRI visualization of SPION-labeled pancreatic islets *in vitro* (A) (Jirák et al. 2004) and *in vivo* after intrahepatic transplantation in a patient (B) (Saudek et al. 2010) and a rat (C, D). Application of a T_1 contrast agent improves visualization of transplanted islets (D) (Herynek et al. 2011).

Sensitivity of visualization of islets labeled with T_2/T_2* contrast agents is very high; although absolute quantification of the labeled islets is limited due to a disruption of local magnetic field beyond the actual size of an islet – so called "blooming artefact" and only relative amounts can be estimated. Moreover, it has been shown that SPIONs are taken up by macrophages, which may then contribute to false positive results after cell death (Berkova et al. 2008). This issue represents a limitation in proper visualization of intracellular imaging labels (Terrovitis et al. 2008). Improvement of sensitivity of SPION-labeled islets and elimination of imaging artefacts can be accomplished by double contrast approach using a T_1 contrast agent for liver signal intensity enhancement, while the transplanted islets are labeled with a T_2/T_2* CA (Herynek et al. 2011). Besides above-mentioned SPIONs, novel non-commercial agents are tested as magnetoliposomes-based CAs (Ribeiro et al. 2018) or conjugates of iron oxides and exendin-4 supplemented with a fluorescent dye Cy5.5 (Wang et al. 2014).

3.3.2.3 Alternative MR visualization approaches

There are many novel MR contrast agents based on various principles (e.g., chemical exchange, hyperpolarization etc.) or different isotopes than conventional ^{1}H (e.g., ^{19}F). Within this thesis, MR probes based on proton chemical exchange saturation transfer (CEST) and probes containing ^{19}F isotopes were tested.

3.3.2.3.1 Chemical Exchange Saturation Transfer (CEST)

CEST agents represent a group of paramagnetic agents that can generate contrast due to proton exchange after saturation at a specific frequency. CEST has been recently reported also as a possible contrast mechanism for cellular imaging (Ferrauto et al. 2013) and therefore we investigated this approach for labeling and visualization of PIs.

CEST effect is based on frequency selective saturation of labile protons and subsequent transfer of the saturation to the water pool due to chemical exchange. There could be various forms of exchanges as proton exchange, water-ligand (molecule) exchange, proton and molecule exchange, compartment exchange and molecule-mediated compartment exchange (Liu et al. 2013). The CEST agents can be classified according their exchange rate (chemical shift) as diamagnetic (DIACEST) with the small frequency offset from water (up to 5 ppm) and paramagnetic (PARACEST) with the larger chemical shift (tens of ppm). There are also other groups as hyperpolarized (HYPERCEST) or liposomal CEST agents (LIPOCEST).

A CEST agent contains labile (exchangeable) protons that are in a constant chemical exchange with the larger water pool and resonate at different frequency from water, which allows their selective saturation. Ideally, after application of a saturation RF pulse, the Boltzman distribution of spins is altered and the number of spins aligned with and against the external static magnetic field is equal, and therefore no vector of magnetization is created. Due to chemical exchange, the saturated protons physically move to water pool causing a reduction of magnetization in water. Because the water signal intensity is decreased, CEST contrast is negative. Since the creation of CEST contrast depends on irradiation at the proper frequency, it can be switched on/off and multiple agents with the properly shifted frequency offsets can be visualized allowing so called multi-color MRI (Liu et al. 2012). A scheme of CEST principle is shown in Fig. 3.6.

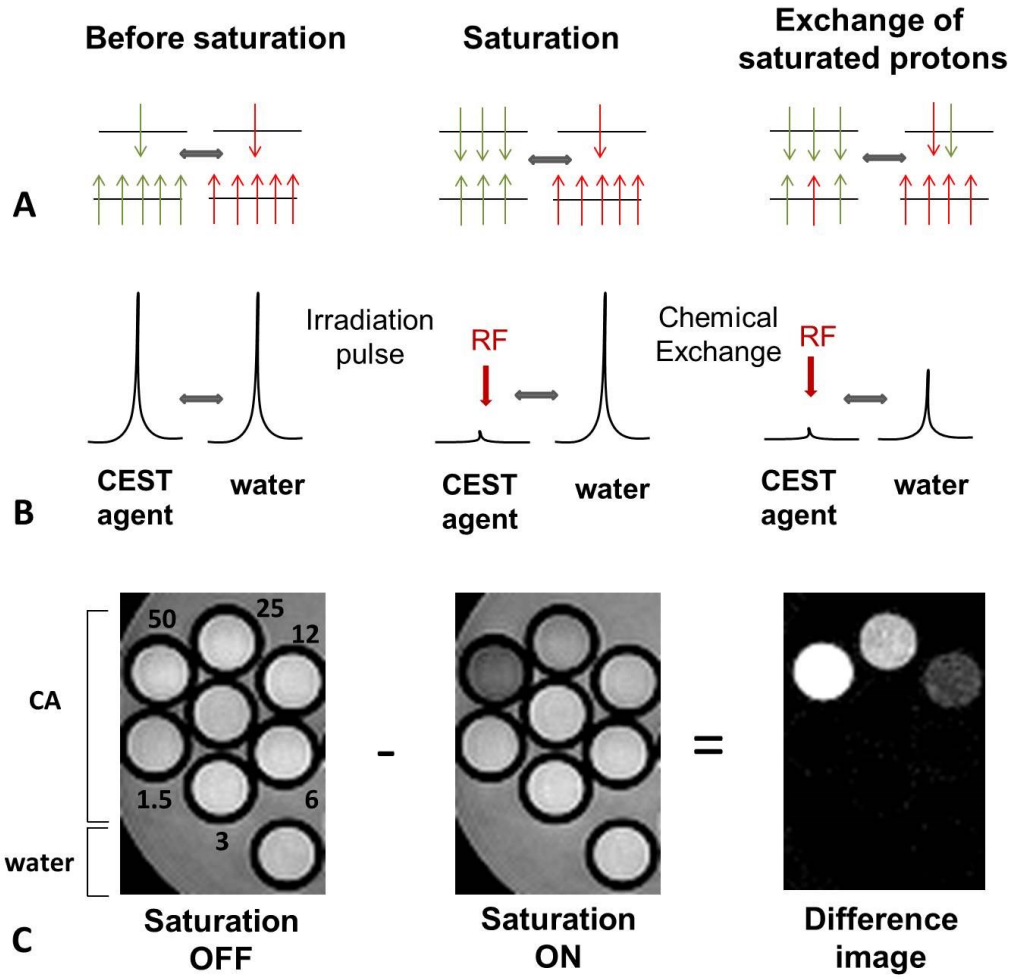

Fig. 3.6. A simplified scheme of the principle of CEST. Spin distribution in a system before and after saturation by a RF pulse (A) with corresponding MR signal (B). As a result, a difference image can be created by subtraction of the images acquired before (Saturation OFF) and after application of a saturation pulse (Saturation ON) (C). The phantom contains tubes with various concentrations of a CEST contrast agent (CA) and water (C). The numbers represent concentration of a CEST agent in mM.

CEST effect can be characterized by two-pool exchange model and described by the modified Bloch (Bloch-McConnel) equations considering saturation and chemical exchange (no back exchange of saturated protons) (Liu et al. 2012; Zhou et al. 2004). In this model, two non-equivalent spin pools (a larger water pool and a smaller solute pool) are in a constant chemical exchange characterized by an exchange rate constant k_{EX} [Hz], which is a composite of k_{SW} [Hz] (exchange rate from solute to water) and k_{WS} [Hz] (exchange rate from water to solute). Since the water pool is much larger (110M) compared to the solute pool (μM – mM), the rate constant can be expressed as $k_{EX} = k_{SW} + k_{WS} \approx k_{SW}$. The exchange rates can be then

determined from the mass balance $k_{SW} / k_{WS} = M_{0W} / M_{0S}$, where M_{0W} and M_{0S} are equilibrium magnetizations of water and the CEST agent, respectively (Liu et al. 2013). The CEST effect is proportional to the fractional concentration of the solute protons X_S, the saturation efficiency α, the exchange rate k_{SW} and relaxation rate R_1 (van Zijl & Yadav 2011). The two-pool model can provides a solution in the form of a proton transfer ratio (PTR):

$$PTR = Xs.\alpha.k_{SW}.T_1\,(1 - e^{-\frac{tsat}{T_{1W}}}) \qquad (3.6)$$

The exchange rate constant k_{EX} depends on the frequency offset of the agent (Δω). CEST effect is only visible if the exchange is slow on the timescale of NMR measurement so $kex << \Delta\omega$. This slow or intermediate exchange leads to separation of spectral lines necessary for efficient detection of decrease in the water signal and indirect observation of the CEST agent, which is not detectable by the standard MR techniques due to low concentration. Because the chemical exchange "compete" with relaxation, its rate should be also faster than T_1 relaxation to detect sufficient signal, so $R_1 << k_{ex} << \Delta\omega$.

Another type of saturation transfer (except CEST) is magnetization transfer (MT) effect that occurs between bulk water and solid or semi-solid substances e.g., cell membranes or macromolecules through dipolar cross-relaxation (van Zijl & Yadav 2011) and/or combination of cross-relaxation and chemical exchange (Kingsley & Monahan 2000; Liu et al. 2013). In contrast to CEST, the lineshapes of the MT pool are symmetric to water and can be eliminated by asymmetric analysis by calculation of asymmetric magnetic transfer ration (MTR_{ASYM}). In biological tissues, both MT and CEST effects occur often at the same time and should be differentiated for proper quantification.

Quantification of CEST effect

For identification of the CEST peaks of an agent, water signal intensity is measured at several frequency offsets after saturation with a saturation pulse. A plot of the saturated water signal intensity normalized to the signal without saturation is called the Z-spectrum (Grad & Bryant 1990) and it is specific for each CEST agent. Usually, the Z-spectra are acquired using a variable sampling steps either within the whole spectrum (necessary for DIACEST agents) or only around the known irradiation offsets (satisfactory for PARACEST). Then, the measured data points are interpolated (e.g., using the smoothing-splines) or fitted by the modified Bloch equations for chemical exchange between two pools. The CEST effect for each offset is quantified as a percentage of signal intensity decrease in comparison to signal intensity measured without saturation (S_0). PTR is also a very

straightforward quantification metric; however improper in the presence of MT and direct saturation (DS) of water (Liu et al. 2013). In the simplest way, the CEST effect can be calculated as a percentage of water signal intensity decrease:

$$CEST = \frac{S_{SAT}(\Delta\omega) - S_{SAT}(-\Delta\omega)}{S_{SAT}(-\Delta\omega)} * 100\% \quad (3.7)$$

To separate CEST from MT and DS, CEST can be calculated as MTR_{ASYM}, which is defined as:

$$MTR_{ASYM} = \frac{S_{SAT}(\Delta\omega) - S_{SAT}(-\Delta\omega)}{S_0} * 100\% \quad (3.8)$$

or

$$MTR_{ASYM} = \frac{S_{SAT}(\Delta\omega)}{S_{SAT}(-\Delta\omega)} * 100\%, \quad (3.9)$$

where $S_{SAT}(\Delta\omega)$ and $S_{SAT}(-\Delta\omega)$ are water signal intensity after saturation at the frequency offsets $\Delta\omega$ and $-\Delta\omega$, respectively and S_0 is water signal intensity without saturation.

CEST effect can be calculated from the Z-spectra, or from the MR images within a region or interest (ROI), or on the pixel-wise basis (e.g., MTR_{ASYM} maps). For visualization of CEST in an image, a difference image is usually reconstructed by subtraction of the image acquired by saturation at $\Delta\omega$ and $-\Delta\omega$ (or average of several offsets around $\Delta\omega$/-$\Delta\omega$).

Practical consideration of CEST approach

Higher magnetic field strengths increase sensitivity of CEST signal. Usually long saturation periods using a rectangular pulse (duration > 2-3 s) are implemented; however specific absorption rate (SAR) should be taken into account and differently shaped pulses are preferred in some applications (e.g., Gaussian, Fermi) (Dixon et al. 2010). To suppress the SAR effect, multiple shorter pulses (range of ms) so called pulsed-CEST are often implemented; however their optimization is more complicated compared to rectangular pulses due to wiggles generation in the Z-spectrum (Liu et al. 2013). Higher pulse power generates higher CEST signal; although the Z-spectrum gets broader what complicates quantification. Usually, pulses with power in the range of several μT are used.

CEST effect is also very sensitive to $\vec{B}_0$ and $\vec{B}_1$ inhomogeneites that should be minimized for a proper quantification. The most common and useful method for $\vec{B}_0$ correction in a CEST experiment is acquisition of a fine-resolved Z-spectrum around the water peak using a weak pre-saturation pulse is so called WAter Saturation Shift Referencing (WASSR) (Kim et al. 2009). By using the WASSR approach, a $\vec{B}_0$ map is generated by finding the shift of the water peak from zero in each voxel and then the inhomogeneity is

corrected by moving it to zero. Other $\boldsymbol{B_0}$ correction methods include the gradient-echo based maps (Sun et al. 2007) or a more recent fitting of the spectra by a Lorentz lineshape (Liu et al. 2010).

Applications of CEST

Conventional paramagnetic (Gd^{3+}) contrast agents do not serve as CEST agents due to fast chemical exchange; however lanthanide chelates with other central atoms as e.g., Eu^{3+}/Yb^{3+}-DO3A (HPDO3A) can provide CEST effect (Krchová et al. 2013; Aime et al. 2005). CEST approach can be used for estimation of metabolite concentration (Schleich et al. 2016; Kogan et al. 2014; Wang et al. 2016; Haris et al. 2011; Cai et al. 2012) or pH in biological tissues (Delli Castelli et al. 2014).

CEST was also proposed as a contrast mechanism for cells labeled with exogenous agents (Wang, 2009). The first report of *in vitro* visualization of the cells labeled with the CEST agents (Eu^{3+}- and Tb^{3+}-DOTAM-Gly) was published in 2005 (Aime et al. 2005); however further translation was hampered by insufficient biocompatibility of the agents and large chemical shift resulting in high irradiation field strength. In 2013, the same group reported an *in vivo* differentiation of two different cell populations (macrophages and melanoma cells) labeled with Eu- and Yb-HPDO3A using the CEST approach (Ferrauto et al. 2013). Ferrauto at el. also utilized CEST effect for labeling of the red blood cells by lanthanide liposomes that act as the shift reagents with the aim to assess the blood volume in a tumor upon release of liposomes manifested by the change of the CEST contrast (Ferrauto et al. 2014). In 2015, simultaneous visualization of neural stem cells and endothelial cells in a mouse model of stroke was also reported (Nicholls et al. 2015). Although the study reported a nice proof-of-principle and the experiments were supported by a strong simulation background, the authors encountered also with low sensitivity of the method. The difference in CEST signal between labeled and unlabeled cells was only 3.27% under *in vivo* condition.

There was no study focused on visualization of pancreatic islets by CEST approach, therefore in this thesis, we examined two PARACEST agents (Eu- and Yb-DO3A chelates) as alternative contrast agents for labeling of PIs.

3.3.2.3.2 Fluorine ^{19}F MRI

The main advantage of using ^{19}F isotopes in comparison to ^{1}H is their negligible content in the tissues allowing high specificity of visualization. ^{19}F resonates at frequency close to ^{1}H (94% of ^{1}H); therefore same MR hardware with minor modifications (special RF coils) can be used as for ^{1}H MRI. Usually, the RF coils are constructed as dual-tuned for both $^{1}H/^{19}F$ and ^{19}F MR signal is visualized as "hot spot" signal overlaid on ^{1}H MR anatomical reference (Fig. 3.7).

The number of ^{19}F nuclei is proportional to their ^{19}F MR signal allowing absolute quantification of ^{19}F atoms, which enables estimation of the number of labeled cells. The drawback of ^{19}F MR cell imaging is low sensitivity due to low amount of ^{19}F per a molecule of synthetized agents. Usually, concentration of ^{19}F atoms in a contrast agent is in milimolar range (water has 100M), therefore the agents containing high amount of ^{19}F atoms are necessary for sufficient visualization by ^{19}F MR. Another important factor for their visualization is chemical equivalency of ^{19}F atoms in the molecule leading to a good resolved single spectral peak. In case of multiple peaks, chemical shift artefacts are presented in the MR images.

^{19}F MR probes has been already implemented in various medical applications ranging from drug development (Wolf et al. 2000), assessment of lung ventilation (Wolf 2006) to cell labeling (Ahrens & Bulte 2013). The mostly used ^{19}F agents for MRI are perfluorocarbons (PFCs) e.g., perfluorodecalin ($C_{10}F_{18}$), perfluorohexane (C_5F_{14}), perfluorooctane (C_8F_{18}), perfluoro-15-crown-ether (PFCE) ($C_{10}F_{20}O_5$) or perfluorobromide (PFOB) (C_8BrF_{17}). The majority of labels are emulsions, which need to be coated with a suitable surfactant as lipids, phospholipids and poloxamers (Srinivas et al. 2012). One of the examples are the freezable non-toxic PFCs encapsulated into a PLGA polymer, which allow incorporation of various compounds on the surface or inside such as dyes allowing the use of other imaging modality (Srinivas, Cruz, et al. 2010). Size (200 - 2000 nm), coating (antibody), content (imaging agent, fluorescent dye, drug) and surface charge (-40 to 30 mV) of these agents can be customized to reach specific requirements (Srinivas et al., 2010). These nanoparticles were used for visualization of PIs in this thesis.

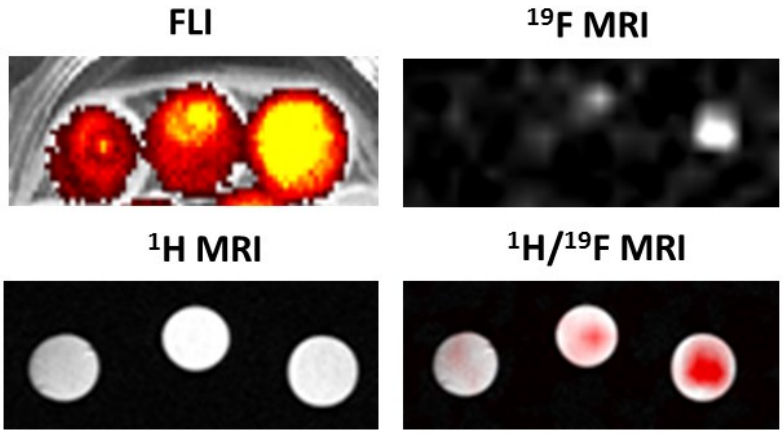

Fig. 3.7. Multimodal imaging of islets labeled with PLGA-based nanoparticles containing PFCE. Fluorescence image (FLI), ^{1}H MR anatomical image, ^{19}F MR image and a merged ^{1}H/^{19}F MR image of the phantoms with 50, 100 and 300 islets (from left to right) labeled with 12.5 mg/mL of nanoparticles.

Practical consideration using ^{19}F MRI

To increase detection sensitivity of ^{19}F MR, novel acquisition or post-processing approaches are tested. Liang et al. implemented acquisition of sparse sampled data (compressed sensing) for acquisition time decrease and increase of SNR (Liang et al. 2017). The dual-tuned coils (^{1}H/^{19}F) are implemented for co-registration of ^{19}F signal on anatomical ^{1}H reference (e.g., transplanted labeled cells in the organ/body). Most of the studies dealing with ^{19}F MR were performed using surface coils due to their easier construction and higher SNR, although non-uniform excitation and loss of signal in dependence on distance from a coil complicate quantification (Ruiz-Cabello et al. 2010).

The main advantage of ^{19}F MR over other MR techniques is absolute quantification, which can be performed from both ^{19}F MR images and spectra, if a reference tube with a known number of ^{19}F atoms is present (Srinivas et al. 2007). Fluorine content in labeled islets (F_{PI}) can be calculated from the ^{19}F MR images by comparison of the signal of labeled islets S_{PI} to the signal of a reference S_{REFI} (containing a known number of ^{19}F atoms F_{REFI} in the voxel). The agent uptake can be calculated according to the formula:

$$F_{PI} = \frac{S_{PI}}{S_{REF1} * N} * F_{REF1}, \tag{3.10}$$

where N represents number of PIs in the sample.

The number of engrafted islets N_{TxPI} can be quantified from *in vivo* ^{19}F MR images by comparison of the signal of transplanted islets S_{TxPI} to the signal of the reference S_{REF2} and by taking into account amount of ^{19}F atoms in the reference F_{REF2} and the agent uptake per one islet F_{PI} estimated in the *in vitro* study. The amount of islets can be then calculated as

$$N_{TxPI} = \frac{\frac{S_{TxPI}}{S_{REF2}} * F_{REF2}}{F_{PI}} . \quad (3.11)$$

Intracellular ^{19}F content (after non-specific labeling by endocytosis) usually ranges between 10^{11} - 10^{13} ^{19}F atoms/cell (Srinivas et al. 2012; Srinivas et al. 2007) and the minimum amount of cells for sufficient detection was reported to be 2000 cells/voxel at 7 T *in vitro* (Helfer et al. 2010) and 7500 cells/voxel at 11.7 T *in vivo* (Srinivas et al. 2007).

Application of ^{19}F MR for cell labeling

Several studies reported short-term *in vivo* tracking (days or weeks) of labeled cells by ^{19}F MRI in various animal models (Srinivas et al. 2007; Bonetto et al. 2012; Gaudet et al. 2015; Ahrens & Bulte 2013). For instance, a group of Böhm-Sturm implemented a multimodality platform to study transplanted progenitor cells in the stroke-damaged brain for 4 weeks (Böhm-Sturm et al. 2014). ^{19}F labeled dendritic cells were also tested for immunotherapy of colorectal cancer in humans and other clinical trials are ongoing (Ahrens et al. 2014).

Despite a broad application of ^{19}F labels for cellular labeling, there is only one *in vivo* study focused on tracking of PIs labeled with multimodal PFOB (for ^{19}F MRI, CT and ultrasound) (Brad P; Barnett et al. 2011). Detection sensitivity in this study is relatively low, 2000 islets were visualized *ex vivo* and as much as 10 000 islets were visualized under the kidney capsule of rabbits. Moreover, transplanted islets were measured only at one time point post transplantation without long-term information about the transplanted graft. Due to lack of evidence about labeled PIs by specific ^{19}F-containing probes, we used PFCE nanoparticles coated with PLGA and containing a fluorescent dye indocyanine green (ICG) for multimodal tracking of transplanted PIs in an animal model.

3.3.3 Optical imaging

Optical imaging (OI) is a non-invasive imaging modality capable of detection of light originating from the living subjects. The subtle photon emission from either the exogenous optical probes or from the genetically-modified cells with expression of the reporter genes for luminescent enzymes can be detected by a highly sensitive charge-coupled device (CCD). OI is advantageous over other imaging methods due to outstanding sensitivity below 10^{-12} M, short acquisition times (seconds to minutes), lower cost, easy operation and the possibility of measurements of multiple animals in one experiment. On the other hand, the major obstacle of OI is limited light penetration as a consequence of attenuation, reflection and scattering of optical signal in biological tissues.

Absorption of light is mainly affected by the presence of hemoglobin, which absorbs strongly in the blue-green part of spectrum of visible light (VIS) (Rice et al. 2001). Attenuation of light is prominent in the visible range of spectrum (400 – 650 nm), while in the near-infrared (NIR) spectrum (650 – 900 nm) is lower and therefore NIR is preferable for *in vivo* applications. Above 900 nm, water absorption in the tissues takes place and it prevents deep penetration of the light. Scattering originates mostly due to changes in relative refractive index at organs, cell membranes and organelles leading to the effective length for scattering about 0.05 cm in biological tissues. The photons can be detected from maximum depth of 1 or 2 cm; the optical signal is attenuated by approximately 100× for wavelengths at ≈ 650 nm at the depth of 1 cm (Rice et al. 2001).

Propagation of photons from the light source to the CCD aperture in a homogenous tissue can be described by a diffusion model (Ishimaru 1978). Under the assumption that the scattering is dominant over absorption in most tissues (scattering coefficient μ_S >> absorption coefficient μ_A) (Ntziachristos 2010), the photon fluence Φ (W/cm^2) can be described as exponential decay dependent on the distance from the source (r), power of source (P), diffusion coefficient (D) and the effective attenuation coefficient μ_{eff} [cm^{-1}] (reflects both absorption and scattering) (Rice et al. 2001). In the majority of the small animal optical imaging systems, the radiance L [W/cm^2/sr] along a unit vector s is measured as a combination of the photon fluence (number of photons) and the flux (the rate of propagating photons):

$$L(r,s) = \frac{1}{4\pi[\phi(r)+3j(r).s]} \tag{3.12}$$

where $j(r)$ is the photon flux (Farrell et al. 1992). Using this model, the radiance on the animal

surface can be calculated and the resulted image is diffuse one (Fig. 3.8).

Light emission can be generated in the living subjects by two main processes: fluorescence (FLI) and bioluminescence (BLI). Photon emission by fluorophores is dependent on excitation light in contrast to bioluminescence that occurs upon a chemical reaction without the need for external light irradiation. In most of the optical systems for small animal imaging, radiance is estimated from a photon counts on a CCD chip within certain time [seconds] originating from a pixel [cm^2] under a spatial angle θ [sr]; therefore the units are photons/seconds/cm^2/sr. In case of fluorescence, the signal is normalized to the excitation light (because of inhomogeneous excitation) and the final signal can be expressed as radiance efficiency in units ([photons/seconds/cm^2/sr]/[$\mu W.cm^2$].

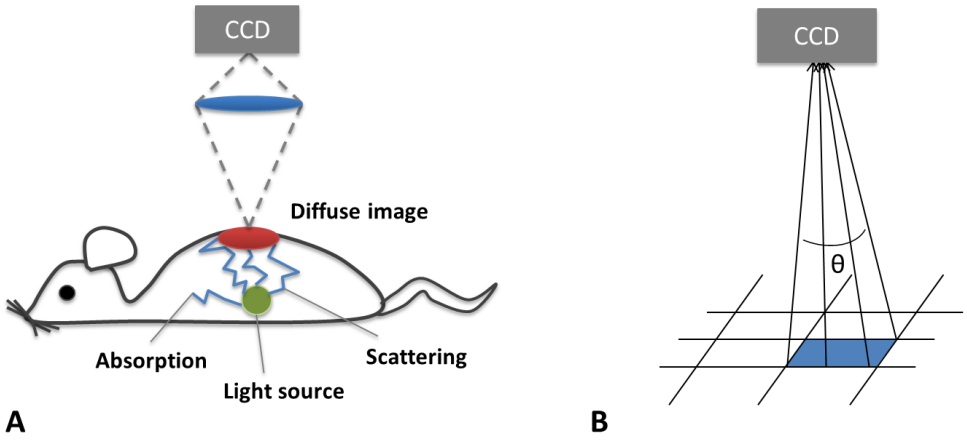

Fig. 3.8. Small animal optical imaging. The optical signal originates from a light source: (i) a fluorophore produces light after excitation, (ii) light is created in a biochemical bioluminescence reaction (A). The resulted image on the animal surface is diffuse because of scattering and absorption of light in the tissue (A). Radiance is estimated from a photon counts on a CCD chip within certain time originating from a pixel (blue color) under a spatial angle θ (B).

Bioluminescence

Bioluminescence represents a self-emission of photons in the enzymatic reaction, which involves a light-emitting molecule (generally called luciferin) and an enzyme (called luciferase). Luciferins and luciferases may differ in different species. In eukaryotic cells, a gene for luciferase isolated for example from a firefly beetle (Photinus pyralis), coral (Renilla reniformis), yelly fish (Aequorea victoria) or bacteria (Photorhabdus luminescens) is incorporated in their DNA. The most common luciferase for biological applications is firefly luciferase that catalyzes a biochemical reaction of oxygenation of D-luciferin with one of the

products being light with broad spectrum (peak at approximately 560 nm). The reaction is dependent on the presence of oxygen and adenosine triphosphate (ATP), therefore only viable cells can be detected (Fig. 3.9). Renilla and Gaussia luciferases catalyze reactions with different substrate – coelentrazine, which produces blue light (peak at 480 nm) (Luker & Luker 2008). Bioluminescence exhibits high signal-to-noise ratios due to negligible background and acquisition times ranging from seconds to minutes. Bioluminescence has an important role in pre-clinical developments; although it is not suitable for human application due to genetic manipulation.

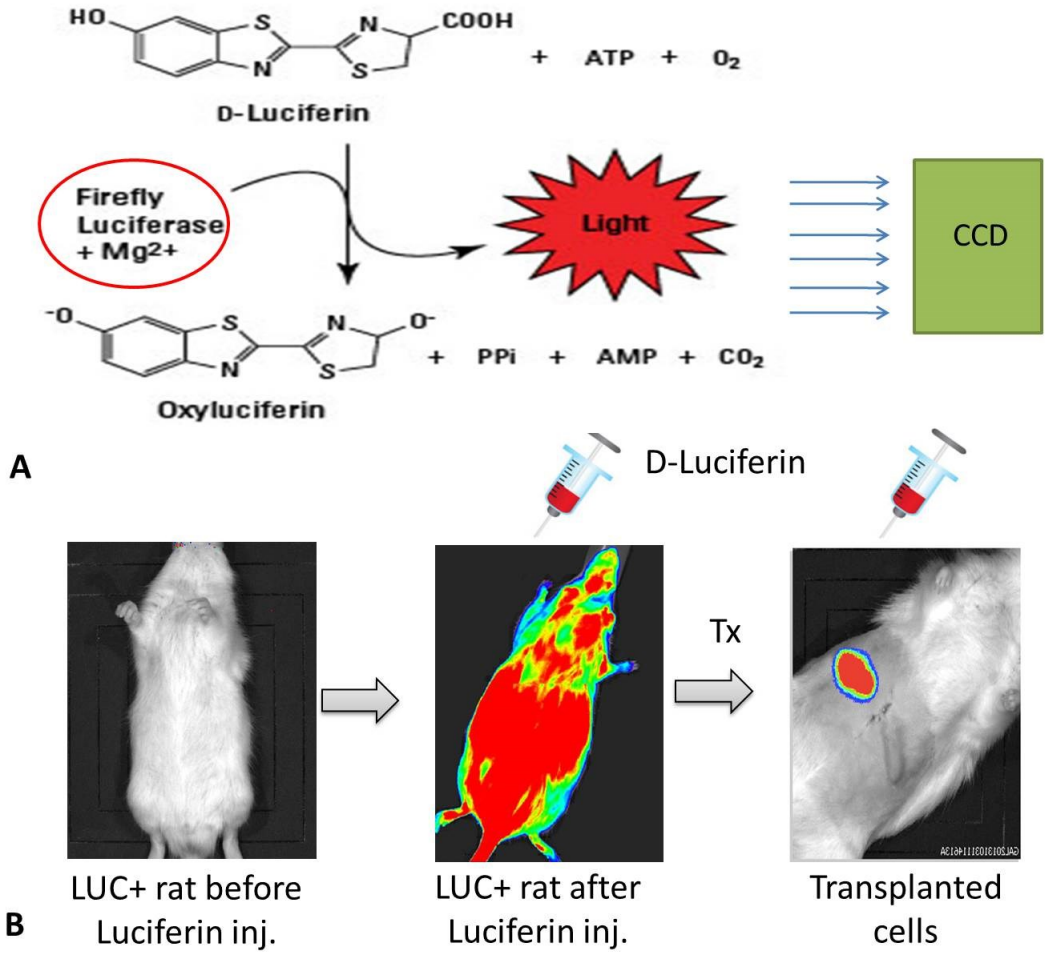

Fig. 3.9. Bioluminescence in experimental transplantation research. In a bioluminescence reaction, conversion of D-luciferin into oxyluciferin is catalyzed by luciferase (e.g. Firefly Luciferase). The created light is measured by a CCD chip (A). When the cells isolated from a bioluminescent rat (LUC+) are transplanted into a non-bioluminescent animal (LUC-), only transplanted cells produce light after D-luciferin administration (B).

Fluorescence

For generation of fluorescence, an external light with a specific wavelength (λ_{EX}) is needed to excite the electrons of a fluorophore to the higher energy level. Within a short time period, the electrons come back to the ground energy level and photons are released with a longer wavelength ($\lambda_{EM} > \lambda_{EX}$). The difference between the peak of excitation and emission light (Stokes shift) is around tens of nanometers. Fluorescence efficiency is defined by the fluorescence quantum yield Q that represents the ratio of photons absorbed (N_{ABS}) to photons emitted (N_{EM}):

$$Q = \frac{N_{EM}}{N_{ABS}} \tag{3.13}$$

The source of fluorescence in mammalian cells can be natural endogenous molecules (e.g., hemoglobin, flavins etc.), fluorescent proteins created by the genetically manipulated genes or exogenously administered fluorescent probes. Fluorescent proteins created upon expression of the reporter genes as e.g,. green (GFP) or red (RFP) fluorescent protein (DsRed) are widely used in molecular biology to target and visualize some specific cell structures. Up to now, a variety of fluorescent dyes have been synthetized including nanosized crystals called quantum dots, which excitation/emission wavelengths can be adjusted by their size (Mutavdžic et al. 2011). For *in vivo* applications, the NIR probes as e.g., cyanines (Cy5.5 or ICG) are preferred due to low absorption in the biological tissues.

Because of autofluorescence of natural fluorophores as nicotinamide, flavins, collagen and elastin (Bornhop et al. 2001) in the biological tissues, localization of the original light source can be hampered, what should be taken into account in an experiment. In some cases, tissue autofluorescence can be subtracted by conducting an additional experiment at the blue-shifted wavelengths or for the certain application; it can be suppressed by using a non-fluorescent food for animals.

Practical considerations and quantification of optical signal

The detected optical signal is influenced by measurement parameters: exposure time, lens aperture and binning. Optical signal is directly proportional to exposure time. Lens aperture controls the amount of the received light - by choosing a small aperture, less light is gathered but with higher image resolution. Fluorescence images are acquired with smaller aperture, while bioluminescence images with the open aperture. Binning refers to the

post-processing grouping of the pixels into a larger one (2 × 2, 4 × 4), what results in higher sensitivity and SNR and lower image resolution. To minimize influence of attenuation and scattering on the animal's surface, the fur should be removed. The animals with white fur (lower absorption by pigments) or naked ones are preferable for optical imaging.

Application of optical imaging for PIs tracking

For bioluminescence imaging of the transplanted PIs, isolated PIs are usually transduced *in vitro* by a virus vector (adenovirus, lentivirus) that expresses a luciferase gene under a control of a promoter as e.g., cytomegalovirus (Lu et al. 2004). Beta cell mass has been non-invasively visualized using a mouse insulin I promoter (MIP) (Park et al. 2005). In 2004, Lu at al. monitored virus-transduced rodent and human PIs transplanted under a kidney capsule in mice for 140 days (Lu et al. 2004). Localization of bioluminescent PIs transplanted in the liver and under the kidney capsule (Fowler et al. 2005) and the changes in PIs mass upon different diet in mice have been already reported (Chen et al. 2006). Bioluminescence has also helped to predict graft rejection in mice (Chen & Kaufman 2009).

Another way is the use of the transgenic animals that have expression for luciferase in all cells, what is a very advantageous approach for monitoring of cell transplantation (Hakamata et al. 2006).

Fluorescent dyes intended for labeling of PIs should emit light in NIR spectrum to avoid interference with tissue autofluorescence. As an example, transplanted PIs labeled with SPIO nanoparticles that were modified by Cy5.5 were tracked under the kidney capsule (Evgenov et al. 2006); however optical imaging was performed only for differentiation of labeled and non-labeled islets *ex vivo*. Fluorescence imaging has been also implemented for examination of complex cellular processes of PIs transplanted into an anterior eye chamber of animals (Speier et al. 2008).

Although optical imaging is not broadly applicable in clinical practice due to necessity of gene manipulation (bioluminescence) and low penetration of light through the tissues (bioluminescence and fluorescence), these methods help to reveal important biological processes in transplanted PIs and contribute to enhance the transplantation outcome.

3.3.4 Radionuclide imaging

Radionuclide imaging modalities, such as PET and SPECT, are based on detection of radioactivity (PET – positrons created via beta decay, SPECT – gamma rays) originating from the radio labeled tracers. Detection of radioactivity possesses higher sensitivity (detectability in pM range) compared to MR and at least similar to optical imaging; however spatial resolution is low and the accumulation of the tracer needs to be high. Another disadvantage is the need of a cyclotron (eg. ^{18}F, ^{13}N, ^{11}C) or a radionuclide generator (e.g. ^{68}Ga) in close proximity to the experimental facility. Various PET tracers have relatively short half-life (e.g. ^{18}F: 110 min, ^{11}C: 20 min, ^{15}O: 2 min) in comparison to SPECT tracers (6 hours to 8 days) that allow longer examination.

Mostly used approach for visualization of native beta cell mass (BCM) or transplanted PIs is direct targeting to a specific molecule on the islet surface as antigens or receptors. Variety of organic compounds have been suggested for BCM estimation and tracking of transplanted PIs, such as broadly tested exendin, which is a glucagon-like peptide receptor (GLP-1) agonist or the serotonin precursor ^{11}C-5-hydroxytryptophan (^{11}C-HTP) (Eriksson et al. 2014). Radiolabeled exendin was used to visualize transplanted PIs in the liver of T1DM patients by PET (Eriksson et al. 2016) and in a skeletal muscle by SPECT (Pattou 2010). Moreover, SPECT detection of ^{111}In-labeled exendin was efficient enough to differentiate between BCM of healthy volunteers and T1DM patients (Brom et al. 2014).

3.3.5 Ultrasound imaging

Transplanted PIs can be visualized also by ultrasonography, which is based on detection of sound waves that propagate through the body and reflect on the tissue boundaries with different acoustic impendence. PIs transplanted under the kidney capsule were visualized by ultrasonography and detected islet volume correlated with the number of islets (Sakata et al. 2012). Application of ultrasound CAs is limited due to poor spatial resolution and non-specificity of imaging probes (usually based on air bubbles).

3.3.6 Encapsulated probes

Microencapsulation of islets together with contrast probes has become a potential route for islet visualization. The capsules (usually alginate) allow diffusion of metabolites, but restrict antibodies and immune cell infiltration. Islets have been encapsulated with SPIONs for ^{1}H MRI (Barnett et al. 2007), with PFOB for ^{19}F MR, ultrasound and CT imaging (B P Barnett et al. 2011), with barium sulfate and bismuth sulfate for X-ray imaging (Barnett et al. 2006) or with Gd-gold or SPIO-gold nanoparticles for ^{1}H MRI, CT and ultrasound (Arifin et al. 2011).

3.3.7 Motivation for implementation of alternative probes

The reviewed imaging methods and CAs differ by means of applicability for tracking of transplanted PIs (see Tab. 3.3). In this thesis, we implemented MRI because of its non-invasiveness, high spatial resolution, tomographic capabilities, visualization of deep structures and possibility of using different contrast mechanisms. The conventional MR CAs containing gadolinium possess low sensitivity, unsuitable small size and could be toxic for cells. SPIONs as the most common CAs for PIs are safe, sensitive and as low as a single SPION-labeled cell can be visualized *in vivo*. A strong effect of iron nanoparticles on magnetization creates a so-called blooming artefact beyond the actual cell size that even increases sensitivity of visualization. On the other hand, the blooming artefact restricts absolute quantification of the cell number. A hypointense MR signal originating from the labeled islets may cause false positive data because of other sources producing the same or similar MR signal intensity in the biological systems. Moreover, SPIONs are taken up by macrophages, which may then contribute to false positive results limiting in the proper visualization of transplanted PIs. Although SPION-labeled PIs were successfully used for PI tracking also in clinical practice, SPION-based CAs are not approved for clinical applications in Europe anymore. Therefore, there is a need for novel sensitive and specific agents or approaches for tracking of transplanted PIs. In this work, we tested novel MR probes that have not been tested yet for labeling of PIs as CEST agents or specific PLGA nanoparticles containing fluorine (^{19}F). Highly sensitive optical imaging has been also implemented in the thesis to acquire more complex multimodal information about transplanted PIs.

Besides transplantation of islets in the liver, an alternative transplantation site was tested – polymeric scaffolds. The subcutaneously implanted scaffolds have already shown suitable properties for PIs transplantation, although with limited outcome. In this thesis, we implemented multimodal imaging approach (MRI and optical imaging) for optimization of transplantation protocol for PIs transplanted into the scaffolds.

	Advantages	Limitations
Radionuclide PET/SPECT agents	absolute quantification high sensitivity	low resolution ionizing radiation
MR SPIO nanoparticles	high sensitivity low toxicity	relative quantification low specificity negative MR signal
MR paramagnetic agents	positive MR signal clinically approaved low toxicity	low sensitivity small size (diffusion out of cells)
CEST MR agents	possibility of switch on/off more agents visualized in one experiment pH, temperature estimation	low sensitivity strong pH dependence signal quench in endosomes/lysosomes need for post-processing algorithms
^{19}F MR agents	high specificity absolute quantification	low sensitivity long acquisition time
CT agents	high sensitivity fast acqusition	low specificity ionizing radiation need of encapsulation
Ultrasound probes	fast acqusition cheap and simple	spatial resolution low specificity
Bioluminescence	only viable cells detectable high sensitivity fast acqusition	attenuation, scattering of light only a surface image (2D BLI) genetic manipulation low spatial resolution
Fluorescent dyes	high sensitivity fast acqusition	attenuation, scattering of light only a surface image (2D FLI) tissues autofluorescence

Tab. 3.3. Summary of advantages and limitations of different CAs for PI labeling.

4 Experimental part

In this chapter, experimental procedures and results of alternative visualization of pancreatic islets will be described and discussed. The section contains three studies focused on testing of CEST agents, visualization of genetically-modified bioluminescent islets and examination of multimodal nanoparticles suitable for ^{19}F MRI and fluorescence imaging. Each study is divided into Materials and Methods, Results, Discussion and Summary.

4.1 CEST agents for labeling of pancreatic islets

CEST approach has been already implemented in various applications. In our study, CEST agents were tested as novel contrast agents for labeling and visualization of PIs for the first time. The results of these experiments were summarized in two papers:

- Gálisová A, Jirák D, Krchová T, Herynek V, Fábryová E, Kotek J, Hájek M. Magnetic Resonance Visualization of Pancreatic Islets labeled by PARACEST Contrast Agents at 4.7T. Journal of Molecular Imaging and Dynamics (impact factor (IF) 2)
- Krchová T, Gálisová A, Jirák D, Hermann P, Kotek J. Ln(III)-complexes of a DOTA analogue with an ethylenediamine pendant arm as pH-responsive PARACEST contrast agents. Dalton Transactions 2016; 45(8):3486-96 (IF 4.0)

4.1.1 Materials and Methods

Preparation and characterization of the PARACEST agents

Two ligands with a different central atom europium Eu-DO3A-ae or ytterbium Yb-DO3A-ae (Fig. 4.2) with a suitable proton exchange rate between water and NH_2 groups were synthetized in the Department of Inorganic Chemistry of the Faculty of Sciences, Charles University in Prague. Briefly, the ligand H_3-DO3A-ae was prepared by reaction of t-Bu_3DO3A by alkylation with N-(2-bromoethyl)-phthalimide followed by sequential deprotection by trifluoroacetic acid and hydrazine. The ligand H3DO3A-ae was purified by chromatography on an anion exchanger and by crystallization from hot EtOH with 59% overall yield. The Ln^{3+}complexes of H_3DO3A-ae were prepared by mixing the ligand Ln^{3+}

chloride in small amount of distilled water. The complex was purified on Al_2O_3 column by chromatography. The pure product [Ln(DO3A-ae)] was eluted using a mixture of EtOH:H_2O:conc. aq. NH_3 (10:8:1) (Krchová et al. 2013). The concentration of the probes mentioned in the text refers to concentration of Eu^{3+} or Yb^{3+} in the molecule, respectively.

For MR characterization of these agents, T_1/T_2 relaxation times of the compounds solutions (40 mM) were measured on a 4.7 T scanner using a resonator coil (Bruker BioSpin, Germany) at the room temperature (25 °C). T_1 relaxation time was calculated from a series of images acquired by a spin echo sequence with a variable repetition time (*TR* = 6400/ 3200/ 1600/ 800/ 400/ 200/ 100/ 50 ms), echo time (*TE*) of 7.2 ms and acquisition time (*AT*) of 5 min per one image. T_2 relaxation time was measured by an imaging Carl Purcell Meiboom Gill (CPMG) sequence (*TR* = 5000 ms, *TE* = 7.2 ms, 256 echoes, *AT* = 21 min). The mean signal intensity from a selected ROI was assessed for each time point and it was fitted by a mono-exponential decay in the software GraphPad Prism (GraphPad Software Inc, USA). T_1 and T_2 relaxation times were calculated according to the formulas 3.2 and 3.3, respectively (p. 24).

To characterize the frequency offsets, Z-spectra of the PARACEST agents were obtained by acquisition of a series of images after saturation at variable frequency offsets ranging from -100 ppm to +100 ppm with the step of 2.5 ppm (81 images were acquired). For saturation, a Gaussian pulse (3000 ms/ 35 μT) was applied. A turbo spin echo sequence - RARE (Rapid Acquisition with Relaxation Enhancement) was used to acquire images with following parameters: *TR* = 5000 ms, *TE* = 6.4 ms, turbo factor = 16, matrix size of 128 × 128, the field of view (*FOV*) = 55 × 55 mm, 2 dummy scans, slice thickness of 2 mm and acquisition time of 40 seconds per one image.

Isolation and labeling of pancreatic islets

Pancreatic islets were isolated from Brown-Norway rats according to a standard protocol described by Gotoh (Gotoh et al. 1985). Briefly, the pancreata (2-3 donor rats per recipient) were excised and digested by intraductal injection of collagenase (1 mg/mL; 15 mL/rat). The tissue filled with collagenase was gently shaken at 37 °C for 20 min. Islet pellet was then carefully overlayered by polysaccharide Ficoll® solution (Sigma Aldrich, USA) of various concentrations - 1.037 g/mL, 1.069 g/mL, 1.096 g/mL and 1.108 g/mL. Following centrifugation of islets in the discontinuous Ficoll® gradient separates islets from the exocrine tissue. Islets were then hand-picked from the polysaccharide interlayer and incubated (37 °C, CO_2 atmosphere) in CMRL-1066 culture medium (PANBiotech GmbH,

Germany) supplemented with 5% HEPES buffer, 10% fetal bovine serum (FBS) and 1% of antibiotics penicillin/streptomycin/L/glutamine (all Sigma-Aldrich, USA).

After overnight incubation, islets were labeled either by pinocytosis or microporation. Labeling by pinocytosis was accomplished by incubation of islets in a culture medium containing dissolved CEST agents. Different numbers of islets were incubated in a 6-well plate (50 – 800 PIs) or in a 5 mL flask (1000 - 2000 PIs) for 12 or 24 hours; the wells contained Eu-/Yb- agents at concentrations 30, 45, 60, 80, 100 mM. The control islets (not microporated; 200 PIs) were incubated in the medium without the contrast agents.

Microporation was performed using the Neon^{TM} transfection system (Thermo Fischer Scientific, USA). 300 islets were mixed with the resuspension buffer R containing 60 mM or 100 mM of the CEST agents. Islets in 100 uL of the buffer were then placed into a container with the electrolytic buffer E2 and two 20 or 30 ms electric pulses were immediately applied. Various voltages ranging from 600 to 1000 V were tested. After poration, islets were transferred into a well containing the incubation medium and kept on ice for 10 min. Then, islets were placed into a 6-well plate and incubated overnight in 3 mL of culture medium without antibiotics at 37 °C.

After labeling, the islets were washed three times with phosphate-buffered saline (PBS), counted in a black well and hand-picked. For each labeling condition, 10 islets were evaluated for estimation of viability and 50 islets for assessment of insulin release in duplicates. For the MRI experiment, islets were placed into a dish containing 4% gelatin layer and overlaid with another 3% gelatin on the top. The exact numbers of islets in the phantoms are listed in the figure legends.

Viability assays and functional tests

Islet viability was evaluated after staining with acid-binding fluorescent dyes that refer about cell membrane integrity (Bank 1987). Ten handpicked islets were mixed with a 1:1 solution of propidium iodide (75 µmol/L) and acridine orange (9 µmol/L); after 5 minutes, 250 µL of PBS was added to dilute the solution and the islets were examined under a fluorescent microscope. The ratio of the viable cells to all cells inside each islet was assessed and expressed as an average percentage.

The functional potency of the islets was assessed using a glucose-stimulated insulin secretion test. Triplicates of 50 isolated islets were incubated in Krebs-Ringer bicarbonate buffer medium (37 ºC, 1 hour) at low (3.3 mM), high (22 mM) and low (again) glucose concentrations. Aliquots of the medium were removed and frozen at -20 ºC; insulin content

was measured using the ELISA test. The amount of insulin released upon glucose stimulation was assessed as the stimulation index, i.e., the ratio of insulin values measured after stimulation and before stimulation.

ICP-QMS measurements

The uptake of the complexes into islets was assessed by inductively coupled quadrupole plasma mass spectrometry (ICP-QMS). The labeled and control islets were washed three times with PSB, then digested by 250 μL of concentrated HNO_3 and dried in a desiccator (NaOH) equipped with a drying tube ($CaCl_2$) for 24 hours at 90 °C. The drying process was performed twice; then each sample was dissolved in 5 mL or 10 mL of 2% (v/v) HNO_3. The blank sample contained only 2% (v/v) HNO_3. ICP-QMS analysis was performed using a Thermo Scientific X Series II quadrupole ICP mass spectrometer. The uptake of the agents was estimated as a number of complexes incorporated in one islet. For assessment of the feasibility of islet visualization of the labeled islets, an approximate milimolar concentration of the agents in a suspension containing 1000 islets per 50 μL was calculated.

In vitro CEST MRI experiments of the labeled pancreatic islets

MR imaging was conducted on a 4.7 T MR scanner (Bruker BioSpin, Germany) using a resonator coil with a diameter of 7 cm (Bruker BioSpin, Germany). The parameters for CEST imaging were optimized in a separate experiment in advance (power and type of saturation pulses, readout parameters). Seven glass tubes containing 1.25 – 40 mM of each CEST agent dissolved in water were immersed in 4% gelatin (Fig.3 A, B). For CEST measurement, a modified RARE sequence was used: *TR* = 5000 ms, *TE* = 8.9 ms, turbo factor = 4, matrix size of 64 × 64, *FOV* = 55 × 55 mm, 2 dummy scans, slice thickness 2 mm, acquisition time of 1.5 min per one frequency offset (19 ppm, 34 ppm, 42 ppm, 89 ppm). The whole sequence was preceded by a saturation scheme consisting of a Gaussian pulse (3000 ms/35 μT). Contrast-to-noise ratio (CNR) was calculated for each concentration according to the formula

$$CNR = \frac{I(-)-I(+)}{\sqrt{\sigma^2(-)+\sigma^2(+)}}, \quad (4.1)$$

where *I(-)* and *I(+)* represent MR signal intensities in images acquired at negative or positive frequency offsets, respectively; $\sigma^2(-)$ and $\sigma^2(+)$ represent standard deviations from the same images (Liu et al. 2013).

The theoretical threshold $CNR_{threshold}$ for *in vivo* visualization according to Liu (Liu et al. 2009) is

$$CNR_{threshold} = 2\sqrt{2}. \quad (4.2)$$

The lowest detectable concentration, which generates CNR higher than this theoretical threshold, was determined for both CEST agents from CNR values experimentally assessed for various agent concentrations.

Islets labeled by both pinocytosis (60, 80, 100 mM) and microporation (100 mM) were examined by *in vitro* CEST imaging. The parameters for *in vitro* CEST imaging of islets were similar as for the phantom study with the solutions (*TR*/*TE* = 5000 ms/8.9 ms, turbo factor = 16, matrix size of 128 × 128, *FOV* = 55 × 55 mm, slice thickness of 2 mm); the spatial resolution was higher because of the size of islets (a small islet layer in the phantoms required smaller voxel size): slice thickness was 1 mm or 1.5 mm and two image resolutions were tested: 128 × 128 and 256 × 256. In the case of failure of detection of 300 islets (labeled with 80 and 100 mM) within 3.5 or 20 min per one frequency offset, the acquisition time was prolonged to 1 hour per one frequency offset.

CEST effect of 1000 islets labeled with 60 mM concentration of each CEST agent was measured by acquisition of the whole Z-spectrum. $\vec{\boldsymbol{B}}_{\boldsymbol{0}}$ inhomogeneities were corrected in each voxel by using WASSR approach (Kim et al., 2009). For both CEST and WASSR Z-spectra acquisition, a series of images was acquired using a standard CEST protocol. A saturation Gaussian pulse (2000 ms/25 μT) with variable frequency offsets ranging from -110 ppm to +110 ppm with the step of 2.5 ppm (89 images) was applied. Measurement time per one frequency offset was 3.5 minute (total measurement time was 5 hours). For WASSR acquisition, direct water saturation was accomplished with higher frequency resolution ranging from -1.5 ppm to +1.5 ppm with the step of 0.25 ppm using a 100 ms/0.5 μT Gausian pulse (13 images). All Z-spectra were processed by MATLAB software (Mathworks, USA). The data were interpolated up to 0.5 ppm (CEST) or 0.05 ppm (WASSR) resolution using a smoothing spline-based interpolation method.

CEST effect was expressed as the asymmetric magnetic transfer ratio (MTR_{ASYM}) (according to the equation 3.9, p. 33) and calculated from a ROI on the pixel wise basis. MTR_{ASYM} maps were reconstructed using a custom written script in MATLAB (Mathworks, USA) (Fig. 4.1). The script with comments can be found in the Appendix A. The maps were expressed in a false-color scale in percentage of MTR_{ASYM}.

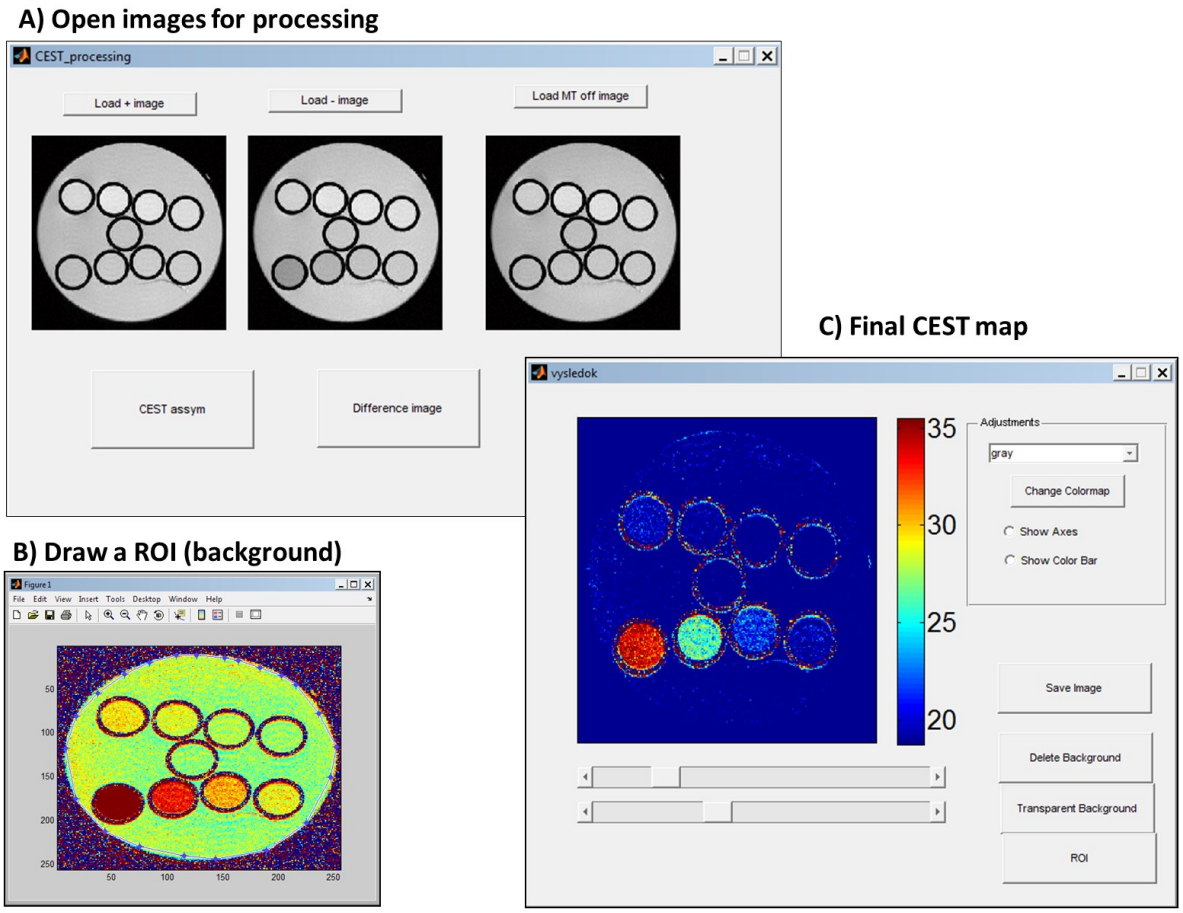

Fig. 4.1. An example of the home-made program for reconstruction of the CEST maps. The script written in MATLAB allows the choice of the raw images for analysis (A), and then a manually-drawn ROI can be chosen (B). In the last step, the final CEST map is calculated (C). The final image can be manipulated – color map, minimum and maximum of the scale showing MTR_{ASYM} values can be chosen. The background can be deleted or transparent. The final image can be saved as .jpeg/.png at the specific location.

4.1.2 Results

Characteristics of the CEST agents

Two specific peaks of each CEST agent were identified in their Z-spectra: for Eu-DO3A-ae at 19 ppm and 34 ppm; for Yb-DO3A-ae at 42 ppm and 89 ppm (Fig. 4.2). A solution of Eu-DO3A-ae agent of 50 mM concentration exploited higher CEST signal (47% MTR_{ASYM} at 19 ppm and 43% MTR_{ASYM} at 34 ppm) compared to Yb-DO3A-ae (8% MTR_{ASYM} at 42 ppm and 4% MTR_{ASYM} at 89 ppm). The Z-spectra showed that the peaks of Eu-DO3A-ae at 34 ppm overlap with the peak of Yb-DO3A-ae at 42 ppm. MR relaxivity

measurement revealed that the relaxation times of Eu-DO3A-ae (T_1 = 1436 ± 24 ms; T_2 = 480 ± 47 ms) are higher than Yb-DO3A-ae (T_1 = 599 ± 17 ms, T_2 = 331 ± 39 ms).

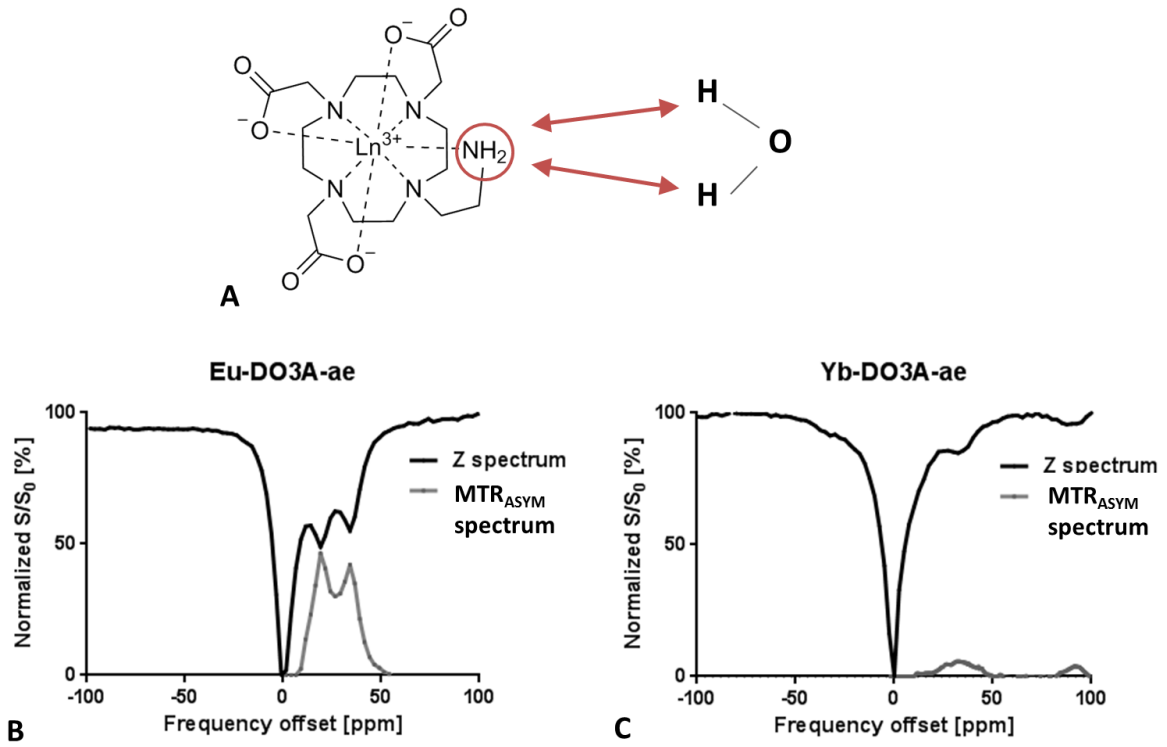

Fig. 4.2. Characterization of the CEST agents. A scheme of proton exchange between NH_2- group of the CEST agents with a central lanthanide (Eu/Yb) and bulk water (A). Z-spectra and MTR_{ASYM} spectra of Eu-DO3A-ae (B) and Yb-DO3A-ae (C) agents. The peaks in the spectra represent water saturation after irradiation of the complexes at specific frequencies as a result of slow exchange of labile protons between the amino groups of the complexes and bulk water.

CEST imaging of solutions of the CEST agents showed proportional dependence of MTR_{ASYM} on agent concentration (Fig. 4.3 G). Similarly as in the Z-spectra, Eu-DO3A-ae exploits higher CEST signal compared to Yb-DO3A-ae; 40 mM solution of Eu-DO3A-ae possesses approximately 30% MTR_{ASYM} in contrast to 8% MTR_{ASYM} of Yb-DO3A-ae. Calculated CNR values revealed that the minimal detectable concentration for imaging (above the detection threshold, according to the formula 4.2, p. 50) is 1.25 mM for Eu-DO3A-ae and 2.5 mM for Yb-DO3A-ae (Fig. 4.3 H).

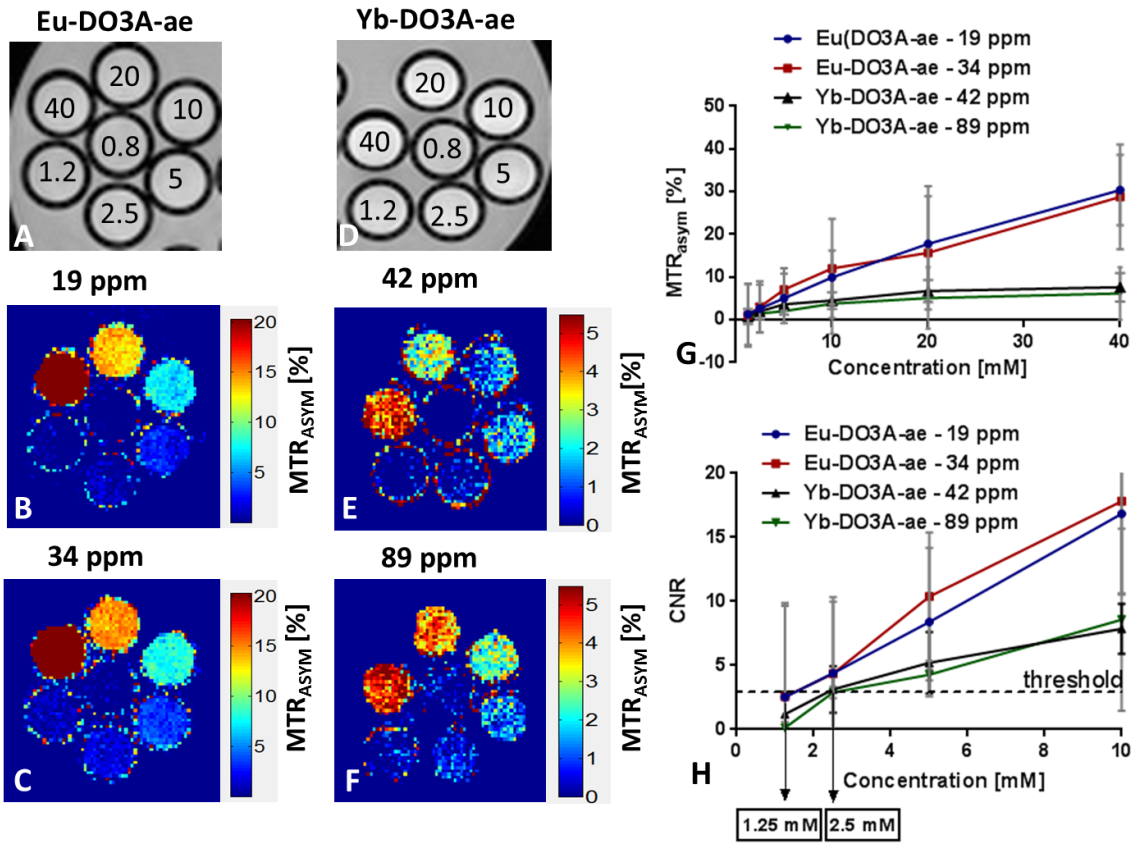

Fig. 4.3. MR characterization of the CEST agents. ^{1}H MR images and corresponding MTR_{ASYM} maps of a phantom containing various concentration of Eu-DO3A-ae (A, B, C) and Yb-DO3A-ae (D, E, F). MTR_{ASYM} maps of the agents were measured at specific frequency offsets: 19 ppm (B) and 34 ppm (C) for Eu-DO3A-ae, 42 ppm (E) and 89 ppm (F) for Yb-DO3A-ae. The numbers in the ^{1}H images represent milimolar concentrations of the agents. Graphs (G) and (H) show dependence of MTR_{ASYM} values and contrast-to-noise ratios (CNR) on concentration; the dotted line represents the detection *CNRthreshold* and the minimal detectable concentration, which can reach CNR above this threshold is highlighted in the box (Gálisová et al. 2016).

Labeling of pancreatic islets by CEST agents

PIs were labeled with the CEST agents using pinocytosis and microporation. The agent uptake in the islets after labeling by pinocytosis was in the range of $8.3 \times 10^{12} - 2.9 \times 10^{14}$ complexes per one islet. The use of a higher concentration of the CEST agents for pinocytosis led to higher cellular uptake of both complexes (Fig. 4.4 A, B). Similarly, 24-hour incubation resulted in higher agent internalization in the islets compared to 12 hours (Fig. 4.4 A, B). Labeling by microporation led to incorporation of maximum of 2×10^{13} of complexes per islet that is lower amount than using pinocytosis with 30 mM

of the agents for 24 hours (Fig. 4.4 C). Only labeling by pinocytosis with 80 mM concentration of CEST agents exceeded the detection threshold.

High concentrations of CEST agents in the culture medium during incubation had negative impact on islet viability (Fig. 4.5 A). By using concentration above 60 mM for 24-hour incubation, viability of islets decreased below 70%. Islet viability above 80% was reached by using shorter incubation time (12 hours) or with concentrations below 45 mM. Similarly, insulin secretion of islets, which were labeled with agent concentration 60 mM or higher was impaired (Table 4.1). Viability of microporated islets was approximately 80%; however, the amount of harvested islets was only about 30% of the initial mass. Viability of a control unlabeled sample was >95%, with the stimulation index >2.

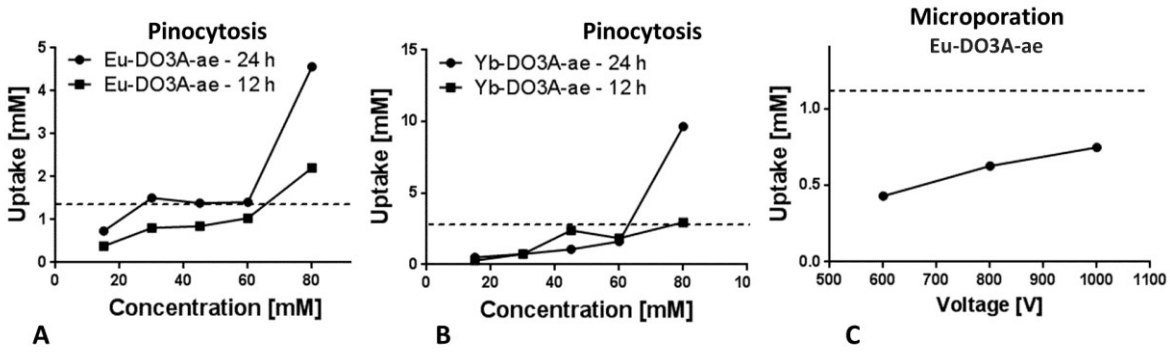

Fig. 4.4. Uptake of the CEST agents into pancreatic islets. Islets were labeled by pinocytosis using various concentrations of Eu-DO3A-ae (A) or Yb-DO3A-ae (B) in the incubation medium and by microporation using different voltage (C). The means and standard deviations (SD was below 1%) were calculated from approximately 100 PIs. The dotted lines represent the detection threshold calculated from CNR of agent solutions (Gálisová et al. 2016).

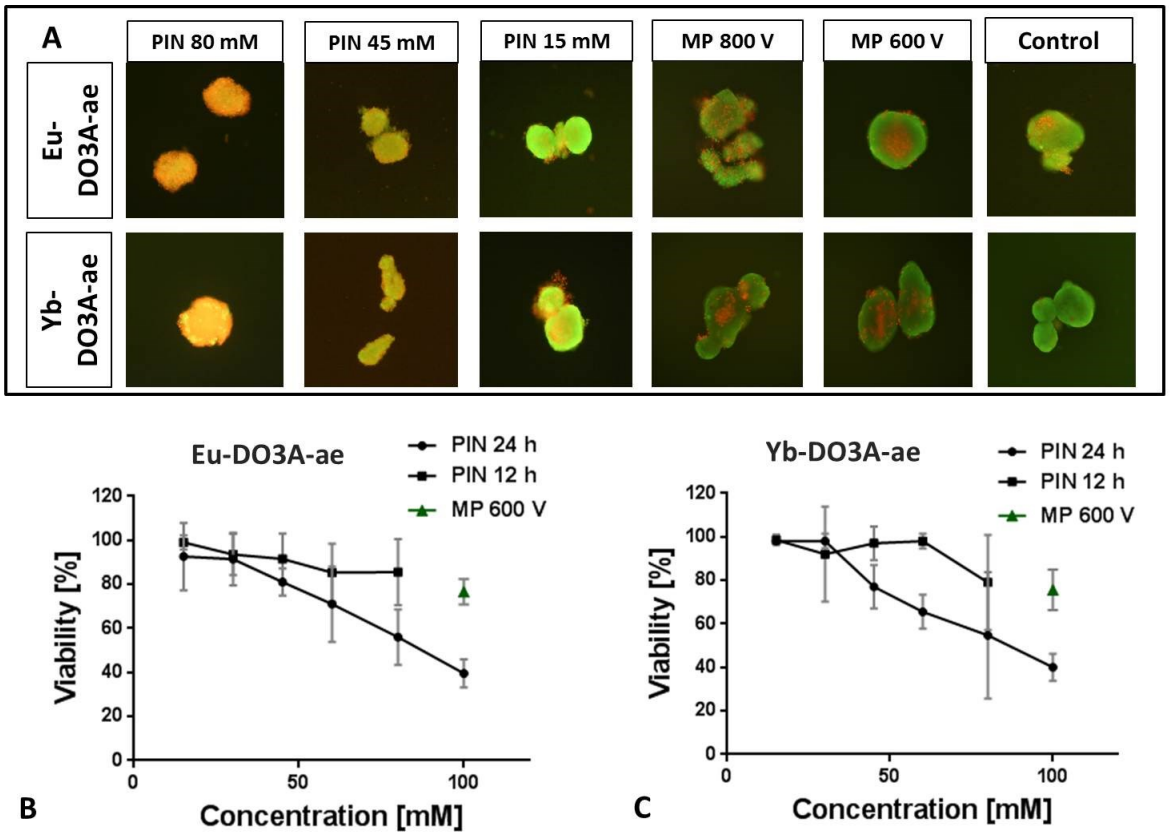

Fig. 4.5. Viability assessment of labeled pancreatic islets. Representative fluorescence images of islets after staining with acridine orange and propidium iodide (A). Green color refers to viable cells, red color to dead cells. Distribution of dead cells in the labeled islets was different for pinocytosis and microporation – the porated islets had dead cells mostly in the islet center in comparison to pinocytosis, where dead cells were detected at the islet surface. The results of quantification of viability of islets labeled with Eu-DO3A-ae (B) and Yb-DO3A-ae (C) (Gálisová et al. 2016).

PARACEST complex	Concentration [mM]	Stimulation index	SD
Eu-DO3A-ae	45	2.1	1.6
	60	2.1	1.3
	80	0.6	0.2
Yb-DO3A-ae	45	1.2	0.2
	60	2.0	1.8
	80	0.9	0.1
Control	0	2.1	1.5

Table 4.1. Insulin secretion by labeled pancreatic islets. Average glucose stimulation indexes corresponding to insulin production of pancreatic islets labeled with various concentrations of the PARACEST agents by pinocytosis. SD refers to standard deviation.

Visualization of pancreatic islets labeled with the CEST agents

Pancreatic islets labeled with the higher concentration of the agents (80 - 100 mM) were measured in a gelatin phantom at first. In this experiment, no CEST signal from the labeled islets was detected within 20 minutes of acquisition per one frequency offset (Fig. 4.6 B, C). After prolongation of acquisition time up to 1 hour per one frequency offset, 200 - 300 islets labeled either by 80 and 100 mM of CEST agents were detected (Fig. 4.6 E, F). Using 100 mM of the agent for labeling, 20% MTR_{ASYM} signal was detected from islets labeled with Eu-DO3A-ae, while only 4% of MTR_{ASYM} signal was observed from islets labeled with Yb-DO3A-ae (Fig. 4.6 E, F). Islets labeled with 80 mM of Eu-DO3A-ae provided about 8% MTR_{ASYM} (Fig. 4.6 H) and islets labeled with 80 mM of Yb-DO3A-ae were not detected (Fig. 4.6 I). No CEST signal was detected from islets microporated with 100 mM of the CEST agents within 1 hour of acquisition (Fig. 4.6 E, F). It should be mentioned that only a part of islets survived microporation, therefore only up to 170 microporated islets were transferred to a phantom for imaging. Islets labeled with Yb-DO3A-ae provided also low CEST effect (approximately 10%) after Eu-specific irradiation at 34 ppm and similarly islets labeled with Eu-DO3A-ae showed low MTR_{ASYM} values (4%) after Yb-specific irradiation at 89 ppm (Fig. 4.6 E, F).

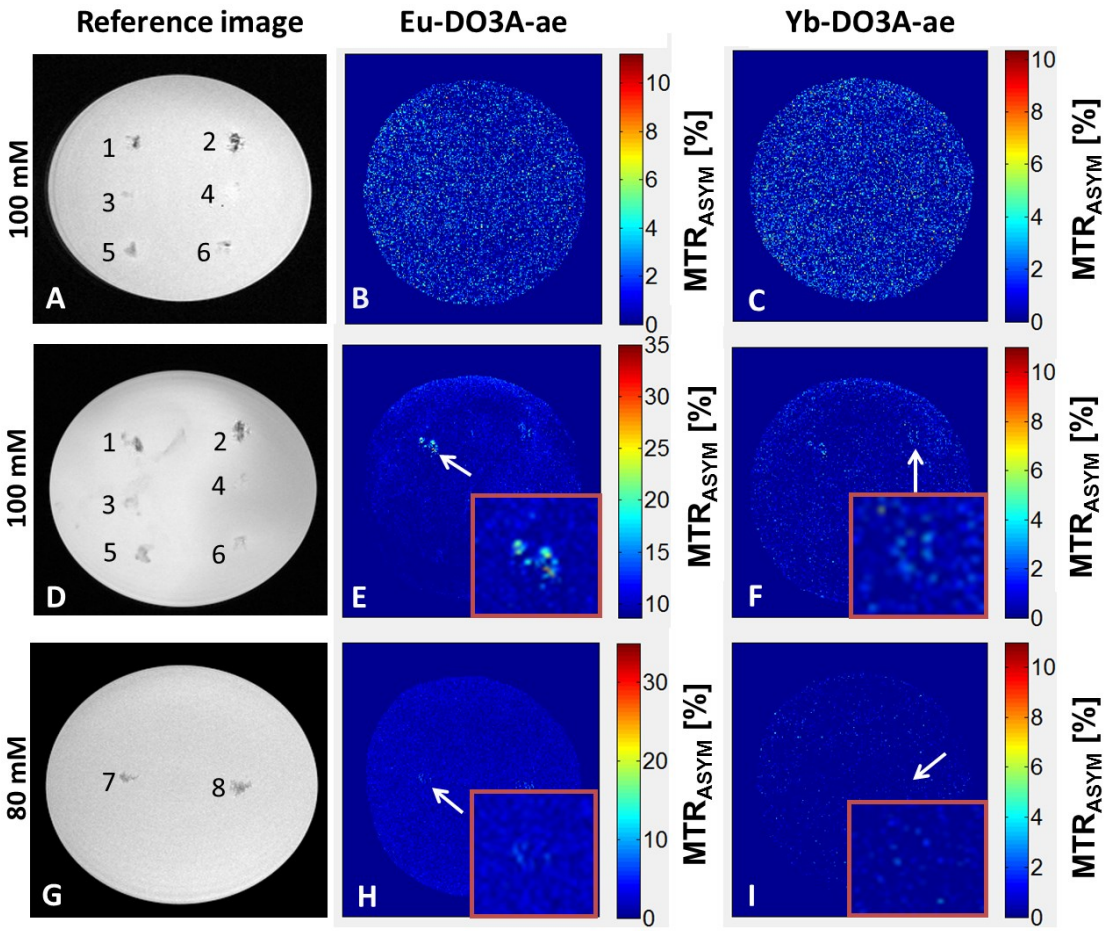

Fig. 4.6. ***In vitro*** **CEST MRI visualization of labeled pancreatic islets in a gelatin phantom.** A reference MR image of a gelatin phantom containing labeled pancreatic islets (A, D, G). MTR_{ASYM} maps of the phantom with saturation at 34 ppm for Eu-DO3A-ae (B, E, H) and with saturation at 89 ppm for Yb-DO3A-ae (C, F, I). Labeling conditions for each group: (1) pinocytosis Eu-DO3A-ae, 300 PIs; (2) pinocytosis Yb-DO3A-ae, 380 PIs; (3) microporation Eu-DO3A-ae 800V for 20 ms, 60 PIs; (4) microporation Yb-DO3A-ae 800V for 20 ms, 60 PIs; (5) microporation Eu-DO3A-ae 800V for 30 ms, 150 PIs; (6) microporation Yb-DO3A-ae 800V for 30 ms, 170 PIs; (7) pinocytosis Eu-DO3A-ae, 200 PIs; (8) pinocytosis Yb-DO3A-ae, 200 PIs. Measurement time per one frequency offset: B, C – 20 min; E, F – 1 hour. The arrows mark the islets, which should be visualized at the chosen frequency offsets and the detailed images of these islets are shown in the insets (Gálisová et al. 2016).

The use of higher concentration of the CEST agents for labeling of pancreatic islets led to cell viability and functionality impairment; therefore we tested also visualization of higher number of islet labeled with 60 mM agent concentration by pinocytosis. To improve sensitivity of CEST detection, the WASSR approach was used for B_0 inhomogeneities correction. The final CEST images were calculated by subtraction of the images at the (+/-)

offset, although the images originated from the corrected Z-spectra. In this experiment, 1000 islets labeled with 60 mM of Eu-DO3A-ae reached 6% MTR_{ASYM} at 19 ppm and 2% MTR_{ASYM} at 34 ppm. The islets labeled with Yb-DO3A-ae exploited less than 1% MTR_{ASYM} at 42 ppm and approximately 2% MTR_{ASYM} at 89 ppm (Fig. 4.7). The signal originated from the labeled islets was similar to the signal of a reference containing 2 mM of each CEST agent. No CEST signal was observed from the unlabeled control islets.

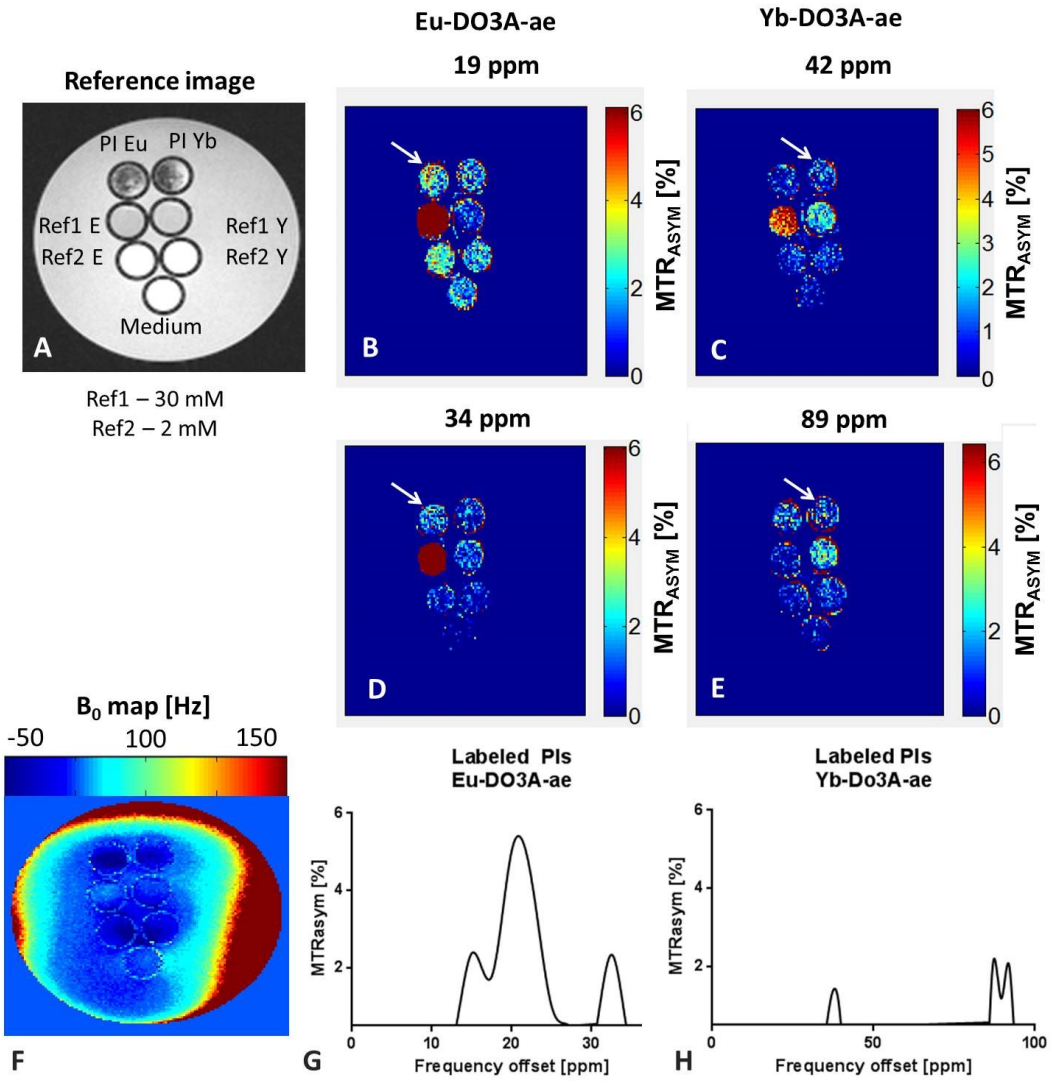

Fig. 4.7. *In vitro* visualization of labeled pancreatic islets in PBS. The reference MR image of the phantom (A). PI Eu refers to islets labeled with Eu-DO3A-ae and PIs Yb refers to islets labeled with Yb-DO3A-ae. The reference samples contain the agent solutions or incubation medium. MTR_{ASYM} maps of 1000 labeled islets obtained by saturation at various frequency offsets: 19 ppm (B), 34 ppm (C), 42 ppm (D) and 89 ppm (E). A representative B_0 map (F) and corresponding Z-spectra of islets labeled with Eu-DO3A-ae (G) and Yb-DO3A-ae (H). Islets were labeled by pinocytosis using 60 mM concentration of the complexes. Measurement time per one frequency offset was 3.5 minute. The arrow points the islets, which were selected for visualization at the chosen frequency offsets.

4.1.3 Discussion

CEST approach represents a novel contrast mechanism with some advantages for cellular labeling and visualization compared to the conventional superparamagnetic and paramagnetic agents. The tested Eu-/Yb-based chelates can serve as exogenous CEST agents due to a slow exchange between protons of their amino groups and bulk water (Krchová et al. 2013) resulting in two saturation peaks detected at different frequency offsets. Various saturation offsets allow specific identification of the agents (labeled cells or pancreatic islets) in one MR experiment, although the peaks of Eu-DO3A-ae (at 34 ppm) and Yb-DO3A-ae (at 42 ppm) chelates overlap and therefore these peaks are not optimal for differentiation of the agents. Nevertheless, the peaks at 19 ppm (Eu-DO3A-ae) and 89 ppm (Yb-DO3A-ae) could still serve for this purpose. Importantly, the chemical structure of the tested CEST agents is similar to the clinically approved MRI contrast agents (e.g., Gd-HPDO3A – ProHance® or Gadovist®), which is advantageous for their possible clinical application. Moreover, the saturation peaks exploit a large chemical shift from water, which minimizes direct water saturation and therefore is preferable for *in vivo* measurements. Because of the distinguishable irradiation offsets of our tested CEST probes with a large shift from the water, we hypothesize that the agents can be feasible for differentiation of islets according to size or drug modification.

The CEST MR experiment involving the contrast agent solutions showed that the Eu-based agent had higher CEST effect compared to the Yb-based analogue at both saturation offsets. Lower relaxation times of Yb-DO3A-ae may contribute to its lower MTR_{ASYM} values. Better sensitivity of Eu-DO3A-ae allowed reaching the detection threshold using lower concentration compared to Yb-DO3A-ae.

In this study, two labeling methods were tested for PIs labeling – pinocytosis and microporation. Microporation allows cytoplasmic uptake of the agents that is favorable due to higher pH and lack of additional endosomal membrane. The labels taken up by pinocytosis are entrapped in endosomes, where lower pH and the endosomal membrane could quench the CEST signal (Terreno et al. 2006). In spite of mentioned advantages of microporation, this method did not lead to sufficient agent uptake for *in vivo* visualization in our study. Moreover, the procedure was harmful to islets and viability of islets subjected to microporation decreased below 80%. In other studies, microporation has been applied for transfection

of various cells types (Lim et al. 2010); however according to our results, it is not suitable for labeling of PIs using the CEST agents.

In the case of pinocytosis, only labeling at concentration of 80 mM of both agents exceeded the detection threshold, although viability of labeled PIs was impaired suggesting a detrimental effects of the probes on cells. This effect was manifested also by impaired insulin secretion of labeled islets. Sufficient viability and function of PIs was maintained at concentrations lower than 45 mM only; although this concentration did not reach the detection threshold. Islets labeled by pinocytosis within longer time (leading to higher uptake of the complexes in PIs) expressed lower viability probably due to longer and higher exposure to the adverse impact of the contrast agents. A slow release of a toxic lanthanide ion under acidic condition (pH<6) has been already reported (Krchová et al. 2013) and we propose that the same effect occurred in endosomes during pinocytosis. Moreover, endosomes containing the agents could be fused with lysosomes, which pH is even more acidic.

CEST MRI experiment proved feasibility of *in vitro* visualization of PIs labeled with Eu-DO3A-ae and Yb-DO3A-ae chelates; however long acquisition time limits their use for *in vivo* application. PIs labeled with higher agent concentration showed higher CEST effect compared to lower concentration, which was in accordance to the higher content of the agent measured by ICP-QMS. PIs labeled with 80 and 100 mM concentration were visible after 2 hours of acquisition reaching high CEST signal ($MTR_{ASYM} \approx 20\%$); however corresponding viability impairment and long acquisition times were unacceptable for *in vivo* applications. In a similar study (Ferrauto et al. 2013), the macrophages and murine melanoma cells were successfully visualized after labeling by 100 mM of Eu- and Yb-HPDO3A agents and viability of the labeled cells was not compromised. It is worth to note that the agents and the cell line used in this study were different to ours; pancreatic islets are non-phagocytic, fragile and with a more complex structure than the individual cells. Moreover, cells were visualized at 7 T using a microimaging probe that is more sensitive than 4.7 T used for the PI experiment. Although the *in vitro* signal from the labeled cells was approximately 15 - 20% MTR_{ASYM}, the *in vivo* signal reached 3% or 6% $MTR_{ASYM,}$ what is comparable to our results. In another study, *in vivo* visualization of Eu-/Yb-HPDO3A-labeled neural stem cells and endothelial cells was reported in an animal model of stroke at 9.4T (Nicholls et al. 2015). Similarly to our study, *in vitro* CEST signal from labeled cells was 1% or 12% for Eu- and Yb-labeled cells, respectively. Although differentiation of two different cell lines *in vivo* was reported, the difference between labeled and unlabeled cells was only 3.27% in the case of Eu-labeled cells and 1.16% for Yb-labeled cells. In the same work, the authors discussed

a reduction of the CEST effect after incorporation of the agents into the cells in comparison to the signal originating from the solutions. This effect also indicates low sensitivity of visualization of cells labeled with the CEST agents.

Because of decreased viability of PIs after labeling by 80 – 100 mM of the agents, higher amount of islets (1000 PIs) and lower concentration (60 mM) were used for further tests. Despite usage of the WASSR approach for correction of B_0 homogeneity and higher number of examined islets, only a small MTR_{ASYM} values (below 6% MTR_{ASYM}) were observed from the labeled islets. Moreover, WASSR approach and acquisition of the full Z-spectrum prolonged the acquisition time up to 5 hours that is unacceptable for routine *in vivo* examination. Low MTR_{ASYM} values originating from Yb-labeled islets after Eu-specific irradiation is caused by overlapping of the irradiation peaks of both agents in the Z-spectra. Low CEST signal of Eu-labeled PIs measured at Yb-specific frequency may correspond to a statistical error.

In summary, decrease of CEST effect in endosomes after labeling by pinocytosis together with impairment of islet viability after labeling by higher concentration of the agents and low signal originating from PIs labeled at low concentration, make the CEST agents at current experimental setting unsuitable for *in vivo* application in PIs labeling and visualization. The obtained results are in accordance with the published data acquired at higher magnetic fields and processed by a complex post-processing and simulation approaches. However, improvement of agent properties (pH stability and toxicity) may allow further applications.

4.1.4 Summary – CEST contrast agents

- Labeling of pancreatic islets with the Eu/Yb-based CEST agents was more efficient in the case of endocytosis compared to microporation
- Long acquisition times and the use of high labeling contrast agent concentration is needed for sufficient visualization of labeled islets
- High concentration of the CEST agents impaired islet viability and functionality
- Islets labeled with lower agent concentration were visualized only for long acquisition times, what is unsuitable for *in vivo* measurements
- Our findings of low sensitivity of CEST for cellular imaging correspond to published data

4.2 Visualization of transplanted pancreatic islets by bioluminescence imaging

In this study, multimodal imaging including bioluminescence and MRI were implemented for long-term *in vivo* tracking of transplanted islets in artificial scaffolds in order to test this novel transplantation site and to optimize the transplantation protocol. The experiment was preceded by several pilot and optimization experiments focused on examination of the effect of mesenchymal stem cells (MSCs) on vascularization of the scaffolds and proper timing of PIs transplantation.

The results of these experiments were published in three papers:

- Gálisová A, Fábryová E, Jirák D, Sticová E, Lodererová A, Herynek V, Kříž J, Hájek M.. Multimodal imaging reveals improvement of blood supply to an artificial transplant site induced by bioluminescent mesenchymal stem cells. Molecular Imaging and Biology 2016 (IF 3.4)
- Gálisová A, Fábryová E, Sticová E, Kosinová L, Jirátová M, Herynek V, Berková Z, Kříž J, Hájek M, Jirák D. The optimal timing for transplantation of pancreatic islets in artificial scaffolds assessed by multimodal imaging. Contrast Media and Molecular Imaging 2017 (IF 3.3)
- Fabryova E, Jirak D, Girman P, Zacharova K, Galisova A, Saudek F, Kriz J. Effect of Mesenchymal Stem Cells on the Vascularization of the Artificial Site for Islet Transplantation in Rats. Transplantation Proceeding 2014; 46:1963-1966 (IF 0.9)

4.2.1 Materials and Methods

Isolation and characterization of MSCs

MSCs were isolated from the visceral adipose tissue of epididymal and perirenal areas of rats. Briefly, fat tissue from the epididymal and perirenal areas was excised, washed twice with cold PBS and centrifuged (500g, 5 min) after each wash. The rinsed tissue was digested by collagenase (1340 PZS/g, 1 mg/ml; Sevapharma, Czech Republic) for 30 min at 37 °C. Digestion was terminated upon the addition of ice-cold fetal bovine serum (Sigma-Aldrich, USA) and the mixture was filtered through a 500-μm mesh. The suspension was then

centrifuged and washed three times (1000g; 10, 10 and 5 min) in PBS with 1% antibiotic-antimycotic solution (AAS) containing penicillin, streptomycin and fungizone (Thermo Fisher Scientific, USA). The tissue pellet was then resuspended in 3 mL of PBS with AAS and overlaid with 2 mL of Ficoll solution (1077 g/ml, Ficoll-Paque™ Premium, GE Healthcare Bio Science AB, Sweden). The cells in the interlayer were collected and then washed with PBS and cultured in DMEM low-glucose medium supplemented with 10% fetal bovine serum and 1% L-glutamine-penicillin-streptomycin solution (Sigma-Aldrich, USA). The culture medium was replaced twice a week and the cells were sub-cultured for 2 weeks after isolation. Prior to transplantation, the cells were released from the bottom of the culture flask by trypsinisation, dissolved in cold PBS, quantified and placed in a syringe.

Tens of thousands of cells from each set were examined by fluorescent-activated cell sorting (FACS). The cells were incubated with anti-mouse/rat CD29 antibody (Biolegend, USA), phycoerythrin/CD44 antibody (Abcam, UK), PE-Cy^{TM}5 mouse anti-rat CD45 antibody (BD Biosciences, USA), anti-rat/mouse CD90.1 (Thy-1.1) antibody (E-Bioscience, USA) and anti-mouse endoglin/CD 105 antibody (R&D Systems, USA) for 20 min. The cells were then washed with FACS solution (PBS, 0.2% fish skin gelatin, 0.01% sodium azide) and analyzed by flow cytometry (BD FACSCalibur, BD Biosciences, USA). The analysis revealed specific molecules on the MSC surface: CD29 in 95%, CD90 in 98% and CD105 in 54%.

Cells were differentiated into chondrocytes, osteocytes and adipocytes using a differentiation kit (RD Systems, USA) in order to assess the stem properties of isolated MCSs. Briefly, cells seeded in a 24-well plate (adipocytes, osteocytes) or a 15 mL tube (chondrocytes) were cultured in adipogenic, osteogenic and chondrogenic differentiation media, respectively, according to the manufacturer's instructions. After 21 days, adipocytes, osteocytes and chondrocytes were detected using immunocytochemistry staining for FABP4, osteocalcin and aggrecan, respectively.

To confirm luciferase expression in luciferase positive (LUC+) MSCs, different numbers of MSCs (0.6×10^5 - 1×10^6) were placed into a six-well plate and imaged for 1 min by an IVIS Lumina XR optical imager (Perkin Elmer, USA) after addition of 10 μL of D-luciferin (30 mg/mL).

Pancreatic islet isolation and characterization

Pancreatic islets were isolated from rats according to a standard isolation protocol described in the Chapter 4.1.1 (p. 47). Islets were manually counted using a dissection

microscope and collected in a small plastic tube connected to a syringe prior to transplantation.

Viability of islets before transplantation was evaluated after staining with the nucleic acid-binding fluorescent dyes propidium iodide and acridine orange as is described in the Chapter 4.1.1 (p. 48). The functional potency of the islets was assessed using a glucose-stimulated insulin secretion test as is also described in the Chapter 4.1.1 (p. 48).

Expression of the luciferase enzyme in isolated LUC+ PIs was confirmed using the optical imager. Various amounts of isolated islets (50, 100, 300, 600, 1000 PIs) were placed in the wells of a six-well plate and imaged for 1 minute after the addition of 10 μL D-Luciferin solution (30 mg/mL).

Animal models

In all experiments, polymeric scaffolds were prepared from a 0.3 mm thin non-degradable Silon monofilament mesh (ELLA-CS, Czech Republic). The mesh was sutured into a rounded form with a cavity inside (Fig. 4.8 A).

The rats were placed under general anesthesia (ketamine 36 mg/kg and dexmedetomidine 0.08 mg/kg; Vétoquinole, France and Orion Pharma, Finland) during all surgical procedures.

All animals were kept in a conventional breeding facility under a 12/12 light cycle regimen, with free access to pelleted food and water. The protocols related to the study were approved by the Ethics Committee of the Institute for Clinical and Experimental Medicine and the Ministry of Health of the Czech Republic in accordance with the European Communities Council Directive 86/609/EEC.

Enhancement of vascularization in the artificial scaffolds by LUC+ mesenchymal stem cells

The experiment focused on improvement of blood supply in scaffolds by MSCs and assessment of optimal transplantation window for pancreatic islets. Polymeric scaffolds were implanted into 6 non-diabetic LUC- Lewis rats (Velaz, Czech Republic). The scaffolds were supplemented with the small polytetrafluoroethylene rods inserted during scaffold implantation and removed after one week. Then 15 millions of LUC+ MSCs were injected into the experimental cavity; the second device served as a control without transplanted cells. The design of the experiment is shown in Fig. 4.8. Localization and viability of transplanted MSCs were measured by bioluminescence imaging. Vascularization

inside the scaffolds was assessed by the dynamic contrast enhanced (DCE) MR technique using the contrast agent Gadofosveset and by histology.

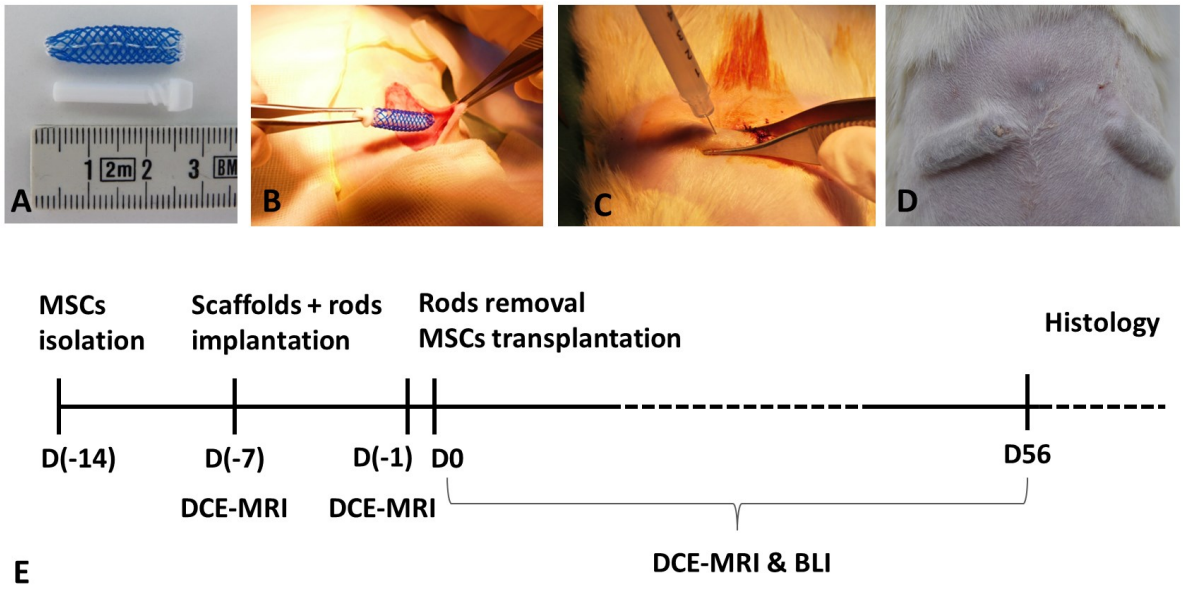

Fig. 4.8. Design of the experiment. A photograph showing a device consisting of a macroporous scaffold combined with a rounded rod (A). A photograph showing the implantation procedure of the scaffold into the subcutaneous space in the abdominal area of an animal (B), injection of MSCs through the skin and engrafted scaffold (C) and an animal with two implanted scaffolds (D). A schematic illustration of the timeline of the experiment (E). D in the scheme refers to a day after/before MSC transplantation (Gálisová, Fábryová, Jirák, et al. 2017).

Optimization of timing for transplantation of LUC+ PIs into scaffolds in diabetic rats

The goal of this experiment was to optimize the transplantation protocol for PIs in artificial scaffolds in diabetic rats. Two time points for PIs transplantation were tested – day 4 and day 7 after MSCs transplantation/ rod removal. The scaffolds were longitudinally examined by MR and bioluminescence imaging for 4 months after PIs transplantation. Vascularization and viability of the graft were assessed also by histology.

The bioluminescent (LUC+) and non-bioluminescent (LUC-) litters used in this study were the progeny of bioluminescent heterozygous Lewis rats. The bioluminescent rats were used as donors of LUC+ pancreatic islets and their LUC- littermates served as either recipients of the transplanted syngenic islets or as donors of LUC- MSCs. All recipients were

10-weeks old male rats weighing 250-300 g at the time of islet transplantation. Two or three rats were used as islet donors for one recipient.

Diabetes was induced by injection of streptozotocin (60 mg/kg, Sigma-Aldrich, USA) dissolved in cold 3.8% sodium citrate (pH 4.5) into the peritonea of the overnight-fasted recipient LUC- rats. One week later, 24 animals with confirmed diabetes (a minimum of 18 mmol/L blood glucose over 3 consecutive days) got subcutaneous implantation of macroporous scaffolds in the abdominal region. The scaffolds were implanted with polytetrafluoroethylene rods, which were removed from all scaffolds one week after implantation. The cavities were left to heal spontaneously or with 10 million LUC- MSCs, which were transplanted by 30G needle syringe injection. The cavities were closed using small polytetrafluoroethylene plugs.

The plugs were then removed and one thousand isolated LUC+ PIs were transplanted into the experimental scaffolds at two time points (4 or 7 days after rod removal) by injection using a syringe supplemented with a thin plastic tube for continuous injection. The animals were divided into experimental groups (n = 6 each): Group A – islets were transplanted on day 4 after rod removal without MSCs; Group B – islets were transplanted on day 4 after rod removal with MSCs; Group C – islets were transplanted on day 7 after rod removal without MSCs; Group D – islets were transplanted on day 7 after rod removal with MSCs. Animals in group A had implanted control scaffolds containing PBS injected on day 4 (group E) without any transplanted cells or islets. Animals in group C had implanted control scaffolds containing PBS injected on day 7 (group F) without any transplanted cells or islets. Both experimental and control scaffolds were treated in the same way and after surgery the scaffolds were covered by skin and tightly sutured. The design of the experiment is shown in Fig. 4.9.

To avoid a negative effect of hyperglycemia on oxygen consumption in beta cells, a slow-release insulin pellet (Linplant Sustained Release Insulin Implants, LinShin Canada, Inc., Canada; ≈2U/day/implant for > 40 days) was implanted subcutaneously in each animal at the time of scaffold implantation. The pellets were removed two weeks after islet transplantation in order to determine the effect of transplanted PIs on blood glucose levels.

The body weights of animals were measured and blood glucose levels monitored on a regular basis using an automatic blood glucose meter for the duration of the whole 4-month experiment. Normoglycemia was defined as a blood glucose level below 7.5 mmol/L.

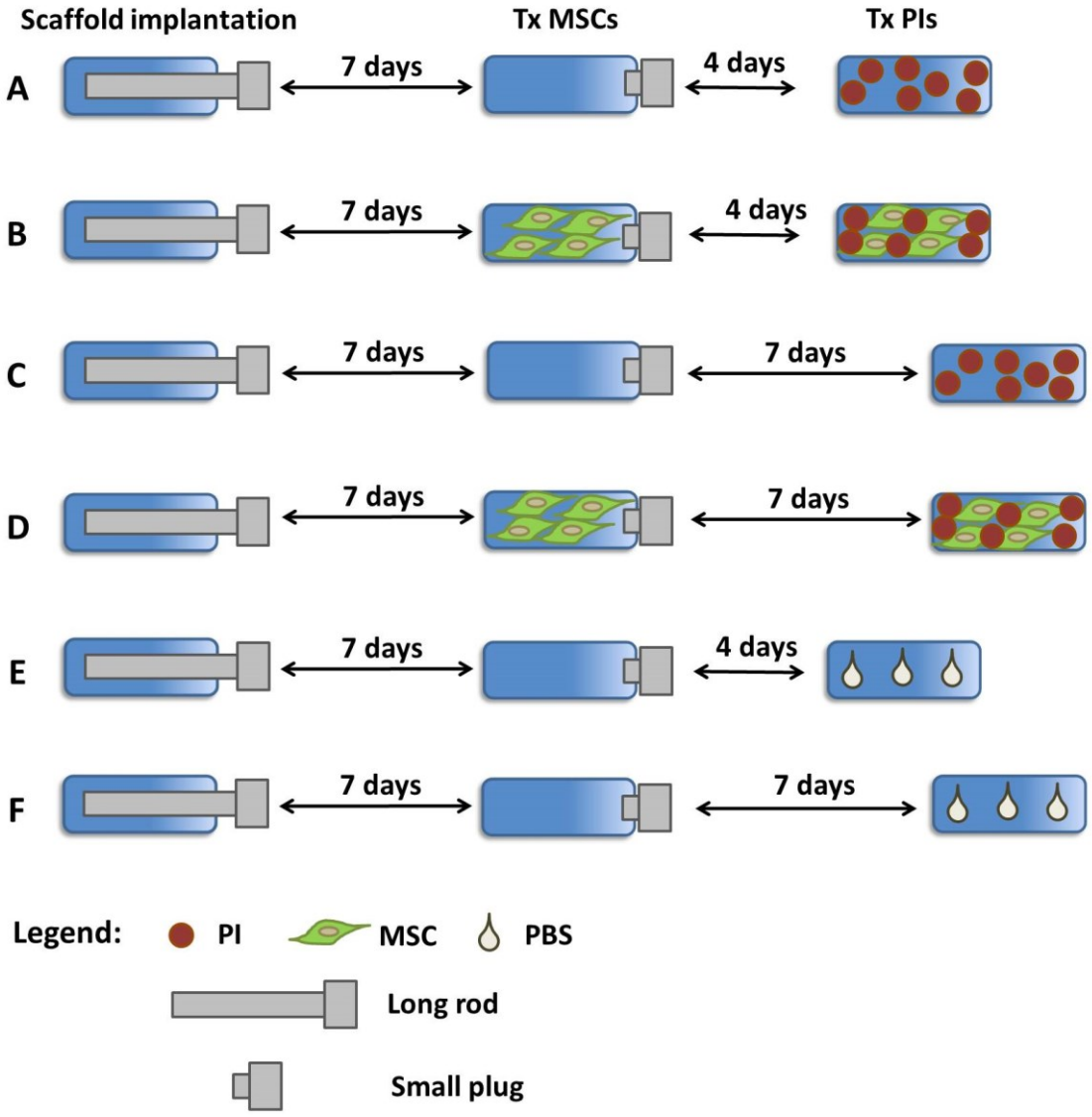

Fig. 4.9. Design of the experiment. Scaffolds were divided into 6 experimental groups (A – F) according to the day of transplantation (Tx) of mesenchymal stem cells (MSCs) or pancreatic islets (PI). Phosphate buffered saline (PBS) was added to the control scaffolds (Gálisová, Fábryová, Sticová, et al. 2017).

Magnetic resonance imaging

The animals were anesthetized by inhalation of isoflurane (Torrex, Austria) in air (5% for induction, 1% during the measurements). Animal body temperature was maintained using a heating system and breathing was monitored for the duration of all *in vivo* experiments. MRI measurements were carried out on a 4.7 T MR scanner (Bruker BioSpin, Germany) using a resonator coil with an internal diameter of 7 cm (Bruker BioSpin, Germany). Anatomical T_2-weighted images were acquired using a fast spin echo sequence

(*TR* = 3000 ms, *TE* = 12 ms, turbo factor = 8, *NA* = 4, time of acquisition *TA* = 5 min, spatial resolution 0.2 × 0.2 × 1 mm^3). For DCE MR measurements, a three-dimensional gradient echo sequence was used with the following parameters: *TR* = 10 ms, *TE* = 3.1 ms, spatial resolution 0.2 × 0.4 × 0.7 mm^3, 32 slices covering the scaffold volume, evolution delay = 2 s, temporal resolution 40 s and *TA* = 16 min. A MR contrast agent (0.05 mmol/kg gadofosveset in the experiment with LUC+ MSCs or 0.1 mmol/kg gadobenate dimeglumine in the experiment with LUC+ PIs) was administered after the 8^{th} cycle into the tail vein through a 24G catheter. For analysis, regions of interest (ROI) in MR images were outlined around the internal diameter of each device using ImageJ software (version 1.46r, National Institutes of Health, USA). The area under the curve (AUC) of the DCE MR signal was calculated within the first 160 s after administration of the contrast agent from the chosen ROI using GraphPad Prism 6.02 (GraphPad Software Inc, USA). The AUC was averaged from the 7 selected slices per time point.

In vivo bioluminescence imaging

The animals were placed in a dark chamber of the IVIS Lumina XR optical imager (Perkin Elmer, USA) in order to detect bioluminescence signals. Standard light photographs were taken for anatomical co-registration of the bioluminescent source. Optical images were measured before and after intravenous administration of D-luciferin dissolved in sterile PBS (50 mg/kg of body weight) with an exposure time of 1 minute, open aperture and open emission filter. The images were acquired from a time series lasting 14 minutes, while the area under the dynamic time curve was calculated using GraphPad Prism 6.02 (GraphPad Software Inc, USA) in order to minimize the variability of D-luciferin administration among the measurements.

Histology

The scaffolds with the tissue inside were removed from the animals at the end of examination (two months in the experiment with LUC+ MSCs; four months in the experiment with LUC+ PIs). The scaffolds were fixed overnight in 4% formaldehyde (pH 7.4) at 4 ^{0}C and embedded in paraffin blocks. Tissue sections (4 μm) were cut and routinely stained with hematoxylin and eosin (H&E) and Verhoeff-Van Gieson elastin stain. Immunohistochemical detection of CD31 (rabbit polyclonal, Acris Antibodies GmbH, Germany) and insulin (mouse monoclonal, MU029-UC, Biogenex, USA) was performed on 4-μm-thick paraffin sections. The primary antibodies were applied overnight at 4 °C.

The CD31 antibody was detected by biotinylated goat anti-rabbit IgG (H+L) (Vector Laboratories, USA), after which the sections were incubated with R.T.U. Vectastain Elite ABC Reagent (Vector Laboratories, USA) for 30 min. The Simple Stain MAX PO (MULTI) Universal Immuno-peroxidase Polymer anti-mouse, anti-rabbit Histofine (Nichirei Biosciences, Japan) was used to detect the primary anti-insulin antibody. Finally, the specimens were stained with the Dako Liquid DAB Substrate-Chromogen System (Dako, Czech Republic) and counterstained with Harris's hematoxylin.

Microvascular density (MVD) assessment was performed on serial sections from each scaffold. Two paraffin blocks were prepared from each sample; three serial sections per block were stained with the primary anti-CD31 antibody. MVD was evaluated in the area of the highest vascularization as a number of CD31-positive microvessels counted at a magnification of ×400 (i.e., ×40 objective lens and ×10 ocular; 0.2375 mm^2 per field). The results were expressed as the mean microvessel count with standard deviation.

Statistical analysis

Statistical analysis was conducted using GraphPad Prism 6.02 (GraphPad Software Inc, USA). The average DCE MRI signals of the control and experimental scaffolds were compared per time point using the unpaired two-tailed Student's t-test or, for the whole examination, using the paired t-test. Comparison between three groups (with and without MSCs and controls) was performed by analysis of variance (ANOVA). The significance level was set at $p < 0.05$. Mean values and standard deviations are presented in the graphs. Coefficient of determination (R^2) were calculated by regression analysis.

4.2.2 Results

Enhancement of vascularization in the scaffolds by LUC+ mesenchymal stem cells

The DCE MR measurements revealed significantly higher perfusion and vessel permeability in the scaffolds with MSCs compared to controls throughout the whole experiment (2 months) with the peak on day 9 after MSCs transplantation. Viable MSCs were tracked in scaffolds during the whole examination with maximum of the optical signal detected on day 3. After 2 months, the bioluminescence signal stayed at approximately 10 – 15 % of the maximal signal level. The stable optical signal was detected in 1 animal even 16 months after MSC transplantation. Histology confirmed higher vascularization (higher content of VEGF and more endothelial structures assessed by MVD) in the scaffolds with MSCs (Fig. 4.10).

The optimal window for PIs transplantation in terms of maximal vascularization (assessed by MRI) and viability or the transplanted MSCs (bioluminescence) therefore lies between day 3 and day 9 (Fig. 4.11).

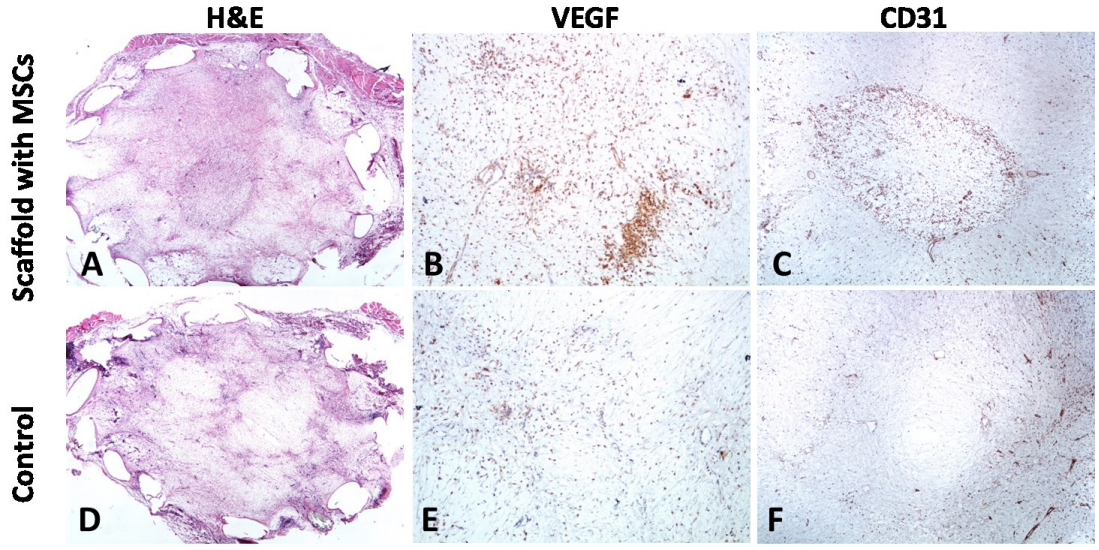

Fig 4.10. Histology of scaffolds with transplanted LUC+ MSCs. Representative histological images of scaffolds with (upper row) and without MSCs (bottom row) stained by hemtoxylin-eosin (H&E) (A, D), antibody to VEGF (B, E) and CD31 (C, F). Higher content of VEGF and more endothelial structures were found in scaffolds with MSCs in comparison to controls.

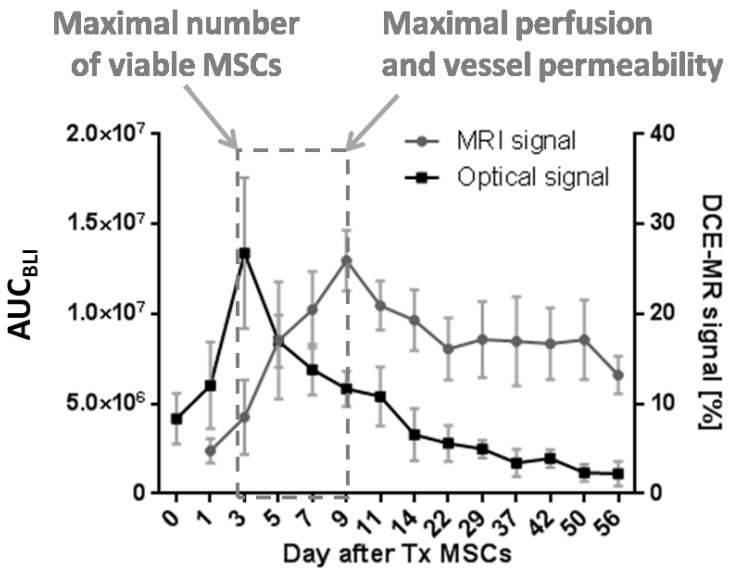

Fig. 4.11. Time window for transplantation of PIs in scaffolds. Assessment of optimal condition in the artificial scaffolds by means of vascularization (assessed by DCE MRI) and graft viability (assessed by bioluminescence imaging). The optimal time window with superior vascularization and islet viability was found between day 3 and 9 after MSCs transplantation (Gálisová, Fábryová, Jirák, et al. 2017).

Optimization of timing for transplantation of LUC+ PIs into scaffolds in diabetic rats

In vitro examination of LUC+ pancreatic islets

All isolated LUC+ pancreatic islets emitted photons following the addition of D-luciferin into the incubation medium due to luciferase expression. A linear relationship between the number of isolated PIs and the optical signal was found (coefficient of determination $R^2 = 0.98$) (Fig. 4.12).

The viability of the islets assessed by staining with fluorescent dyes was > 95% prior to transplantation. The mean of the stimulation index was greater than 5 in all groups.

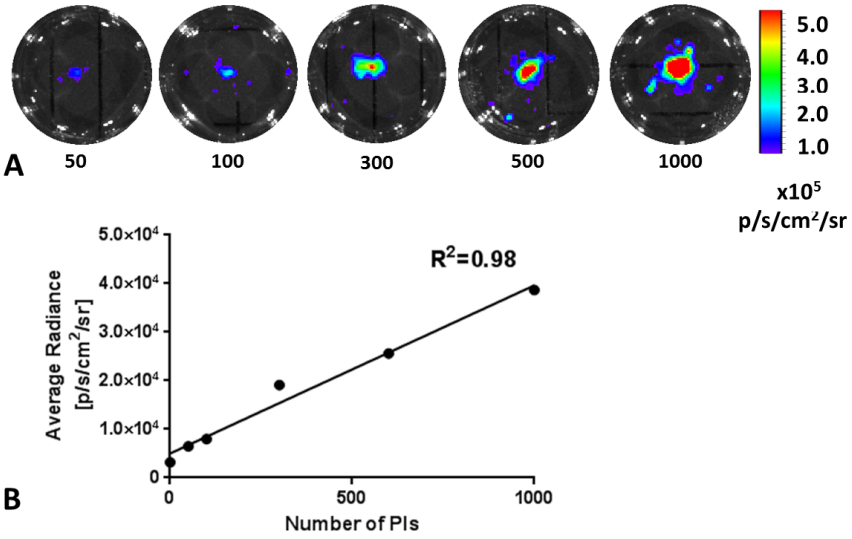

Fig. 4.12. *In vitro* characteristics of isolated PIs. Bioluminescence images (superposed on photography) of isolated LUC+ PIs (A); the numbers below the images represent the amount of PIs in the well. Quantification of optical signal originating from different number of isolated PIs (B) (Gálisová, Fábryová, Sticová, et al. 2017).

Animal model

No adverse macroscopic effects of scaffolds on the surrounding tissue were observed. There was no visible sign of inflammation, seroma, or macrophages migration on the day of scaffold retrieval and no perforation into skin or peritoneum during the whole examination. The scaffolds were removed from animals without causing of massive bleeding or other macroscopic damage. Scaffolds exploited higher level of vascularization at the site closer to subcutaneous space compared to the site close to the muscle; therefore removal of the devices did not cause any harmful effect to the muscle tissue.

Diabetes was reversed in all animals without MSCs; four animals from groups B (n = 2) and D (n = 2) remained hyperglycemic (Fig. 4.13 A). The percentage of euglycemic animals at the end of study was 100% in group A, 67% in group B, 100% in group C and 60% in group D (one animal from the group D died during examination and it did not reach long-term normoglycemia). Animals with non-functional grafts remained hyperglycemic since the removal of the insulin pellet until the end of the examination. Normoglycemia in animals with functional grafts was sustained for 4 months after removal of the insulin pellet. The body weights of animals with functional grafts increased regularly after PIs transplantation, while animals with non-functional grafts did not gain weight after PIs transplantation (Fig. 4.13 B).

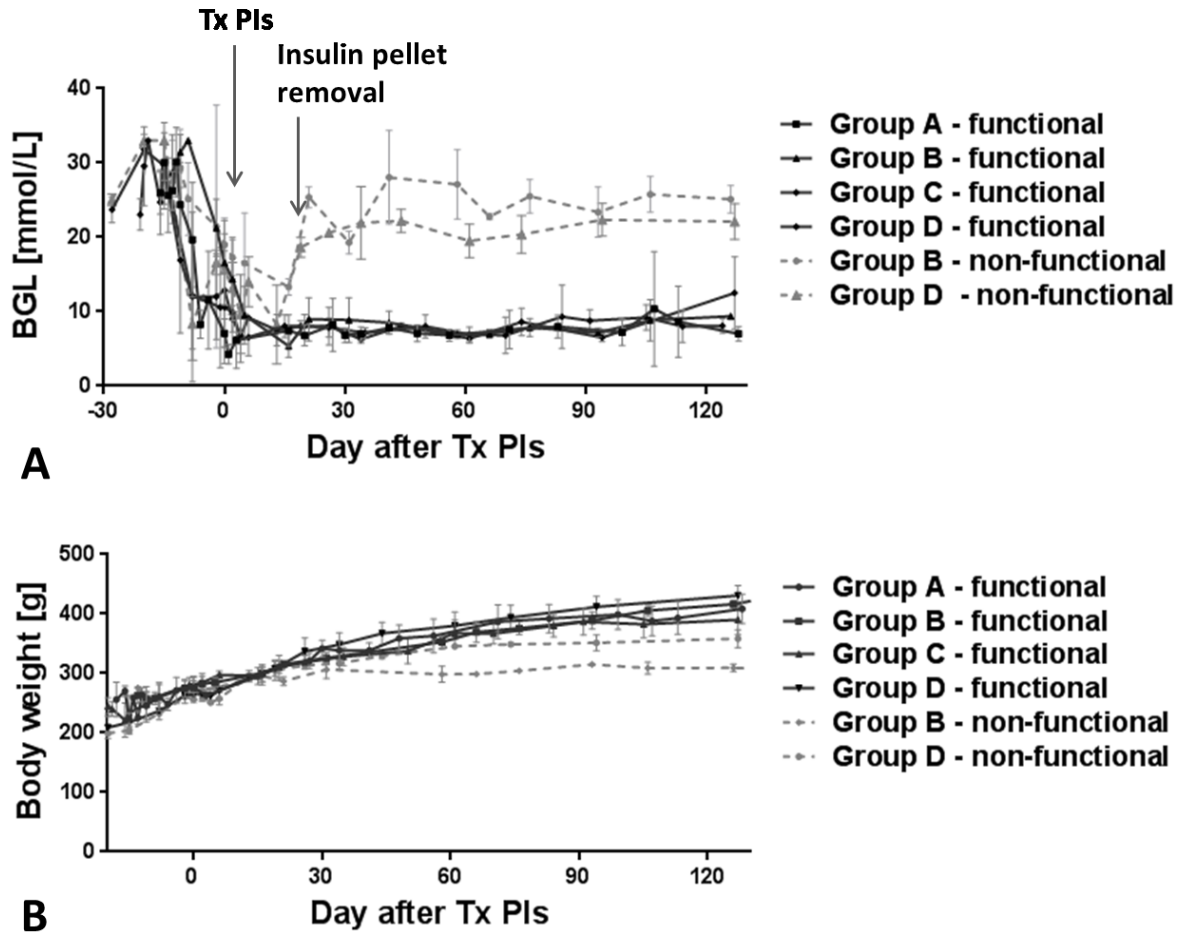

Fig. 4.13. Glycemia and body weight of animals during the examination. Blood glucose level (BLG) was normalized in groups A-D with functional PIs, and increased in groups B and D with non-functional PIs after pellet removal (A). The arrows show the day of pancreatic islet transplantation (Tx PIs) and the day of insulin pellet removal. Body weight of animals with functional and non-functional grafts (B). Animals with non-functional grafts are represented by a dotted line (Gálisová, Fábryová, Sticová, et al. 2017).

MR imaging

T_2-weighted MR images showed that the connective tissue grew through the scaffolds within the first two weeks. No visible anatomical differences between the scaffolds were found among the groups (Fig. 4.14).

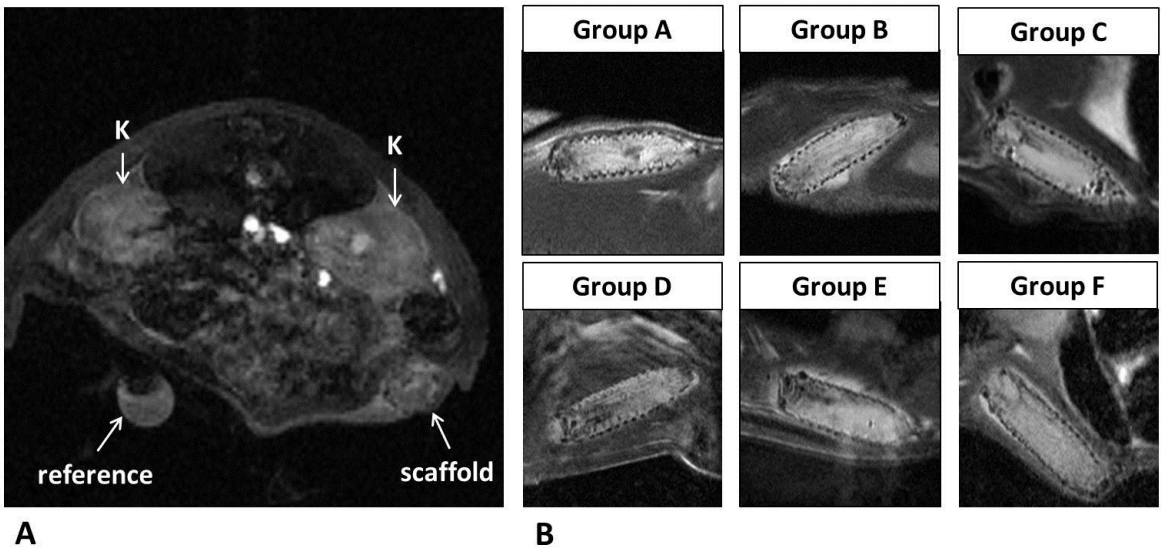

Fig. 4.14. Representative MR images of scaffolds. Representative DCE MR image of an animal with an implanted scaffold with MSCs and PIs (A) after contrast agent administration. The arrows indicate the kidneys (K), the scaffold and a reference tube. Representative T_2-weighted anatomical MR images of the scaffolds of different groups on day 7 after scaffold implantation (B) (Gálisová, Fábryová, Sticová, et al. 2017).

Dynamic MR measurements revealed a peak in the AUC three days after PIs transplantation in all groups, after which AUC values continuously declined until day 60.

Comparison of experimental groups to controls: Higher AUCs were observed in the scaffolds with the transplanted MSCs and/or PIs compared to the control scaffolds without any transplanted cells (paired t-test; $p < 0.001$ in groups A and B and $p < 0.01$ in groups C and D) (Fig. 4.15 A, B). Specifically, the difference between group B and controls (group E) was significant on all days following PIs transplantation, while the difference between groups A and E was significant on day 7 and 35 (Fig. 4.15 A) (unpaired t-test; $p < 0.05$). There was a significant difference between groups C and F on day 7 after PIs transplantation and between groups D and F on day (-1) and 60 (Fig. 4.15 B) (unpaired t-test; $p < 0.05$).

Comparison between scaffolds with and without MSCs: A significantly higher AUC was found in scaffolds supported with MSCs in comparison to scaffolds without MSCs (paired t-test; $p < 0.001$ in groups A and B and $p < 0.01$ in groups C and D). Unpaired t-tests revealed significance between groups A and B on day 3 (Fig. 4.15 A) and between groups C and D one day before PIs transplantation (Fig. 4.15 B) (unpaired t-test; $p < 0.05$).

Comparison between groups with transplanted PIs on day 4 and day 7: Scaffolds with PIs transplanted without MSCs on days 4 and day 7 after rod removal showed similar AUC

values (Fig. 4.15 C). Paired statistical analysis confirmed higher AUCs in the scaffolds with PIs and MSCs transplanted on day 4 after rod removal (paired t-test; p = 0.02). Unpaired statistical analysis revealed significant differences in AUC values on days 7, 10 and 35 (Fig. 4.15 D).

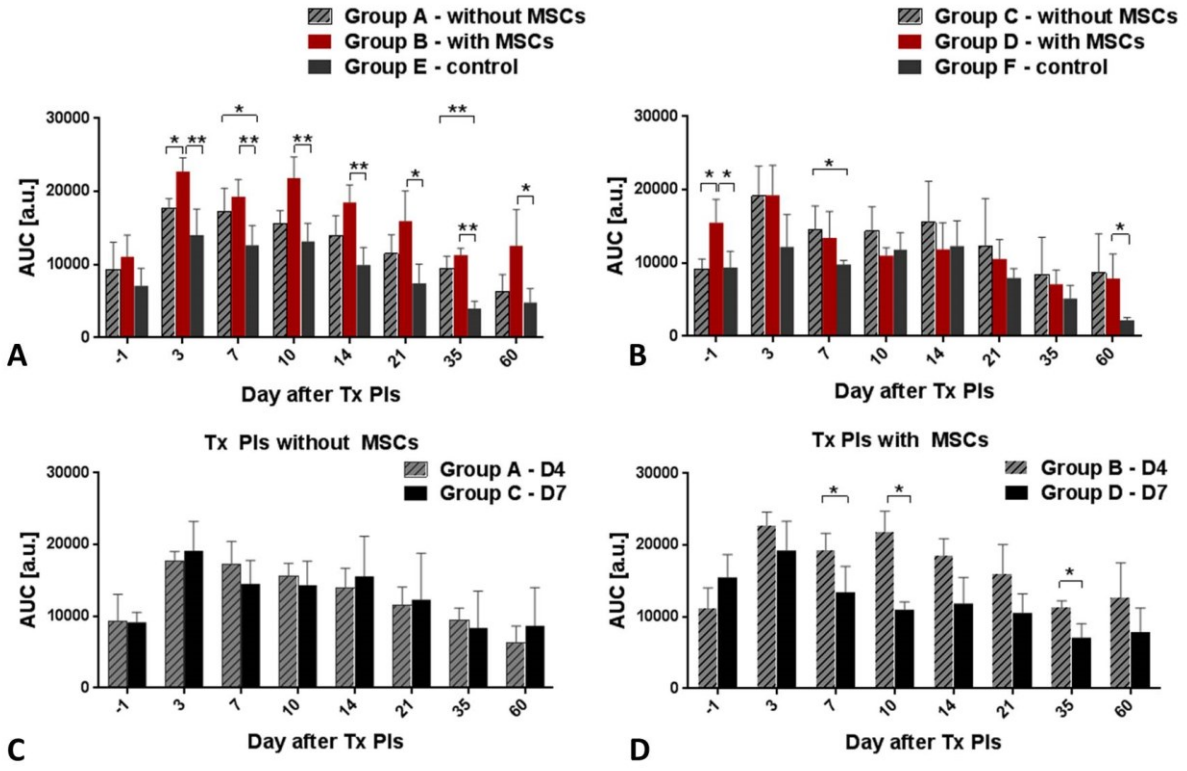

Fig. 4.15. DCE MR analysis related to vascularization. Differences in AUC between scaffolds with and without MSCs and controls in animal groups with pancreatic islets transplanted on days 4 (A) and 7 (B) after rod removal. Comparison of pancreatic islet transplantation on days 4 and 7 after rod removal according to AUC values in scaffolds without (C) and with MSCs (D). * $p < 0.05$, ** $p < 0.01$, *** $p < 0.001$ (Gálisová, Fábryová, Sticová, et al. 2017).

Bioluminescence imaging

Optical imaging confirmed the presence of viable LUC+ PIs in the scaffolds for the duration of the whole examination, whereas no bioluminescence signal was detected in the control groups. Optical signals originating from the viable PIs reached their maximum within the first post-transplant week in all experimental groups (day 5 or day 7) and, after partially decreasing, remained stable for 120 days. In the group C, the maximum bioluminescence signal (day 5) significantly differs from the signal measured on the last examination day (day 120) ($p < 0.05$). No significant difference was found between the maximum and the last measured signal in the groups A, B and D.

Pancreatic islets transplanted on day 4 after rod removal showed higher optical signals regardless of MSC presence compared to transplantation on day 7 after rod removal (Fig. 4.16). There was a significant difference in optical signals between groups A and C on days 35 and 120 (Fig. 4.16 C) and between groups B and D on days 10 and 35 (Fig. 4.16 D). Paired t-test analysis confirmed higher bioluminescence originating from PIs transplanted on day 4 compared to day 7 after rod removal ($p < 0.0001$). There was no significant difference between the groups (with or without MSCs) transplanted at the same time point ($p > 0.05$ for all groups).

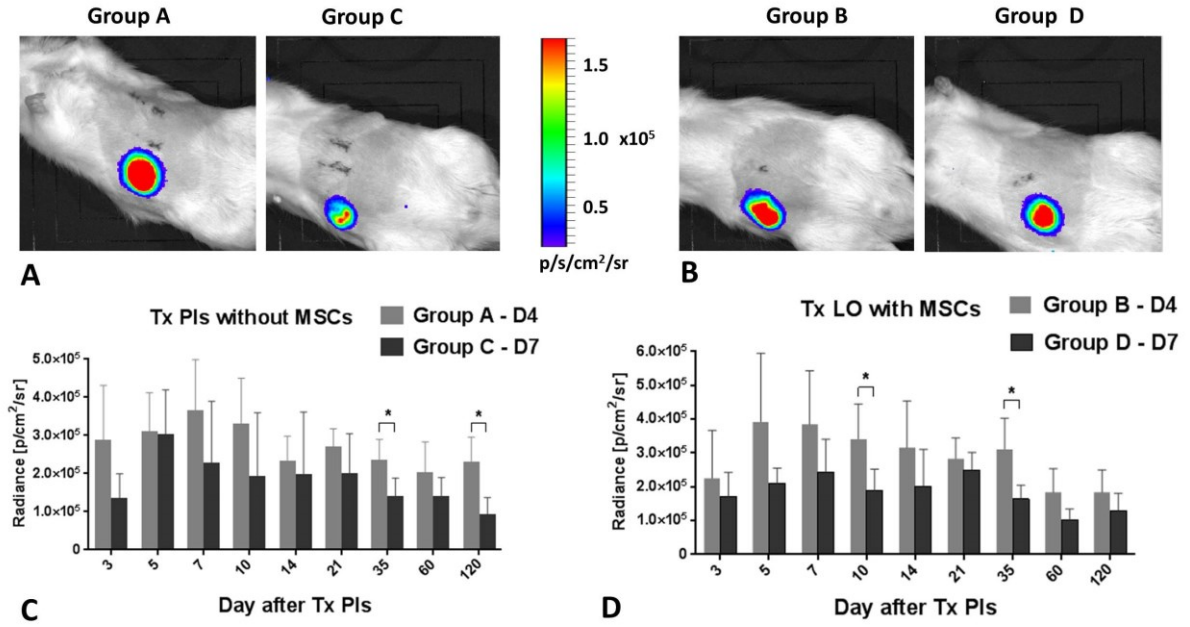

Fig. 4.16. ***In vivo*** **bioluminescence imaging.** Representative bioluminescence images of pancreatic islets transplanted into scaffolds without (A) and with MSCs (B). Images show the scaffolds on day 7 after PIs transplantation. Differences between optical signals originating from pancreatic islets transplanted on day 4 and day 7 after rod removal without (C) and with MSC support (D). D4 and D7 refer to the day after rod removal. *$p < 0.05$ (Gálisová, Fábryová, Sticová, et al. 2017).

Histology

Histological analysis of the specimens stained with hematoxylin/eosin demonstrated the presence of viable islets in the central parts of all scaffolds (Fig. 4.17 left row). Insulin deposits were found in all scaffolds with transplanted PIs (Fig. 4.17, middle row). The microarchitecture of the islets was distorted by mild interstitial fibrosis with minimal inflammatory changes. Neovascularization and fibrosis with hemosiderin deposits were also found in close proximity to the transplanted islets. Immunohistochemical staining with

the anti-CD31 antibody showed higher microvascular density within the devices with transplanted MSCs (Fig. 4.17 right row).

Quantitative analysis showed that the highest MVD was in the experimental scaffolds with PIs transplanted on day 4 after transplantation of MSCs (Group B). Representative images of CD31 stained microvascular structures in the scaffolds are shown in Fig. 4.2.18. The mean microvessel count per ×400 field was 9.4 in group A, 17.7 in group B, 11 in group C and 12.3 in group D. The results of DCE MR examination (AUC) strongly correlated with the results of MVD analysis ($R^2 = 0.99$).

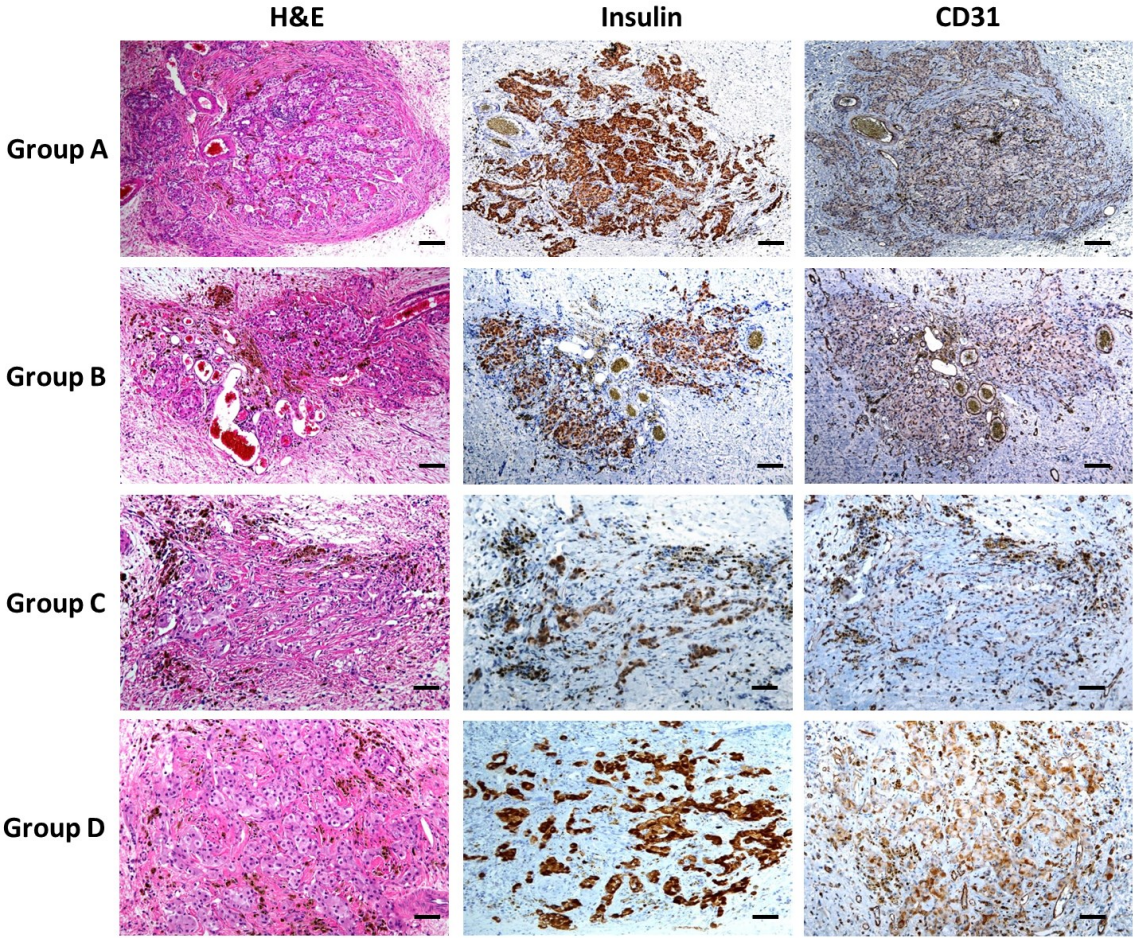

Fig. 4.17. Histology of the grafts. Representative images of transplanted pancreatic islets in scaffolds stained with hematoxylin/eosin (H&E) (left row) and immunohistochemically with primary antibodies anti-insulin (middle row) and CD31 (right row). Viable islets containing insulin positive cells were present in the scaffolds (H&E) in all groups A-D. Endothelial structures (CD31) were found in close proximity to the islets. Scale bars correspond to 100 µm (Gálisová, Fábryová, Sticová, et al. 2017).

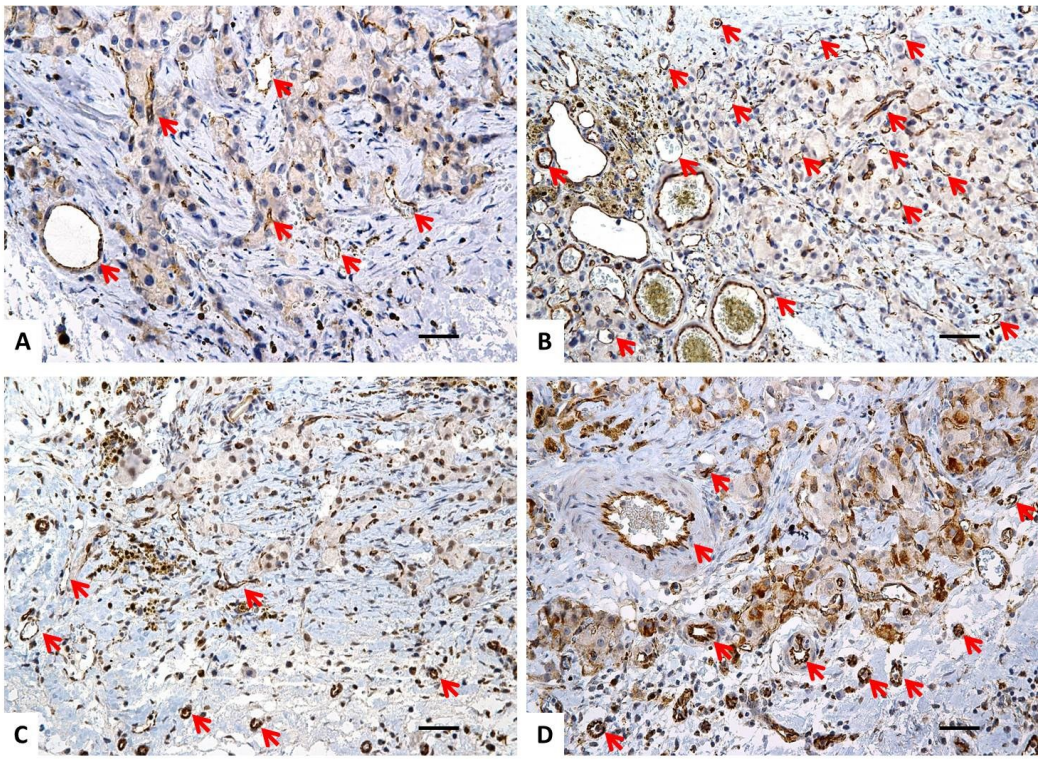

Fig. 4.18. Microvascular density analysis. Representative images of CD31 stained tissue sections from scaffolds. The arrows point to vascular structures that were counted for MVD analysis in group A (A), B (B), C (C) and D (D). Scale bars correspond to 50 μm (Gálisová, Fábryová, Sticová, et al. 2017).

4.2.3 Discussion

Subcutaneously implanted scaffolds represent a perspective transplantation site for PIs. They allow an easy access with the potential for biopsy/histology, device retrieval, imaging and possibility of direct drug delivery (e.g., immunosuppressives). Despite mentioned advantages, the subcutaneous space lacks sufficient vascularization that is necessary for highly oxygen demanding transplanted islets. Therefore, pre-vascularization of the scaffolds by mesenchymal stem cells and proper timing was studied using multimodal imaging.

The effect of MSCs on vascularization was assessed by DCE MR technique. The DCE MR signal reflects the rate of extravasation of a contrast agent into the tissue. It can be quantified by calculating the area under the curve (AUC); its value is dependent on vascular permeability and perfusion, which are related to vascularization. Our results show that transplantation of MSCs into empty scaffolds enhances vascular permeability and perfusion

and improve local blood supply. It has been reported that MSCs secrete various pro-angiogenic substances, such as vascular endothelial growth factor (VEGF), platelet-derived growth factor and angiopoietin-2 (Kagiwada et al. 2008; Krock et al. 2011), and stimulate growth of the vascular network (Miranville et al. 2004; Cao et al. 2005; Minteer et al. 2013; Tang et al. 2004; Martens et al. 2006). The effect of MCSs on vascularization is based on enhancement of formation and stabilization of vascular tubes of endothelial cells (Pill et al. 2015). Improvement of vascularization induced by MSCs was reported in variety of animal studies (Miranville et al. 2004; Cao et al. 2005; Minteer et al. 2013; Tang et al. 2004; Martens et al. 2006). Expression of VEGF and angiogenesis is enhanced under hypoxic condition (Krock et al. 2011; Sunderkötter et al. 1994) as is the case of the empty scaffolds.

Our results show also that the scaffolds with transplanted MSCs and LUC+ PIs exhibited higher AUC values and were therefore more effective in forming the vascular network. It is worth noting that the difference between AUC values in the scaffolds with and without MSCs (containing LUC+ PIs) were significant only at some time points. This may have been caused by interanimal variability and the relatively low number of experimental animals. Also the amount of transplanted MSCs (10 million) could have only the modest effect on changes in vascularization. Nevertheless, it is important that the results obtained by DCE MR examination strongly correlated with the histological findings; both analyses confirmed higher concentration of vascular structures in the scaffolds containing MSCs.

Moreover, a positive impact of MSCs on islet function and survival has been reported after co-culture (Hematti et al. 2013; Johansson et al. 2008) or co-transplantation of PIs with MSCs (Sakata et al. 2011; Kerby et al. 2013; Figliuzzi et al. 2009) due to the suppression of inflammatory responses to transplantation itself and to allograft rejections (Ding et al. 2011; Longoni et al. 2010). Some authors have also reported a positive influence of trophic factors released by MSCs such as VEGF (Figliuzzi et al. 2009), ciliary neurotrophic factor (Rezende et al. 2007), Von Willebrand factor (Ito et al. 2010; Figliuzzi et al. 2009; Solari et al. 2009) and IL-6 (Park et al. 2010) on islet survival.

In our model, only viable islets produced a bioluminescence signal and therefore their viability can be assessed throughout the whole experiment. The results show that the bioluminescent signal originating from transplanted PIs was comparable in the scaffolds with and without MSCs, while the number of normoglycemic animals was even lower in the groups with MSCs. Therefore, we suggest that MSCs had only a negligible impact on syngenic graft survival in our model and addition of MSCs also lowers islet function.

The final aim was to identify the optimal timing for transplantation of PIs in scaffolds. Our experiments with LUC+ MSCs revealed that the best engraftment period for PIs is between 3 and 9 days after MSC transplantation (10 to 16 days after implantation of the scaffold) (Gálisová, Fábryová, Jirák, et al. 2017). Some other studies with rats (Kříž, Greg, et al. 2012; Pileggi et al. 2006) and mice (Pepper, Pawlick, et al. 2015; Smink et al. 2017) with transplant devices stated that 4 weeks is necessary for embedding the device by connective tissue, which should be free of inflammation and rich in new vessels (Pileggi et al. 2006; Kříž, Greg, et al. 2012; Smink et al. 2017). Also the first clinical islet transplantation into a pre-vascularized device was performed 1 – 4 months after device implantation (Gala-Lopez et al. 2016), although the graft functionality was not reached. Contrary to this, our results indicate that a shorter time period (4 or 7 days after rod removal / 11 or 14 days after scaffold implantation, respectively) is also suitable and that the tissue is well vascularized even after this shorter period. Transplantation of PIs on day 4 after rod removal and with the support of MSCs was found to be better than transplantation on day 7 due to better vascularization (assessed by DCE MRI and histological MVD analysis) and islet viability (assessed by bioluminescence). The islets transplanted on day 4 after rod removal produced a higher optical signal, which reflected either the higher amount of surviving PIs or better availability of a substrate for the bioluminescence reaction caused by higher blood supply. Nonetheless, bioluminescent signal of PIs transplanted on day 7 without MSCs significantly decreased between day 5 and the end of examination, which confirmed limited long-term survival of PIs under this transplantation condition. We hypothesize that on day 4 after rod removal, a layer of newly formed granulation tissue in the scaffolds created a matrix suitable for vessel growth and oxygen penetration. The tissue could have become denser over a longer period (7 days), restricting vessel and oxygen availability.

In a novel site for PIs transplantation, consisting of a temporarily implanted catheter, an initial foreign-body response manifested by macrophage infiltration and neovascularization was reported to be favorable for islet survival and function (Pepper, Gala-Lopez, et al. 2015). We concede that a similar process could have also manifested in our model; although we emphasize the importance of the use of a retrievable scaffold for possible removal in case of complications such as rejection or inflammation. It should be noted that the devices were removed after certain period due to bacterial infection in a clinical study (Gala-Lopez et al. 2016).

The effect of MSCs on islet engraftment was not prominent; the grafts were also functional and well-vascularized without the use of MSCs, which points to the strong

influence of proper timing on islet engraftment. It is also worth noting that the transplanted mass was suboptimal and that the number of transplanted islets was lower compared to other scaffold models (Pepper, Pawlick, et al. 2015; Pileggi et al. 2006), which is an important parameter for clinical application due to lack of donors.

This study shows that islets transplanted on day 4 after rod removal reverted diabetes in more than 80% of experimental animals and normoglycemia was maintained until graftectomy (4 months). These findings confirm the efficiency of the model presented here for type 1 diabetes treatment. Moreover, viable grafts and insulin deposits were confirmed by histology, which verified results obtained by other methods. The tested scaffolds were made from a clinically approved material, and easily attainable adipose-derived MSCs were used, all of which enables easy translation into clinical practice.

4.2.4 Summary – bioluminescent pancreatic islets

- Bioluminescence is capable to monitor viability of transplanted cells/islets
- Artificial scaffolds represent a suitable extrahepatic site for PIs transplantation, which was confirmed by long-term reversal of diabetes, histology and imaging methods even using a suboptimal islet mass
- Addition of mesenchymal stem cells improved vascularization in scaffolds, although hindered islet engraftment and function
- The optimal time for transplantation of PIs into the scaffolds was found to be day 4 after rod removal (rather than day 7) in terms of better vascularization and islet viability
- The optimized protocol holds a potential for clinical applications

4.3 Pancreatic islets labeled with multimodal nanoparticles for ^{19}F MR and optical imaging

In this chapter, we focus on optimization of protocol for labeling of PIs by multimodal nanoparticles (NPs) trackable by both ^{19}F MR and optical imaging. Three labeling routes – endocytosis, microporation, and pre-microporation were optimized and compared. Labeled islets were transplanted at extrahepatic transplantation site and tracked by multimodal imaging *in vivo*.

The study was divided into four parts:

1) Estimation of imaging sensitivity of the multimodal nanoparticles
2) Comparison of islet labeling by standard microporation and pre-microporation
3) Optimization of islet labeling using endocytosis
4) *In vivo* multimodal imaging (^{19}F MRI, fluorescence and bioluminescence) of transplanted islets in rats

The results of the experiments focused on optimization of the procedures for labeling of PIs by the multimodal nanoparticles and longitudinal *in vivo* tracking of labeled PIs using trimodal imaging (^{19}F MRI, fluorescence and bioluminescence) have been summarized in two publications:

- Herynek V, Gálisová A, Srinivas M, van Dinther EAW, Kosinová L, Ruzicka J, Jirátová M, Kriz J, Jirák D. Pre-Microporation Improves Outcome of Pancreatic Islet Labeling for Optical and ^{19}F MR Imaging. Biological Procedures 2017 (IF 2)
- Gálisová A, Herynek V, Srinivas M, Swider E, Sticová E, Pátiková A, Kosinová L, Kriz J, Hájek M, Jirák D. A novel trimodal platform for tracking of transplanted pancreatic islets: ^{19}F MR, fluorescence and bioluminescence imaging. Submitted to Molecular Imaging and Biology (IF 3.5).

4.3.1 Materials and Methods

Preparation and characterization of the multimodal nanoparticles

Poly(lactic-co-glycolic acid) nanoparticles (PLGA-NPs) containing a near-infrared fluorescent dye indocyanine green (ICG) and perfluoro-15-crown-5-ether (PFCE) were prepared at the collaborating Multiscale imaging lab of Radboud University in Nijmegen (Netherlands) by solvent evaporation-extraction method as it was described before (Srinivas et al., 2010).

Briefly, 100 mg of PLGA was dissolved in 3 mL Dichloromethane. 900 µL of PFCE and 1 mg of ICG was added to the organic phase. Next, the organic phase was added to the aqueous phase containing a surfactant under ultrasonication. To formulate positively charged particles, the protocol was slightly modified by adding 0.4 g of diethylaminoethyl-dextran (Sigma-Aldrich, Germany) to the aqueous phase. The size of the nanoparticles – measured using dynamic light scattering (DLS; Zetasizer Nano – Malvern Instruments Ltd, UK) – was 180 nm with a polydispersity index of 0.1. The PFCE content – measured on a Bruker Avance III 400 MHz NMR (Bruker, Germany) – was $1.8\text{-}6.0\times10^{18}$ fluorine atoms per mg of the lyophilized sample. The nanoparticles (in the form of a freeze-dried powder) were resuspended in distilled water or PBS at various concentrations (0.04 - 10 mg/mL) and placed into the tubes for assessment of imaging sensitivity.

Isolation, labeling and preparation of islets for imaging

Pancreatic islets were isolated from Brown-Norway rats and the transgenic Lewis rats with ubiquital expression of a gene for the luciferase enzyme (National BioResource Project – Rat, Kyoto, Japan). Luciferase negative (LUC-) were used as donors for *in vitro* examination of islets and luciferase-positive (LUC+) animals were used as donors of PIs for transplantation. Isolation of PIs was performed according to a standard protocol described in the section 4.1.1 (p. 47). After isolation, islets were incubated for 24 hours (37 °C, 5% CO_2 atmosphere) in a culture medium containing 84% CMRL-1066 medium, 10% FBS, 5% HEPES, 0.5% penicillin/streptomycin, and 0.5% glutaMAX (ThermoFisher Scientific, USA).

Labeling by endocytosis, microporation and pre-microporation was tested and compared. Viability of labeled islets was examined by using fluorescent dyes propidium

iodide and acridine orange as was described in the section 4.1.1 (p. 48). Insulin release potency of islets was assessed by the glucose stimulated insulin secretion test as was described in the section 4.1.1 (p. 48). Gain was calculated as percentage of harvested islets to all islets used for labeling. For *in vitro* imaging, islets were fixed with 4% formaldehyde and different numbers of islets were placed into the separate tubes. Islets were labeled by endocytosis for *in vivo* experiment due to the best labeling outcome (without formaldehyde fixation).

- *Microporation – standard procedure*

Poration was performed using the electroporation device Neon Transfection System (ThermoFischer Scientific, USA). 200 or 250 pancreatic islets were resuspended in the buffer R (ThermoFischer Scientific, USA) together with the nanoparticles (23 mg of PLGA-NPs per 1 mL of suspension) in the final volume of 110 μL. The suspension was aspired by the pipette with a 100-μL pipette tip and placed into the container with the electrolytic buffer E2 according to the manufacturer's instructions. Then, high voltage electric pulses were applied. Islet suspension with nanoparticles was placed into a 96-well plate and kept on ice for 10 minutes immediately after poration. Then the samples were transferred to wells containing 3 mL of medium without antibiotics for 24-hour incubation (37 °C, 5% CO_2) (Fig. 4.19). After labeling, the islets were collected, washed three times with PBS, counted and placed into 0.5 mL test tubes for imaging.

Different poration parameters were optimized – number of pulses (1, 2, 4), length of pulses (20 and 30 ms) and voltage (600 – 1500 V corresponding to electric field 20 – 50 kV/m).

- *„Pre-microporation" – modified protocol for microporation*

250 pancreatic islets were resuspended in 110 μL of the buffer R. The samples were aspired into the pipette tip and placed into the microporator container with the electrolytic buffer E2. Two 20 ms pulses were then applied with various voltage (500 – 1000 V, electric field 16.5 – 33 kV/m). After islets pre-poration, the samples were transferred into small wells (96-well plate) containing culture medium with suspended nanoparticles (final concentration of PLGA-NPs was 23 mg/mL). The islets were kept with concentrated nanoparticles on ice for 10 minutes, then the samples were placed into bigger wells (6-well plate) and incubated

for 24 hours (37 °C, 5% CO_2) (Fig. 4.19) in medium without antibiotics. A control sample was microporated using 600 V (two pusles, 20 ms) and incubated in culture medium without nanoparticles. After incubation, the islets were collected, washed three times with PBS, counted and placed into 0.5 mL test tubes for imaging.

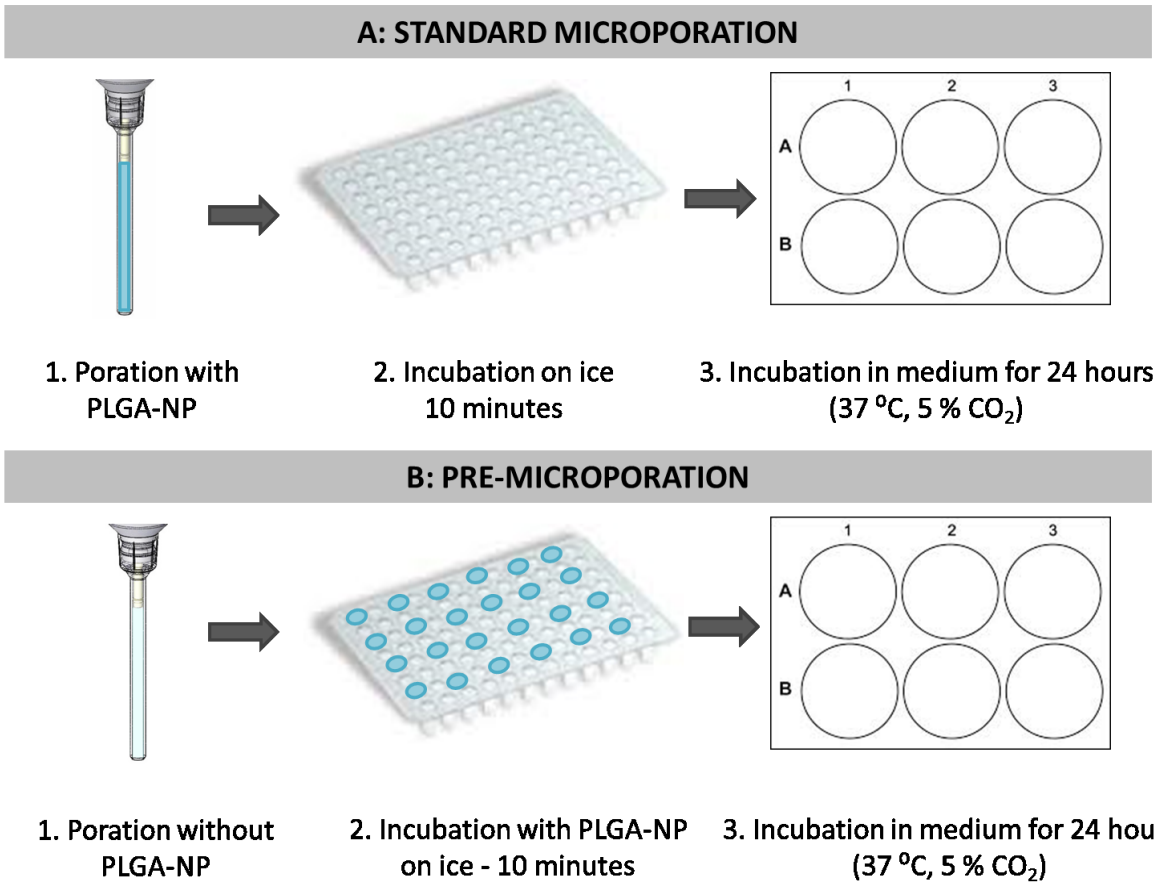

Fig. 4.19. Comparison of experimental design of microporation and pre-microporation procedures. According to the standard procedure, islets are porated in a capillary with a contrast agent (PLGA-NPs) and then incubated in a 96-well plate with pure medium. On the contrary, pre-microporation includes poration without PLGA-NPs and then 10 minute incubation on ice in a well containing medium with PLGA-NPs. After 10 minutes, labeled islets are transferred into a 6-well plate for 24-hour incubation in both cases.

- *Endocytosis*

Islets labeled by endocytosis served as a reference sample for comparison of a standard microporation procedure and pre-microporation. In this experiment, 250 isolated islets were incubated in a medium containing resuspended 23 mg/mL of

PLGA-NPs for 24 hours. The islets were collected, washed three times with PBS, counted and placed into 0.5 mL test tubes for imaging after labeling.

500 islets were incubated in a culture medium containing various concentrations of PLGA-NPs: 12 mg/mL, 17 mg/mL and 23 mg/mL to optimize labeling by endocytosis. The islets were divided into three amounts (50, 100 and 300 islets) and placed into 0.5 mL test tubes prior imaging after 24-hour incubation.

Five hundred islets were labeled with 23 mg/mL of PLGA-NPs and different numbers (10, 30, 50, 100 and 300) of islets were placed into a 6-well plate with 2 mL of a culture medium to estimate imaging sensitivity. The islets were then visualized by fluorescence and bioluminescence imaging (after addition of 0.15 mg/mL D-luciferin).

For *in vivo* experiment, islets were incubated in a 5-mL flask containing 17 mg/mL or 23 mg/mL of PLGA-NPs (1000 islets in each flask). The islets were collected and washed three times with PBS after 24-hour incubation. Control islets were incubated in a culture medium without nanoparticles. The labeled and control islets were counted, hand-picked and placed into a plastic tube prior transplantation.

Confocal microscopy

Confocal microscopy was used for confirmation of intracellular localization of the labels inside the islets. The islets were prepared by overnight fixation by 4% formaldehyde. The islets were then washed by PBS and spun for 1 min at 1300 rpm. 2% agarose was added to the pellets and the mixture was immediately centrifuged for 1 min at 1800 rpm. After solidification of agarose, the pellets were transferred into 30% sucrose solution and incubated at 4 °C overnight. After incubation, the islets were placed in plastic containers and overlayered by Tissue-Tek (Sakura, Netherlands). The samples were stained with diaminophenylindole (DAPI) and mounted with vectashield (Vector H-1000, USA) on a glass slide. The samples were visualized by the confocal microscope Olympus FV1200MPE (Olympus Life Science, Japan). Green background was imaged by an Argon laser at 488 nm, DAPI signal by an EPI lamp at 405 nm and ICG signal by a LD599 laser using excitation at 647 nm. The images were taken on 20x (air) and 60x (oil immersion) objective.

Animal model of extrahepatic transplantation of pancreatic islet

Male LUC- Lewis rats (Velaz, Czech Republic) weighing 350 – 450 g were chosen as the recipients of the pancreatic islets. A surgical non-fluorescent mesh was shaped into the scaffolds and implanted as described in the Chapter 4.2.1 (p. 66). Two scaffolds were implanted in each animal. Three days after rod removal, pancreatic islets were transplanted into the exposed cavities using a manual injector supplemented with a plastic tube in order to ensure the slow controlled injection of a large volume of islets (avoiding syringe obstruction). The scaffolds were closed using small plugs after transplantation and the incisions were tightly closed using 5-0 sutures. Experimental animals received labeled LUC+ islets (3000 and 1000 in each scaffold) and a control animal received unlabeled LUC+ islets (3000 and 1000). Islets were labeled with 17 mg/mL and 23 mg/mL of PLGA-NPs in this experiment.

MRI and optical imaging

Prior imaging, the rats were anesthetized by intramuscular anesthesia (ketamine 36 mg/kg and dexmedetomidine 0.08 mg/kg). All optical images (bioluminescence and fluorescence) were acquired on an IVIS Lumina XR imager and processed using Living Image software (Perkin Elmer, USA). Fluorescence images were measured using excitation at 745 nm and emission at 810 - 875 nm. Bioluminescence images were acquired with an open emission filter without using the excitation light. Fluorescence signal was expressed in average radiance efficiency [photons/sec/cm^2/sr]/(μW/cm^2); bioluminescence signal in average radiance (photons/sec/cm^2/sr).

MR imaging was performed on a 4.7 T MR scanner (Bruker BioSpin, Germany) using a home-made dual ^{1}H/^{19}F surface single loop coil. For anatomical localization of the samples/animals, proton T_2-weighted images were acquired using a turbo spin echo sequence: TR = 3000 ms, TE = 12 ms, effective echo time TE_{eff} = 36 ms, turbo factor 8, spatial resolution 0.19 x 0.19 x 2 mm^3, NA = 4 and scan time of 1 minute. After ^{1}H MR acquisition, the coil was tuned to ^{19}F frequency and transmitter power was set up using a simple single pulse FID sequence.

For visualization of pure agent solutions and the phantoms containing labeled islets, ^{19}F MR images were acquired using a turbo spin echo sequence with parameters TR = 1000 ms, TE = 3.2 ms, TE_{eff} = 42.2 ms, turbo factor 32. For assessment of sensitivity

of visualization of pure agents, ^{19}F MR images were acquired using different acquisition times (4 min – 3 hours) and various slice thickness (2.2 – 10 mm). For assessment of detection threshold of labeled islets, the phantoms were measured within 1 hour 8 minutes (NA = 4096) with slice thickness of 10 mm.

In vivo imaging of animals with transplanted islets was trimodal: bioluminescence, fluorescence and ^{19}F MRI. Fluorescence imaging was performed using exposure time of 60 s (aperture f_{STOP} = 4). Bioluminescence images were acquired before and after intravenous administration of D-Luciferin (70 mg/kg) using 60 s exposure time. MR imaging was performed after optical imaging. Axial and coronal T_2-weighted ^{1}H MR images were acquired for co-registration. Axial ^{19}F MR images were acquired using a turbo spin echo sequence with the following parameters: TR = 1500 ms, TE = 3.2 ms, TE_{eff} = 42.2 ms, turbo factor 32, slice thickness 20 mm, spatial resolution 1.8 × 1.0 × 20 mm^3. One ^{19}F MR image was acquired with a reference tube within 19 minutes (NA = 768), then the reference was removed and another ^{19}F MR image was acquired within 51 minutes (NA = 2048). The ^{19}F MR images were interpolated from the acquisition matrix 32 × 32 to 256 × 256, converted to false colors and co-registered with anatomical images using ImageJ (National Institute of Health, USA).

Signal intensity from ^{19}F MR and fluorescence images was evaluated from manually outlined ROIs around each tube or artificial scaffold and SNR values were calculated. Fluorine content in labeled islets was calculated from the in vitro ^{19}F MR images according to the formula 3.10 (p. 36). Absolute quantification of transplanted islets was performed according to the formula 3.11 (p. 37).

Histological analysis

Two weeks after islet transplantation, the scaffolds were removed, fixed in 10% neutral buffered formalin and embedded in paraffin blocks. Four-µm-thick paraffin sections were cut and routinely stained with hematoxylin and eosin (H&E) and Verhoeff-Van Gieson elastin stain. Immunohistochemical detection of insulin (mouse monoclonal, MU029-UC, Biogenex, USA) and Luciferase (mouse monoclonal, Luci 21 1-107, Novus Biologicals, USA) was performed on 4-µm-thick paraffin sections. The primary anti-insulin antibody was detected by the Simple Stain MAX PO (MULTI) Universal Immuno-peroxidase Polymer anti-mouse, anti-rabbit Histofine (Nichirei Biosciences, Japan). The Histofine Simple Stain Rat MAX PO (Nichirei, Japan) was used for detection of Luciferase. Finally, visualization was performed with Dako Liquid DAB+ Substrate-Chromogen System (Dako,

Denmark) and counterstaining with Harris's hematoxylin. The slides were viewed using a standard light microscopy (Olympus BX41).

Statistical analysis

Statistical analysis was conducted using GraphPad Prism 6.02 (GraphPad Software Inc., USA). Values in the graphs are reported as mean ± standard deviation. Coefficients of regression (R^2) are presented based on the results of linear regression analysis.

4.3.2 Results

1) Sensitivity of visualization of the multimodal nanoparticles by ^{19}F MR and fluorescence imaging

Both fluorescence and ^{19}F MRI signal originating from tubes with PLGA-NPs was proportional to PLGA-NPs concentration; however optical signal was quenched at higher concentrations (higher content of the ICG dye) (Fig. 4.20). The curve shape of fluorescence quenching of our probe corresponds to the published data (Yuan et al. 2004).

The minimal concentration of PLGA-NPs detectable by ^{19}F MRI (above signal of a control water sample with SNR = 2.5) is 0.3 mg/mL (from 10 mm slice and within 30 min, SNR = 4.3) (Fig. 4.21). Fluorescence imaging was more sensitive for visualization of PLGA-NP than ^{19}F MRI. To visualize 0.3 mg/mL of PLGA-NPs in a solution, 2 seconds of acquisition were needed (to detect 1×10^7 photons/s/cm^2/sr) in the case of fluorescence imaging, whereas ^{19}F MRI required at least 30 minutes. Because of low sensitivity of ^{19}F MRI, the minimal thickness of a MR slice for current experimental set-up is 10 mm for visualization of 0.3 mg/mL of PLGA-NPs (Fig. 4.21B). Concentration above 1.2 mg/mL of PLGA-NPs was necessary for sufficient MR detection of PLGA-NPs within shorter acquisition time (4 - 17 min).

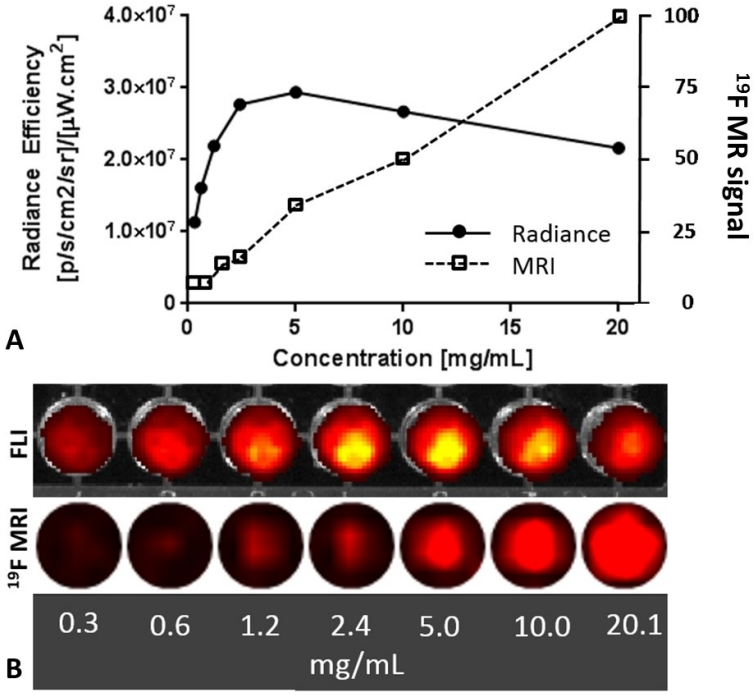

Fig. 4.20. Fluorescence and ^{19}F MR signal of resuspended PLGA-nanoparticles. Dependence of ^{19}F MR (dotted line) and fluorescence signal (solid line) on PLGA-NPs concentration (A, B). Fluorescence signal is quenched at higher PLGA-NPs concentrations, while the ^{19}F MR signal linearly increased (A). Representative ^{19}F MR and fluorescence images of the tubes with resuspended nanoparticles at various concentrations are shown (B) (Herynek et al. 2017).

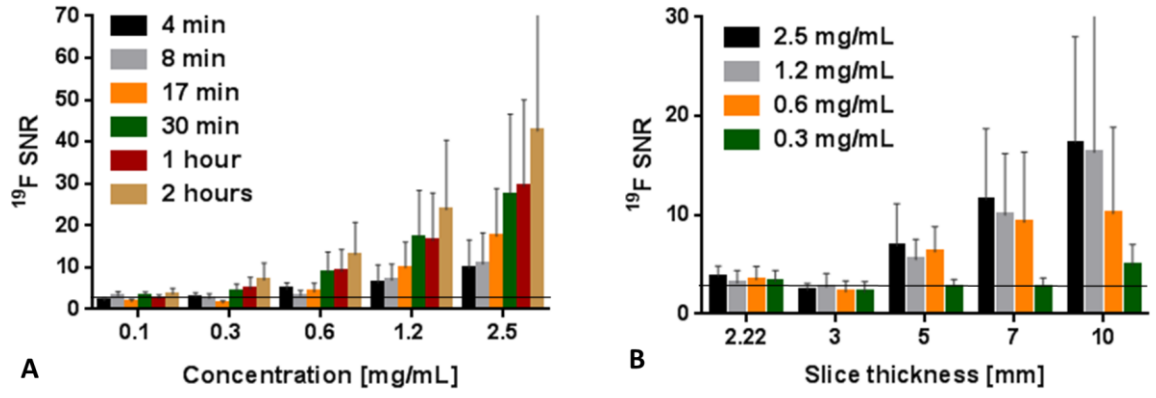

Fig. 4.21. Sensitivity of visualization of PLGA-nanoparticles. ^{19}F MR examination of detection sensitivity of PLGA-NPs. Various concentrations (A) and slice thickness (B) were tested. The line represents a detection threshold – the signal originating from a control water reference.

2) Comparison of a standard microporation procedure and pre-microporation

A number of pulses (1, 2 and 4) used for microporation were optimized at first. Viability and gain were similar when one or two pulses were used; however the use of 4 pulses led to significant decrease of both viability and gain of harvested islets (Mann-Whitney U test, $p<0.05$) (Fig. 4.22 B). Islets labeled by microporation using two pulses exploited the highest labeling efficiency assessed by fluorescence imaging; ^{19}F MR signal of islets labeled by using one or four pulses was lower compared to two pulses (Fig. 4.22 C). Therefore, two 20-ms pulses for microporation and 10 min incubation on ice after microporation was implemented in further experiments.

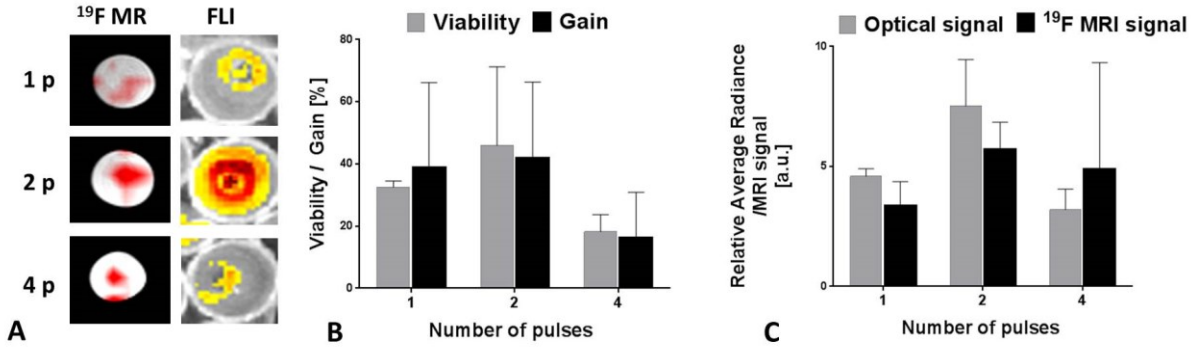

Fig. 4.22. Optimization of microporation parameters. ^{19}F MR and fluorescence images of islets labeled by microporation using 1, 2 or 4 pulses (A). Comparison of calculated viability/gain (B) and ^{19}F MR and fluorescent signal (C) of islets labeled by using different number of microporation pulses.

Microporation and pre-microporation were compared in terms of gain and viability of labeled islets. The results showed that gain of harvested islets was markedly higher in case of pre-microporation (Figure 4.23). The use of the standard microporation procedure led to low gain of harvested islets (below 50%) in comparison to pre-microporation, and significantly lower compared to endocytosis (U test, $p< 0.05$, marked by "x" in Fig 4.23 A). Pre-microporation reached comparable gain to endocytosis at lower voltages; only the use of high voltage (1000 V) caused significant decrease in gain (U test, $P < 0.5$, marked by "×" in Fig. 23 B).

Viability of islets labeled by both microporation procedures was decreased at higher voltage (Fig. 4.23 A, B). Islets labeled by microporation at lower voltage reached comparable viability to endocytosis (around 90%). The use of voltage above 900 V (standard procedure) and 800 V (pre-microporation) affected islet viability significantly compared to endocytosis (U test, $p<0.05$, marked by "*" in Fig. 4.23 A, B). Viability and gain of the control sample was above 98%.

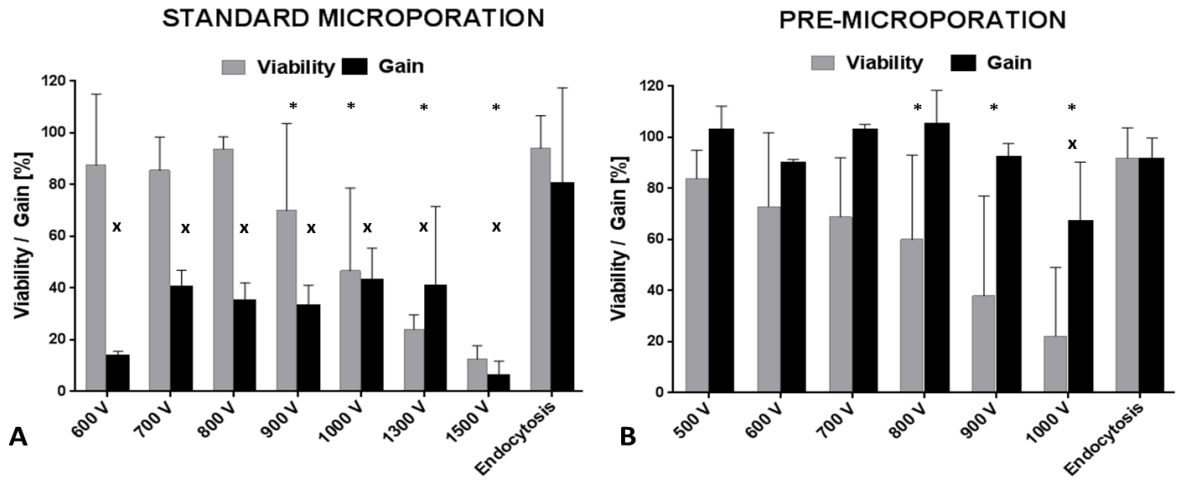

Fig. 4.23. Comparison of viability and percentage of harvested islets (gain). Viability and gain of islets labeled by a standard microporation procedure (A) and pre-microporation (B) compared to endocytosis. 100% gain = number of islets before labeling (Herynek et al. 2017).

Islets labeling by both microporation procedures and by endocytosis was sufficient for detection by ^{19}F MRI and fluorescence imaging. Representative ^{19}F MR, fluorescence and viability images (fluorescence images reflecting integrity of the cell membrane) of labeled islets are presented in Fig. 4.24. The control samples (islets microporated without PLGA-NPs, and islets incubated in medium without PLGA-NPs) provided negligible ^{19}F MR and fluorescence signals.

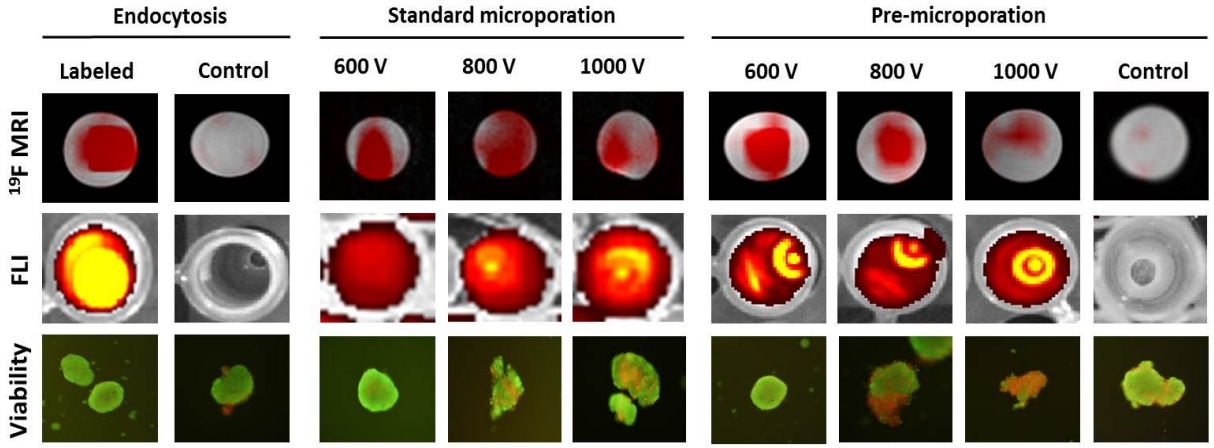

Fig. 4.24. Comparison of labeling procedures – imaging and viability. Representative ^{19}F MR, fluorescence (FLI) and viability images of the islets labeled by a standard microporation procedure and pre-microporation in comparison to endocytosis. The last row shows islets stained by propidium iodide and acridine orange (viable cells are green, dead cells are red) (Herynek et al. 2017).

Quantification of signals revealed that the labeling of islets by using lower voltage was advantageous by means of higher ^{19}F MR (Fig. 4.25 C, D) and optical signals (Fig. 4.25 A, B) obtained from the labeled islets. According to ^{19}F MR data, labeling efficiency of both microporation procedures was markedly lower compared to endocytosis; however signal from 250 microporated islets was still detectable within a 1-hour scan (Fig. 4.25 C, D). Interestingly, fluorescence imaging revealed higher signal from microporated islets (at lower voltage) compared to endocytosis (Fig. 4.25 A, B). This discrepancy can be explained by fluorescence quenching at higher ICG concentration inside islets in case of endocytosis.

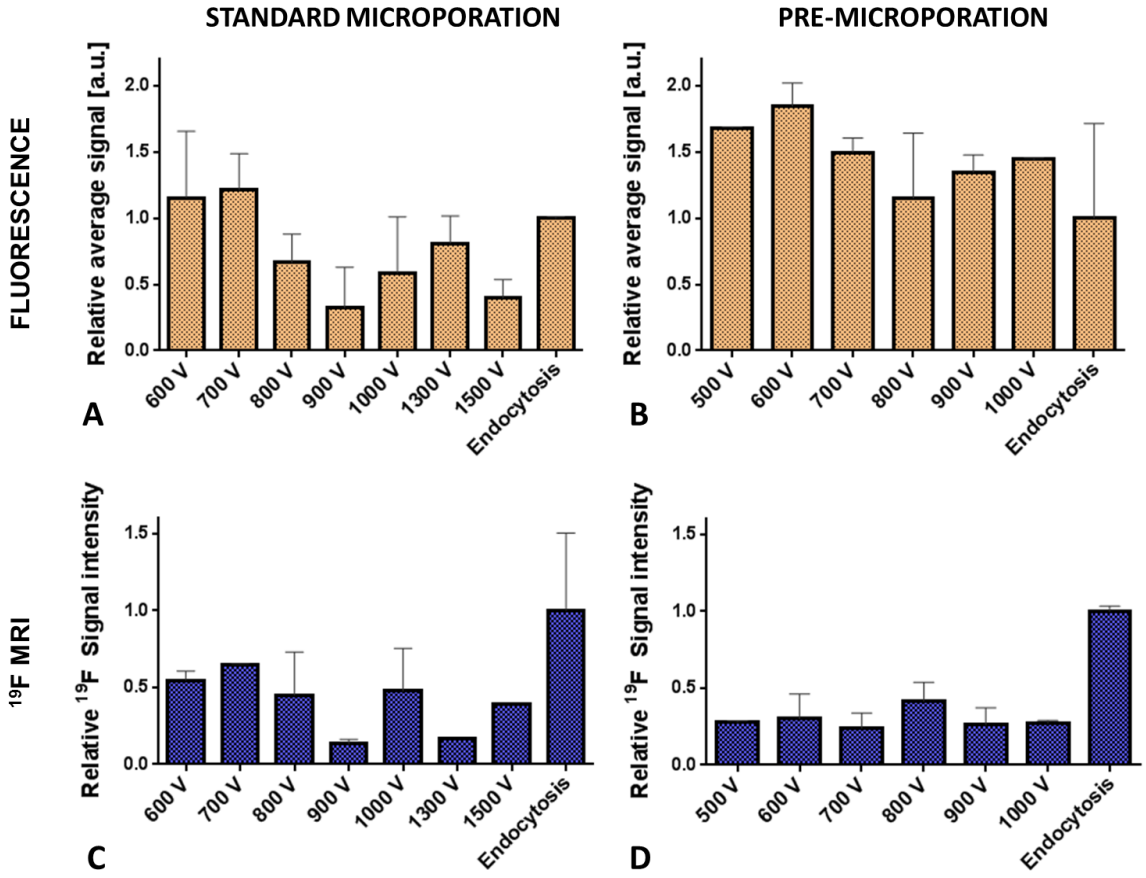

Fig. 4.25. Comparison of labeling procedures – quantification of imaging signals. Relative (normalized to endocytosis) fluorescence signal (upper row) and ^{19}F MR signal intensity (bottom row) of islets labeled by a standard microporation (A) and pre-microporation (B). Different voltage ranging from 600 V to 1500 V was tested.

The uptake of PLGA-NPs into pancreatic islets labeled by microporation and endocytosis was also confirmed by confocal microscopy. There was a higher fluorescence signal at the ICG frequency in the islets labeled by endocytosis compared to microporation (Fig. 4.26), which is in agreement with the ^{19}F MR results.

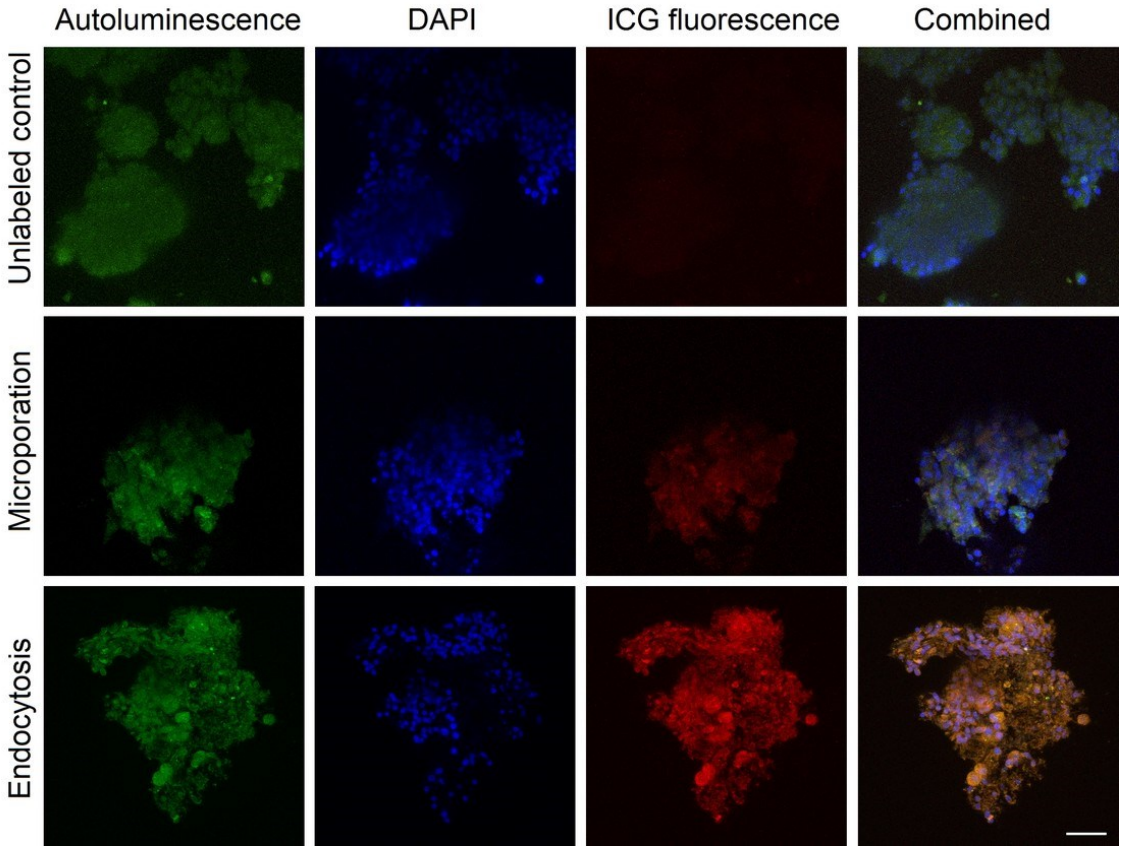

Fig. 4.26. Confocal microscopy of fixed islets. A control unlabeled pancreatic islets (upper row), islets labeled by microporation (600V, 2 pulses) (middle row) and endocytosis (bottom row) using the same concentration of PLGA-NPs. Artificial color represent autoluminescence (green), DAPI staining for nuclei (blue) and ICG signal corresponding to PLGA-NPs (red). Merged images of red, green and blue signals are shown on right. The scale bar represents 50 μm (Herynek et al. 2017).

In summary, the optimal protocol for islet labeling by microporation, which ensures high gain of harvested islets and viability of the islets as well as reasonably high labeling efficiency is as follows:

- pre-microporation without PLGA-NPs using two 20 ms pulses at 600 V,
- placing of microporated islets in the medium with suspended PLGA-NPs on ice for 10 minutes,
- transferring islets to a Petri dish containing the medium and 24-hour incubation at 37°C for recovery

3) Optimization of islet labeling using endocytosis

Viability and functionality of islets labeled with various concentration of PLGA-NPs using endocytosis was assessed. The results showed that labeling procedures based on endocytosis did not affect islet viability markedly; islets labeled by endocytosis with concentration 23 mg/mL of PLGA-NPs showed comparable viability to unlabeled ones (Fig. 4.27 A). Viability of the labeled islets was also confirmed by *in vitro* bioluminescence imaging, while labeled islets provided similar bioluminescence signal (300 PIs: 6.2×10^5 p/s/cm^2/sr) to unlabeled controls (300 PIs: 6.0×10^5 p/s/cm^2/sr).

Islet functionality after labeling was confirmed by measuring of the insulin release upon glucose stimulation. The glucose stimulation index above 2 confirmed good functionality of labeled islets (Fig. 4.27 B). Islets labeled with higher PLGA-NPs concentration (23 mg/mL of PLGA-NPs) had moderately lower stimulation indices (2.4±0.3) compared to the control sample (3.5±0.9).

In the case of LUC+ islets, *in vitro* bioluminescence imaging confirmed expression of luciferase and sufficient bioluminescence signal originating from both labeled and unlabeled islets (Fig. 4.27 C). Fluorescence imaging showed that unlabeled islets emit no fluorescence signal after excitation at 745 nm (Fig. 4.27 D). There was a linear relationship between the number of islets and their *in vitro* fluorescence and bioluminescence signal (both $R^2 = 0.99$) (Fig. 4.27 C, D).

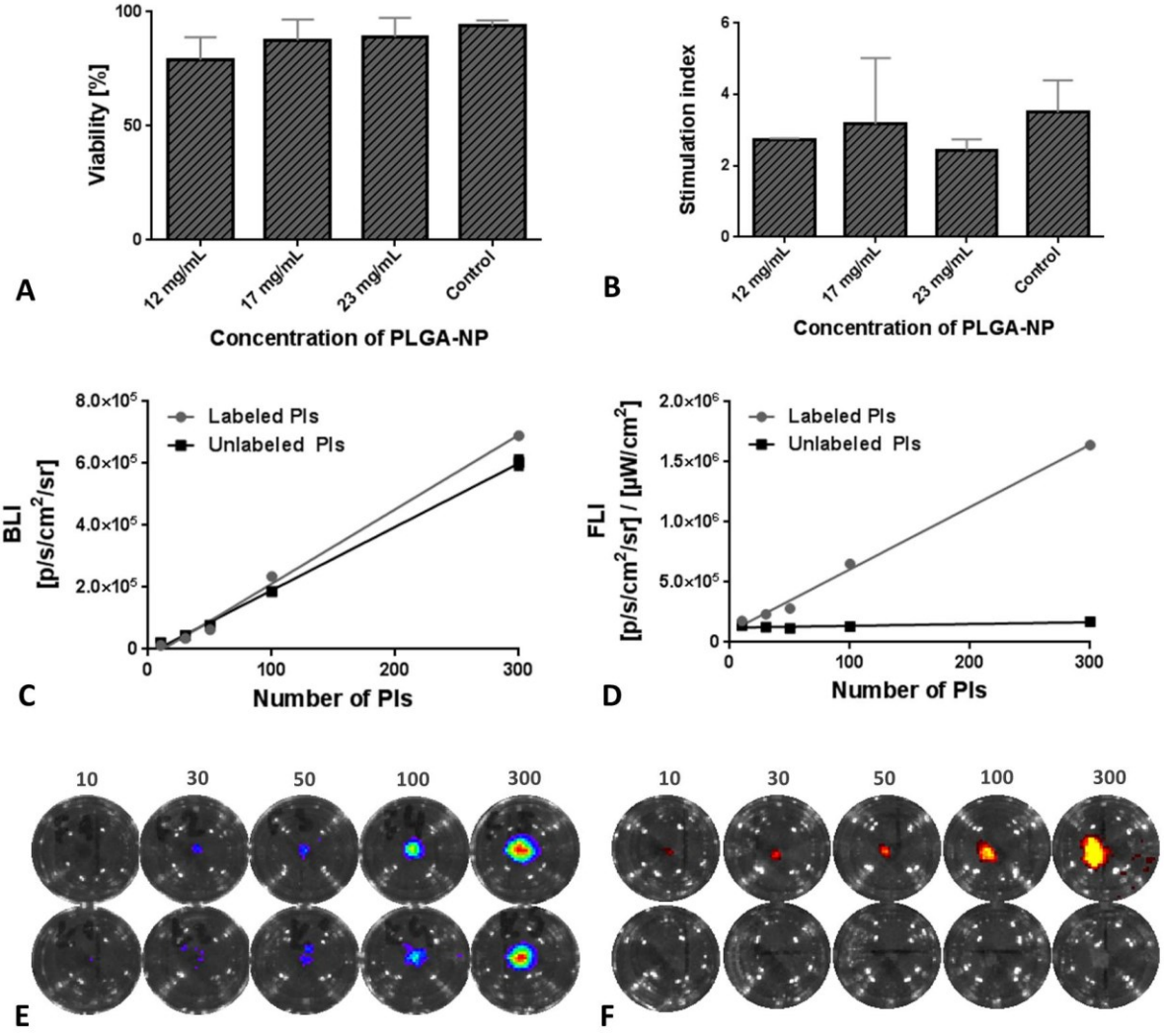

Fig. 4.27. *In vitro* characterization of pancreatic islets. Viability (A) and glucose stimulation indices (B) of islets after labeling with PLGA-NPs. Quantification of *in vitro* bioluminescence (C) and fluorescence (D) signal from labeled and unlabeled islets. Representative bioluminescence (E) and fluorescence (F) images of different numbers of labeled (upper row) and unlabeled (bottom row) islets.

As little as 50 islets were detected by ^{19}F MRI at an imaging time of 1 hour (Fig. 4.28 A, C). Highest ^{19}F MRI and fluorescence signal was originating from islets labeled by endocytosis using 17 mg/mL of PLGA-NPs for 24 hours (Fig. 4.28 A). Fluorescence imaging of labeled islets provided higher signal-to-noise ratio than ^{19}F MRI (Fig. 4.28 B).

In vitro ^{19}F MRI revealed incorporation of an average of $5.5\pm1.8 \times 10^{14}$ of ^{19}F per islet (approximately $5.5\pm1.8 \times 10^{11}$ of ^{19}F atoms per cell) after labeling using 17 mg/mL of PLGA-NPs (Fig. 4.28 D).

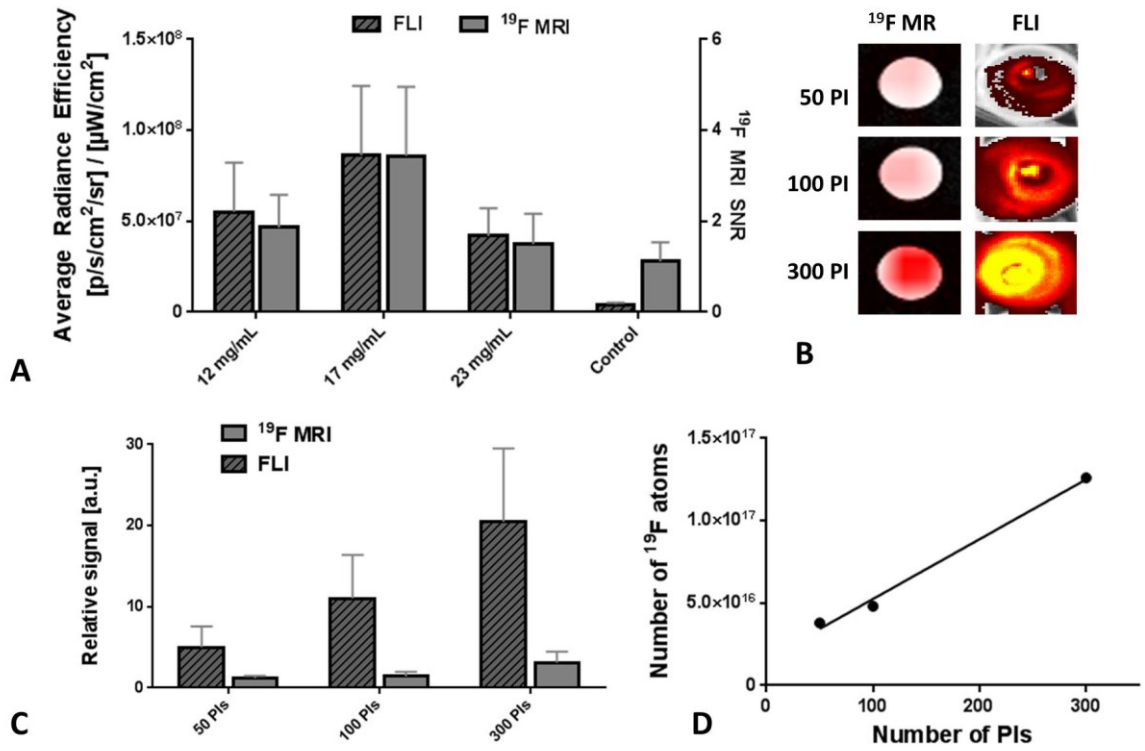

Fig. 4.28. ***In vitro*** **visualization of pancreatic islets labeled using endocytosis by ^{19}F MR and fluorescence imaging.** Comparison of signals originating from 300 islets labeled with different concentrations of nanoparticles (A). Representative ^{19}F MR (left) and FLI (right) images of different numbers of islets labeled using 17 mg/mL of PLGA-NPs (B). Visualization sensitivity of various numbers of islets labeled at a 17 mg/mL concentration (C), where the relative signal is normalized to the signal from the unlabeled islets. Absolute quantification of the number of ^{19}F atoms incorporated in labeled islets (D).

4) In vivo imaging of transplanted islets in rats

Labeled LUC+ islets were transplanted into the scaffolds implanted to rats. *In vivo* BLI imaging confirmed the presence of viable transplanted islets in the scaffolds throughout the entire 14-day experiment (Fig. 4.29 A). *In vivo* bioluminescence showed that labeling did not impair viability and survival of transplanted islets as the bioluminescence signal of the labeled islets was comparable to unlabeled controls. Both, labeled and unlabeled islets showed maximum bioluminescence on day 4 after transplantation, with the signal decreasing slightly by day 14 (Fig. 4.29 A).

The fluorescence signal originating from the labeled islets reached its maximum immediately after transplantation (day 1), before rapidly decreasing over the next week in all

experimental groups (Fig. 4.29 B). The difference between signal measured at day 1 and day 4 was 73% for labeling with 17 mg/mL of PLGA-NPs and 83% for 23 mg/mL of PLGA-NPs. Unlabeled islets provided no fluorescence signal at any point.

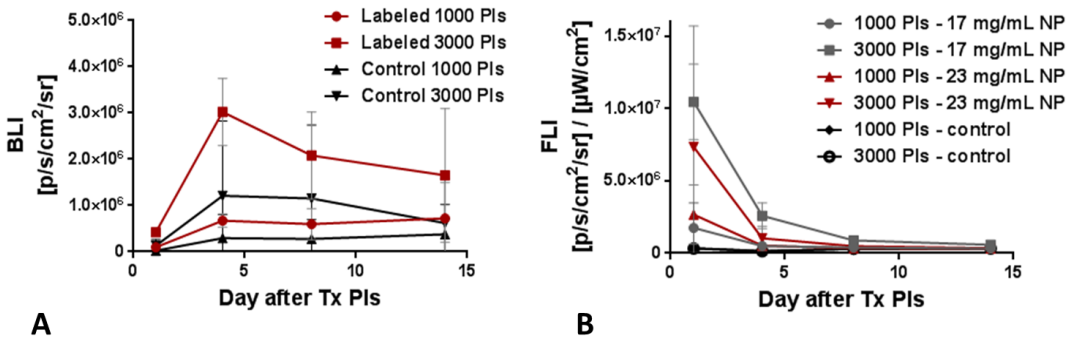

Fig. 4.29. Quantification of optical signals from transplanted islets. The time course of bioluminescence signals (BLI) originating from viable transplanted islets (A). Changes of fluorescence signal (FLI) of transplanted islets over time (B).

The localization of labeled islets inside the scaffolds was also confirmed by ^{19}F MR imaging (Fig. 4.30 A) throughout the whole examination. The absolute quantification revealed engraftment of average of 2300±200 and 1100±300 islets in the scaffolds on day 1, corresponding to 3000 and 1000 transplanted islets respectively (manually counted before transplantation). The maximum ^{19}F MR signal was detected on the first day after islet transplantation, after which the signal continuously declined. Islets labeled with 23 mg/mL of PLGA-NPs gave lower ^{19}F MR signal compared to islets labeled with 17 mg/mL of NPs throughout the whole examination (Fig. 4.30 B). Both 1000 and 3000 islets labeled with PLGA-NPs with concentration 17 mg/mL provided a detectable signal in the scaffolds during the whole examination (until day 14). The ^{19}F MR signal originating from the islets labeled with 23 mg/mL of NPs was significantly lower and reached the noise level on day 14, while ^{19}F MR signal originating from 1000 islets labeled with 17 mg/mL of PLGA-NPs was still above the noise level. The signal from 3000 islets labeled with 17 mg/mL of PLGA-NPs decreased to 66% of the starting value on day 8 and to 47% on day 14.

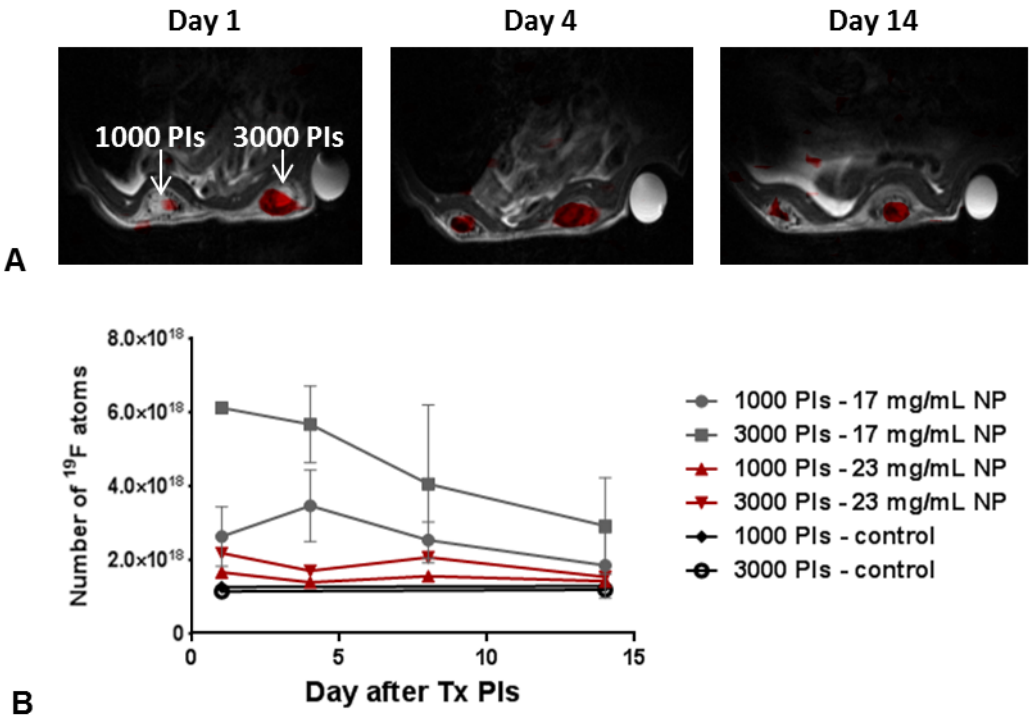

Fig. 4.30. ^{19}F MRI of transplanted islets. The representative ^{19}F MR images of pancreatic islets labeled using 17 mg/mL of PLGA-NPs and 23 mg/mL of PLGA-NPs in artificial scaffolds (A). Quantification of the ^{19}F MR signal from labeled islets (B).

The slow decline of the BLI and ^{19}F MR signals contrasted with the rapid decrease of FLI (Fig. 4.31). The ^{19}F MR signal strongly correlated with bioluminescence between days 4 and 14 ($R^2 = 0.99$).

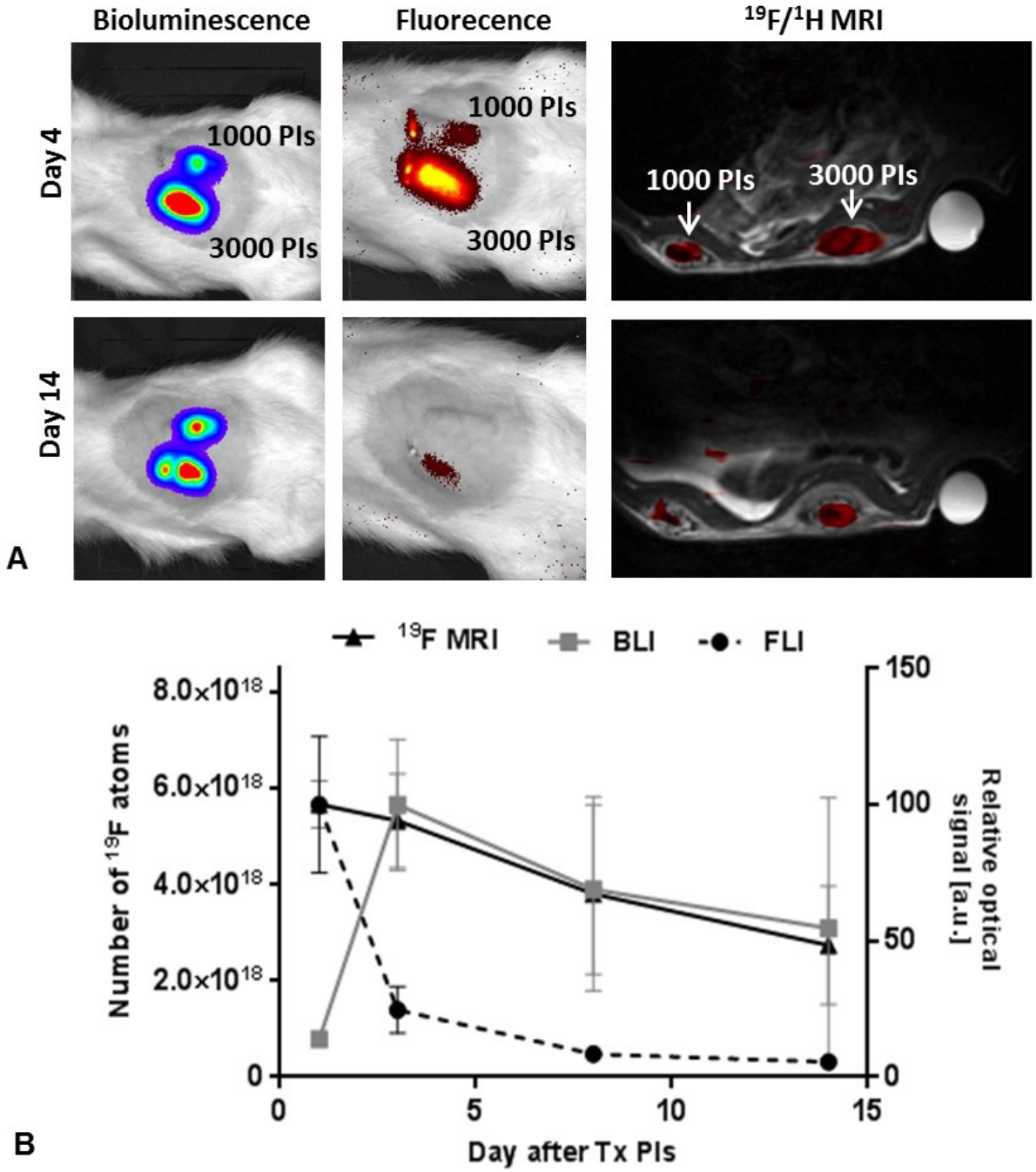

Fig. 4.31. Trimodal imaging of transplanted pancreatic islets in scaffolds. Representative bioluminescence, fluorescence and axial $^{19}F/^{1}H$ MR images of 1000 and 3000 pancreatic islets transplanted into scaffolds on days 4 and 14 (A). Time course of bioluminescence (BLI), fluorescence (FLI) and ^{19}F MRI signals for 3000 labeled transplanted islets (B). MRI signal is recalculated to the corresponding number of ^{19}F nuclei (left axis); the optical signals (BLI, FLI) are normalized to the maximum value (=100 %, right axis).

Histology

The histological analysis confirmed the presence of viable pancreatic islets in the central part of scaffolds (Fig. 4.32 A). Vascularized pancreatic islets distorted by fibrosis were present in the central parts of the scaffolds. Irregularly distributed clusters of cells co-expressing insulin and luciferase were detected immunohistochemically in all the islets (Fig. 4.32 B, C). Cells expressing both markers were arranged in trabeculae and occasional small ductular structures. Deposits of hemosiderin and foreign body granulomatous reaction composed of macrophages and multinucleated foreign body giant cells were detected in some islets.

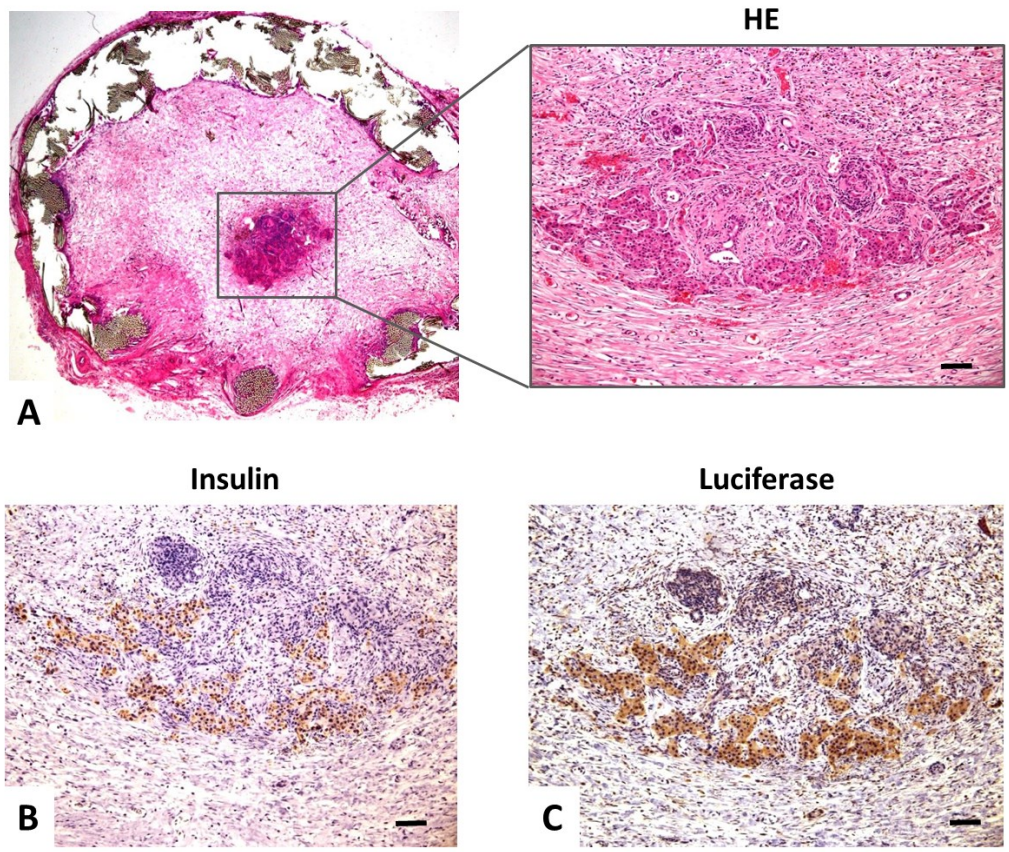

Fig. 4.32. Histology of scaffolds on day 14 after islet transplantation. The representative images of transplanted islets in a scaffold stained with hematoxylin and eosin (left magnification 20×) (A). A detail of the viable graft is shown at higher magnification on right (200×) (A). Immunohistochemical staining with the primary antibodies, anti-insulin (B) and anti-luciferase (C). Insulin- and luciferase-positive cells were present at the same locations within the graft. The scale bar corresponds to 100 µm.

4.3.3 Discussion

1) Sensitivity of visualization of the multimodal nanoparticles by ^{19}F MR and fluorescence imaging

The tested PLGA-NPs enable multimodal imaging. Incorporated ICG dye ensures high sensitivity of visualization by fluorescence imaging, which is advantageous for fast imaging (in range of seconds). A disadvantage of the tested PLGA-NPs is quenching of optical signal by local high ICG concentration due to decay of emission intensity and re-absorption of emission photons. This effect has been already described by Yuan et a. (Yuan et al. 2004) and it represents a limit for precise quantification of the fluorescence signal. Although quenching decreases reliability of quantification of the optical signal, it should be noted that under *in vivo* condition, islets may be more distributed and the effect of quenching will be smaller or even negligible. Whereas fluorescence signal decreased with increasing concentration due to quenching at high probe concentration, ^{19}F MR signal increased with increasing concentration. In contrary to fluorescence, sensitivity of visualization by ^{19}F MRI is lower and longer acquisition times are needed (minutes - hour). Besides high concentration of the ^{19}F contrast agent, lowering of spatial resolution is necessary to obtain sufficient signal. In our case, the lowest slice thickness reliable for visualization of the probe was 10 mm and in-plane matrix 32 × 32 (voxel size 24 μL). Although ^{19}F MR shows similar sensitivity compared to ^{1}H due to similar gyromagnetic ratio, concentration of fluorine atoms in the synthetized agents is extremely low (≈ mM) compared to protons in the tissues (≈ 100 M). The probe we used contained PFCE with 12 equivalent fluorine atoms, which partially compensated low fluorine concentration; however development of a probe with even higher fluorine content is still on demand.

2) Comparison of labeling procedures

Two methods for labeling of pancreatic islets were tested and compared: endocytosis and electroporation (microporation). Endocytosis has been used for labeling of pancreatic islets in a variety of studies (Jirák et al. 2004; Ferrauto et al. 2013). Labeling by endocytosis is an easy, widely used and effective procedure; however relatively time-consuming. Using endocytosis, the positively charged nanoparticles are preferable because of the negative

charge of the cell surface. Also electroporation is a widely used method for cell labeling; however there are only few studies focused on labeling of PIs. Tai et al. labeled PIs with SPIONs (Feridex with a poly-L-lysine transfection agent) using electroporation at lower voltage (100 – 500 V) (Foster et al. 2005; Tai et al. 2006).

Our results indicate that microporation is an invasive procedure in general and it led to substantial loss of islets during the procedure. Use of higher voltage or more than two pulses led to radical impairment of islet viability and decreased gain of harvested islets. It is worth to note that viability was assessed only on unbroken islets, therefore it does not reflect the overall lost or destruction of islets during the procedure. Moreover, microporation using a standard protocol when the islets are porated in a pipette together with PLGA-NPs is very difficult. In our case, suspension of the nanoparticles had turquoise color making visual control of the islets impossible and many islets could have been lost in the electrolytic buffer. Other obstacles were bubbles causing sparks during poration and harm the islets. The PLGA-NPs suspension at certain concentration is foamy probably due to hydrophilic surface of the polymer (Srinivas, Cruz, et al. 2010), which decreases surface tension and therefore the nanoparticle suspension behaves like a surfactant. During the procedure, visible bubbles were usually removed, nevertheless microbubbles could still be presented and cause sparks. According to our observations, the islets porated by the standard microporation procedure were often destructed due to the presence of sparks; however labeling by pre-microporation (the islets are presented in a pipette without nanoparticles) avoided these complications. The setting for pre-microporation was optimized as follows: two low voltage pulses (500 V - 600 V) with subsequent incubation on ice for 10 minutes. Ten minutes interval for incubation of islets with nanoparticles caused no damage to islet viability and it was in accord with the published data (Srinivas, Cruz, et al. 2010).

The observed discrepancy between ^{19}F and FLI signals from islets labeled by endocytosis in this experiment was probably caused by quenching of the fluorescence signal due to locally high nanoparticle concentration. Moreover, the nanoparticles might not be distributed homogenously within the islet pellets, which could also contribute to optical signal loss due to quenching and shielding (the optical signal was detected from the surface). Although pre-microporation was less efficient and more invasive (at higher voltage than 600 V) than endocytosis (3-fold lower uptake), it could be beneficial in applications when fast labeling is required.

3) Optimization of labeling by endocytosis

As low as 50 islets labeled by endocytosis were detected by *in vitro* imaging, although much higher amount was needed for sufficient visualization under *in vivo* conditions due to dispersion of islets in the scaffolds and attenuation of optical signal by the tissue.

Labeling by endocytosis retained viability and the therapeutic potential of labeled islets which was also proved by a comparable bioluminescence signal of labeled and unlabeled islets. The bioluminescence signal is dependent on presence of oxygen and adenosine triphosphate (ATP), therefore only viable cells emit photons in a bioluminescence reaction (Kim et al. 2015). Sufficient viability and insulin secretion of labeled islets was reached what corresponded to published non-toxicity of probes based on pefluorcarbons (Böhm-Sturm et al. 2011) and safety of chosen labeling method (Herynek et al. 2017). The same labeling nanoparticles have been used to label various subsets of primary human dendritic cells in preparation for clinical application (Srinivas et al. 2015). Thus, clinical application of this procedure is feasible. A strong correlation between islet number and detected fluorescence/bioluminescence signal confirmed reliability of optical imaging for detection of labeled islets and monitoring of their viability.

In vitro ^{19}F MRI and fluorescence imaging revealed some controversial results. Using endocytosis, the highest imaging signal was detected from islets labeled with 17 mg/mL of PLGA-NPs in contrast to concentration of 23 mg/mL. The labels (e.g. SPIONs) are usually present at the islet surface in the case of short labeling, while the particles are taken up in deeper islet structures after longer incubation time (Berkova et al. 2008). In our case, positively-charged fluorine nanoparticles could aggregate on islet surface even after long incubation time if the high concentration (≈ 23 mg/mL) was used. Nevertheless, labeling by 17 mg/mL of PLGA-NPs led to incorporation of $5.5\pm1.8 \times 10^{14}$ of ^{19}F per one islet (approximately $5.5\pm1.8 \times 10^{11}$ of ^{19}F spins), what is in accordance with the published data (range of 10^{11}-10^{13}) (Fink et al. 2018; Bonetto et al. 2012; Helfer et al. 2010).

4) In vivo monitoring of transplanted islets in rats

In this study, we used multimodal imaging to track pancreatic islets transplanted into subcutaneously implanted artificial scaffolds. This site possesses some benefits over the liver (Kříž, Greg, et al. 2012) and is suitable for examining transplanted cells using various imaging methods (Fabryova et al. 2014; Gálisová, Fábryová, Sticová, et al. 2017). In addition to the grafted islets being concentrated at one place, what is advantageous for *in vivo* ^{19}F MRI

detection, the scaffolds are implanted subcutaneously ensuring a short optical path for the fluorescence/bioluminescence signal emitted from the transplanted islets.

Labeling by endocytosis was chosen for *in vivo* experiments due to adverse effects of microporation. Transplanted islets were visualized in artificial scaffolds by all used imaging methods within two weeks. Bioluminescence confirmed the viability of islets in the scaffolds throughout the whole examination with only a partial decrease in islet mass. The *in vivo* results were in accordance with *in vitro* findings; the highest ^{19}F MR signal originated from islets labeled with 17 mg/mL of nanoparticles compared to 23 mg/mL concentration. Absolute quantification from ^{19}F MR images confirmed appropriate numbers of transplanted islets in scaffolds on day 1 after islet transplantation. 1000 islets were detectable by ^{19}F MR until day 4 in contrast to 3000 islets providing a sufficient ^{19}F signal for the whole examination (14 days). The decrease of the ^{19}F MR signal to 44% on day 14 corresponds with published experimental and clinical data reporting a gradual loss of transplanted islets within 2 weeks after transplantation (Saudek et al. 2010; Jirák et al. 2009). To our knowledge, this is the first evidence of longitudinal tracking of transplanted islets by ^{19}F MRI *in vivo*. Previous studies have visualized islets labeled with fluorine-containing probes at one time point post-transplantation only (Liang et al. 2017; Brad P; Barnett et al. 2011). It should be noted that due to the low sensitivity of ^{19}F MRI, long acquisition times (1 hour) were needed for visualize the transplanted grafts in our study. Low spatial resolution has been used to improve sensitivity, but it can also lead to the grafts being underestimated due to the spreading of the signal in the image voxel (Böhm-Sturm et al. 2011). Low detection sensitivity of *in vivo* ^{19}F MR has been also reported in other models, e.g., examination of carbohydrates sensitive to beta cells through GLUT-2 transporters in order to visualize transplanted islet (Liang et al. 2016) and tracking transplanted stem cells in the brain (Böhm-Sturm et al. 2011). However, the ability to quantify signals and estimate graft size without the use of radioactive probes represents a considerable advantage.

Inhomogeneous $\boldsymbol{B_1}$ excitation when using the surface RF coil is a further limitation. The ^{19}F MR signal is influenced not only by ^{19}F concentration, but also by the distance from the coil. Other errors in quantification of the ^{19}F MR signal may arise from filtering during post-processing, low measurement matrices and Fourier transform, potentially resulting in partial signal dispersion within the whole measurement matrix (Herynek et al. 2017; Amiri et al. 2015). To overcome these sensitivity problems and to increase ^{19}F SNR, various data acquisition methods, such as compressed sensing have been proposed (Liang et al. 2017).

Although fluorescence imaging was found to be a more sensitive method for cell tracking compared to ^{19}F MRI, we observed a steep decline in the *in vivo* fluorescence signal. Quenching of fluorescence signals originating from islets labeled using high concentrations of PLGA-NPs has been described previously (Herynek et al. 2017), but the fluorescence signal used in this model decreased rapidly within four days after transplantation. Fluorescence of labeled islets decreased to a noise level within 1 week, while ^{19}F MR and bioluminescence signals decreased only partially. This indicates the instability of the fluorescent dye (ICG) in the nanoparticles under *in vivo* conditions. Thermal degradation of ICG using other multifunctional perfluorocarbon nanoemulsions at temperatures above 37 °C has been previously reported (Bae et al. 2014). Alternatively, the dye may leak out of the islets over time (Swider et al. 2018). We hypothesize that these effects may have occurred in our model, thus limiting the reliability of *in vivo* fluorescence imaging. Therefore, in the absence of reporter genes, we did not use FLI with fluorescent dyes for longitudinal *in vivo* imaging.

The bioluminescence signal correlated strongly with the ^{19}F MR signal from the transplanted islets, which indicates that the probe was washed out after cell death. This finding is in apparent contradiction to a previously published study that used PFC-labeled neural stem cells (Böhm-Sturm et al. 2011). The authors of that study found that the agent remained in the tissue, while the ^{19}F MR signal persisted even after cell death in the case of stem cells transplanted into brain tissue. Another study, one that also used lipid-coated emulsions, found that perfluoro-crown-ether was retained at the site in a murine model of inflammation for several months (Jacoby et al. 2014). It should also be noted that the ^{19}F labels used in these studies were different (lipid-coated emulsion versus PLGA NPs). Furthermore, the islets in our study were transplanted into a well-vascularized site with good access to circulating macrophages. It may also be that the difference in formulation had a significant effect on the PFC clearance rate. We hypothesize that migrating macrophages remove the nanoparticles together with dead islets, thus eliminating their contribution to any false-positive results. In any case, clearance from dead cells is essential for avoiding false-positives, a major issue that we resolved through the use of PLGA-NPs.

Importantly, histology revealed viable islet grafts in scaffolds, both labeled and unlabeled islets. It is significant that insulin deposits were found at the same locations as luciferase molecules, which confirmed the functionality of transplanted LUC+ islets labeled using PLGA-NPs.

4.3.4 Summary – multimodal PLGA-based nanoparticles

- Labeling of PIs by multimodal PLGA-NPs was optimized: endocytosis was found to be a more efficient labeling process than microporation or pre-microporation
- A novel platform for *in vivo* multimodal tracking of transplanted PIs including bioluminescence, fluorescence and ^{19}F MRI was introduced
- Islets labeled with PLGA-NPs were tracked in artificial scaffolds for 2 weeks - the study represents the first reported ^{19}F MRI longitudinal *in vivo* tracking of PIs
- *In vivo* fluorescence signal was detected only within 4 days after PIs transplantation indicating instability of the fluorescent dye *in vivo*
- Correlation between the bioluminescence and ^{19}F MRI signals confirmed good clearance of PLGA-NPs from the transplantation site after cell death what addresses a major issue related to intracellular imaging labels
- The proposed imaging platform is therefore reliable for quantification of survived transplanted islets.

5 Conclusion

In this thesis, novel imaging approaches for visualization of pancreatic islets were examined with the aim of improvement of islet monitoring after transplantation. Magnetic resonance and optical imaging were implemented for this purpose, namely CEST MR approach, ^{19}F MR imaging, fluorescence and bioluminescence imaging.

CEST as a frequency-selective approach has a great potential for MR imaging; however our results pointed out to low sensitivity of the method for cell imaging and high toxicity of the tested CEST probes. Labeled islets were successfully visualized only *in vitro* and within long acquisition times. Increase of labeling concentration had adverse effect on cell viability. Therefore, the use of the CEST agents as exogenous labels for PIs and their *in vivo* application is at current instrumental setting inappropriate.

Multimodal imaging with bioluminescence and MR imaging was used for optimization of a transplantation protocol at an alternative transplant site – artificial scaffolds. Transplantation of a suboptimal PIs mass on day 4 after rod removal from scaffolds was found to be superior in comparison to day 7 due to higher islet viability and vascularization. Using the optimized protocol, long-term normoglycemia was induced in more than 80% of experimental animals, therefore the model holds a potential for further clinical applications.

Three imaging modalities, including specific ^{19}F MRI and sensitive optical imaging were applied for monitoring of PIs transplanted using the optimized transplantation protocol. Multimodal probes can provide complementary information about distribution and viability of transplanted grafts. Quantification of ^{19}F MRI signals assessed absolute numbers of transplanted islets in scaffolds over time. The bioluminescence signal correlated with the ^{19}F MR signal indicating clearance of PLGA-NPs from the transplantation site after cell death eliminating false positive data. This result addresses one of the major issues of intracellular imaging labels. The proposed imaging platform is therefore reliable for quantification of survived transplanted islets.

The work contributes to the improvement of transplantation protocol for pancreatic islets and may help to monitor non-invasively the distribution and viability of transplanted islets or processes causing rejection. Moreover, multimodal imaging might speed up translation of these alternative transplant models into clinical practice.

6 List of publications

6.1 Publications related to the thesis

(1) **Gálisová A**, Jirák D, Krchová T, Herynek V, Fábryová E, Kotek J, Hájek M. Magnetic resonance visualization of pancreatic islets labeled by PARACEST contrast agents at 4.7 T. *Journal of Molecular Imaging and Dynamics 2016*; 6:121. **IF: 2**

(2) Fabryova E, Jirak D, Girman P, Zacharova K, **Galisova A**, Saudek F, Kriz J. Effect of Mesenchymal Stem Cells on the Vascularization of the Artificial Site for Islet Transplantation in Rats. *Transplantation Proceeding 2014*; 46:1963-1966. **IF: 0.9**

(3) **Gálisová A**, Fábryová E, Jirák D, Sticová E, Lodererová A, Herynek V, Kříž J, Hájek M. Multimodal imaging reveals improvement of blood supply to an artificial cell transplant site induced by bioluminescent mesenchymal stem cells. *Molecular Imaging and Biology 2017*; 19(1):15-23. **IF: 3.5**

(4) Krchová T, **Gálisová A**, Jirák D, Hermann P, Kotek J. Ln(iii)-complexes of a DOTA analogue with an ethylenediamine pendant arm as pH-responsive PARACEST contrast agents. *Dalton Transactions 2016*; 45(8):3486-96. **IF: 4.0**

(5) **Gálisová A**, Fábryová E, Sticová E, Kosinová L, Jirátová M, Herynek V, Berková Z, Kříž J, Hájek M, Jirák D. The optimal timing for pancreatic islet transplantation into subcutaneous scaffolds assessed by multimodal imaging. *Contrast Media and Molecular Imaging 2017*. Article ID 5418495. **IF: 3.3**

(6) Herynek V, **Gálisová A**, Srinivas M, van Dinther EAW, Kosinová L, Ruzicka J, Jirátová M, Kriz J, Jirák D. Pre-Microporation Improves Outcome of Pancreatic Islet Labeling for Optical and ^{19}F MR Imaging. *Biological Procedures Online 2017*; 19:6. **IF: 2.0**

(7) **Gálisová A**, Herynek V, Srinivas M, Swider E, Sticová E, Kosinová L, Pátiková A, Kříž J, Hájek M, Jirák D. A novel trimodal platform for tracking of transplanted pancreatic islets: 19F MR, fluorescence and bioluminescence imaging. *Submitted to Molecular Imaging and Biology*. **IF: 3.5**

6.2 Other publications

(1) **Galisova A**, Bačiak L, Jozefovičová M, Kukurova J I, Kebis A, Ambrusova K, Dubovicky M, Estera, Sadlonova I, Kronnerwetter C, Berg A, Krssak M, Kasparova S. Pathophysiological rat model of vascular dementia: magnetic resonance spectroscopy, microimaging and behavioral study. *Brain Research 2014*; 1568:10-20. **IF: 2.8**

(2) Blahut J, Hermann P, **Gálisová A**, Herynek V, Cisarova I, Tošner Z, Kotek J. Nickel(II) complexes of N–CH2CF3 cyclam derivatives as contrast agents for 19F magnetic resonance imaging. *Dalton Transactions 2016*; 45: 474-478. **IF: 4.0**

(3) Blahut J, Bernášek K, **Gálisová A**, Herynek V, Císařová I, Kotek J, Lang J, Matějková S, Hermann P. Paramagnetic 19F Relaxation Enhancement in Nickel(II) Complexes of N‑Trifluoroethyl Cyclam Derivatives and Cell Labeling for ^{19}F MRI. *Inorganic Chemistry 2017*; 56:13337-13348. **IF: 4.9**

(4) Krchová T, Herynek V, **Gálisová A**, Blahut J, Hermann P, Kotek J. Eu(III) Complex with DO3A-amino-phosphonate Ligand as a Concentration-Independent pH-Responsive Contrast Agent for Magnetic Resonance Spectroscopy (MRS). *Inorganic Chemistry 2017*; 56 (4), 2078–2091. **IF: 4.9**

(5) Šmejkalová D, Nešporová K, Huerta-Angeles G, Syrovátka J, Jirák D, **Gálisová A**, Velebný V. Selective In Vitro Anticancer Effect of Superparamagnetic Iron Oxide Nanoparticles Loaded in Hyaluronan Polymeric Micelles. *Biomacromolecules 2014*. 15(11): 4012-4020. **IF: 5.2**

(6) Herynek V, Turnovcová K, Veverka P, Dědourková T, Žvátora P, Jendelová P, **Gálisová A**, Kosinová L, Jiráková K, Syková E. Using ferromagnetic nanoparticles with low Curie temperature for magnetic resonance imaging-guided thermoablation. *International Journal of Nanomedicine 2016*; 11:3801-3811. **IF: 4.4**

(7) Jirátová M, Pospíšilová A, Rabyk M, Pařízek M, Kovář J, **Gálisová A**, Hrubý M, Jirák D. Biological characterization of a novel hybrid copolymer carrier system based on glycogen. *Drug Delivery and Translation Research 2018*; 8(1):73-82. **IF: 3.1**

(8) Rabyk M, **Galisova A**, Jiratova M, Patsula V, Srbova L, Loukotova L, Jirak D, Stepanek P, Hruby M. Mannan-based conjugates as multimodal imaging platform for sentinel lymph nodes. *Journal of Materials Chemistry B 2018*. **IF: 4.5**

(9) Šedivý P, Herynek V, Dezortová M, Drobný M, **Gálisová A**, Hájek M. ^{31}P and ^{19}F MR spectroscopy and imaging in IKEM. *Česká radiologie 2017*; 71(4):312-322. **no IF**

6.3 First-author presentations related to the thesis

Galisova A, Jirak D, Herynek V, Krchova T, Fabryova E, Kotek J, Hajek M. Visualization of pancreatic islets labeled by two PARACEST contrast agents. International Workshop „Magnetic Resonance Studies“ 2013, Germany (oral presentation)

Galisova A, Jirak D, Herynek V, Krchova T, Fabryova E, Kotek J, Hajek M. Visualization of pancreatic islets labeled by PARACEST agent, Annual Scientific Meeting of European Society for Magnetic Resonance in Medicine and Biology (ESMRMB) Scientific Meeting 2013, France (electronic poster + 2 min talk)

Galisova A, Herynek V, Jirak D, Kriz J, Dovolilova E, van Dinther E, Srinivas M, de Vries J, Hajek M. Comparison of procedures for labeling of pancreatic islets by ^{19}F MRI and optical imaging probes, Annual Scientific Meeting of European Society for Magnetic Resonance in Medicine and Biology (ESMRMB) Scientific Meeting 2013, France (oral presentation)

Gálisová A, Jirák D, Herynek V, Fábryová E, Dovolilová E, Kříž J, Hájek M. Dynamic MRI and optical imaging of an artificial cell transplant site. International Workshop „Magnetic Resonance Studies“ 2014, Czech Republic (oral presentation)

Gálisová A, Jirák D, Herynek V, Fábryová E, Dovolilová E, Kříž J, Hájek M. The Effect of Mesenchymal Stem Cells on Vascularization of an Artificial Cell Transplant Site studied by DCE MR and Optical Imaging, Annual Joint Meeting of ISMRM and ESMRMB 2014, Italy (traditional poster)

Gálisová A, Jirák D, Herynek V, Fábryová E, Dovolilová E, Kříž J, Hájek M. Improvement of Blood Supply to an Artificial Transplant Site after Stem Cells Implantation studied by DCE MR and Bioluminescence Imaging, European Molecular Imaging Meeting 2014, Belgium (traditional poster)

Gálisová A, Jirák D, Fábryová E, Kosinová L, Herynek V, Kříž J, Hájek M. Bioluminiscenční potkani a jejich využití v experimentálním modelu léčby diabetu. 8. výzkumné fórum "Pyramida" 2015, Czech Republic (oral presentation)

Gálisová A, Jirák D, Fábryová E, Herynek V, Kosinová L, Kříž J, Hájek. Multimodal imaging of an artificial transplant site for pancreatic islets supported with mesenchymal stem cells. European Molecular Imaging Meeting 2015, Germany (oral presentation)

Gálisová A, Jirák D, Fábryová E, Herynek V, Kosinová L, Kříž J, Hájek. Monitoring the pancreatic islets implantation in the subcutaneous polymeric scaffolds by DCE MRI and optical imaging, 23rd Annual Meeting of International Society for Magnetic Resonance in Medicine (ISMRM) 2015, Canada (electronic poster)

Gálisová A, Herynek V, Jirák D, Martinisková M, Kotek J, Hájek M. Pilot ^{19}F MRI experiments at IKEM. International Workshop „Magnetic Resonance Studies" 2015, Austria (oral presentation)

Galisova A, Fabryova E, Jirák D, Herynek V, Kosinova L, Jiratova M, Kriz J, Hajek M. Multimodal imaging of pancreatic islets transplanted into the artificial scaffolds. Annual Scientific Meeting of European Society for Magnetic Resonance in Medicine and Biology (ESMRMB) Scientific meeting 2015, UK, Program No. 547 (electronic poster)

Gálisová A, Fábryová E, Jirák D, Kosinová L, Jirátová M, Saudek F, Hájek M, Kříž J. Určení vhodného načasování transplantace pankreatických ostrůvků do arteficiálních podkožních

skeletů pomocí zobrazovacích metod. 52. Diabetologické dny 2016. Czech Republic (traditional poster)

Gálisová A, Fábryová E, Kosinová L, Jirátová M, Herynek V, Kříž J, Hájek M, Jirák D. Assessment of an optimal timing for transplantation of pancreatic islets into the artificial scaffolds by multimodal imaging, World Molecular Imaging Meeting 2016, USA (oral talk)

- **awarded for the best pre-clinical paper**

6.4 Other first-author presentations

Galisova A, Jirák D, Deligianni X, Drobny M, Sedivy P, Herynek V, Hajek M. Important biomarkers related to the MRI-estimated whole liver fat content in the healthy volunteers and type 1 diabetic patients. Annual Scientific Meeting of European Society for Magnetic Resonance in Medicine and Biology (ESMRMB) Scientific meeting 2015, UK (electronic poster + 2 min talk)

Gálisová A, Jirák D, Jirátová M, Rabyk M, Hrubý M, Hájek M. In vivo MR zobrazování tumorů pomocí kontrastních látek na bázi glykogenu. 9. výzkumné fórum Pyramida 2016, Czech Republic (oral talk)

Galisova A, Jirak D, Jiratova M, Hruby M, Rabyk M, Pospisilova A, Hajek M. Biodegradable glycoged-based nanoprobe as a multimodal tumor-targeting contrast agent. 24rd Annual Meeting of International Society for Magnetic Resonance in Medicine (ISMRM) 2016, Singapore, Program number: 2309 (traditional poster)

Gálisová A, Jirák D, Hrubý M, Sedláček O, Hájek M. A novel thermoresponsive agent for ^{19}F molecular imaging. 33rd Annual Scientific Meeting of European Society for Magnetic Resonance in Medicine and Biology (ESMRMB) 2016, Austria (electronic poster + 2 min talk)

- **awarded by the Certificate of Merit**

Gálisová A, Jirátová M, Sticová E, Hrubý M, Rabyk M, Hájek M, Jirák D. Multimodální polysacharidové „drug delivery" systémy pro nádorovou teranostiku. 10. Výzkumné forum Pyramida 2017, Czech Republic (oral talk)

Gálisová A, Jirátová M, Hrubý M, Rabyk M, Hájek M, Jirák D. A Novel Multimodal Mannan-Based Polymer System Suitable for Tumor and Metastasis Diagnosis. 25th Annual Meeting of International Society for Magnetic Resonance in Medicine (ISMRM) 2017, USA. Program number: 3573 (electronic poster)

Gálisová A, Jirátová M, Rabyk M, Hrubý M, Hájek M, Jirák D. Preklinické testování mananových konjugátů určených pro nádorovou teranostiku. 11. Výzkumné forum Pyramida 2018, Czech Republic (oral talk)

Galisova A, Jiratova M, Rabyk M, Sticova E, Hruby M, Hajek M, Jirak D. A novel glycogen-based probe for tumor imaging and drug delivery. Annual Scientific Meeting of European Society for Magnetic Resonance in Medicine and Biology (ESMRMB) Scientific meeting 2017, Spain, Program number: 426 (oral talk)

Galisova A, Jiratova M, Rabyk M, Hruby M, Hajek M, Jirak D. A novel mannan-based probe for multimodal imaging of cancer and inflammation. European Molecular Imaging Meeting 2018, Spain (paper poster)

- **awarded by a poster award**

7 References

Ahrens, E. et al., 2014. Clinical cell therapy imaging using a perfluorocarbon tracer and fluorine-19 MRI. *Magnetic Resonance in Medicine*, 72(6), pp.1696–1701.

Ahrens, E.T. & Bulte, J., 2013. Tracking immune cells in vivo using magnetic resonance imaging. *Nat Rev Immunol*, 13(10), pp.755–63.

Aime, S. et al., 2005. Tunable imaging of cells labeled with MRI-PARACEST agents. *Angewandte Chemie (International ed. in English)*, 44(12), pp.1813–5.

Amiri, H. et al., 2015. Cell tracking using (19)F magnetic resonance imaging: technical aspects and challenges towards clinical applications. *Eur Radiol*, 25(3), pp.726–35.

Antkowiak, P.F. et al., 2012. Manganese-Enhanced Magnetic Resonance Imaging Detects Declining Pancreatic Cell Mass in a Cyclophosphamide - Accelerated Mouse Model of Type 1 Diabetes. *Diabetes*, 62(1), pp.44–48.

Arbab, A. et al., 2004. Comparison of Transfection Agents in Forming Complexes with Ferumoxides, Cell Labeling Efficiency, and Cellular Viability. *Molecular Imaging*, 3(1).

Arifin, D. et al., 2013. Microencapsulated cell tracking. *NMR in Biomedicine*, 26(7), pp.850–9.

Arifin, D.R. et al., 2011. Trimodal gadolinium-gold microcapsules containing pancreatic islet cells restore normoglycemia in diabetic mice and can be tracked using positive contrast MR, CT, and ultrasound imaging. *Radiology*, 260(3), pp.790–8.

Atkinson, M.A., Eisenbarth, G.S. & Michels, A., 2014. Type 1 diabetes. *The Lancet*, 383(9911), pp.69–82.

Bae, P.K., Jung, J. & Chung, B.H., 2014. Highly enhanced optical properties of indocyanine green/perfluorocarbon nanoemulsions for efficient lymph node mapping using near-infrared and magnetic resonance imaging. *Nano Convergence*, 1, p.6.

Bank, H., 1987. Assessment of islet cell viability using fluorescent dyes. *Diabetologia*.

Barnett, B.P. et al., 2011. Fluorocapsules for improved function, immunoprotection, and visualization of cellular therapeutics with MR, US, and CT imaging. *Radiology*, 182–191.

Barnett, B.P. et al., 2007. Magnetic resonance-guided, real-time targeted delivery and imaging of magnetocapsules immunoprotecting pancreatic islet cells. *Nature Medicine*, 13(8), pp.986–991.

Barnett, B.P. et al., 2006. Radiopaque alginate microcapsules for X-ray visualization and immunoprotection of cellular therapeutics. *Molecular Pharmaceutics*, 3(5), pp.531–538.

Barnett, B.P. et al., 2011. Use of perfluorocarbon nanoparticles for non-invasive multimodal cell tracking of human pancreatic islets. *Contrast Media Mol Imaging*, 6(4), pp.251–259.

Barton, F.B. et al., 2012. Improvement in outcomes of clinical islet transplantation: 1999-2010. *Diabetes care*, 35(7), pp.1436–45.

van Belle, T., Coppieters, K. & von Derrath, M., 2011. Type 1 diabetes: etiology, immnunology, and therapeutic strategies. *Physiological Reviews*, 91(1), pp.79–118.

Berkova, Z. et al., 2008. Labeling of pancreatic islets with iron oxide nanoparticles for in vivo detection with magnetic resonance. *Transplantation*, 85(1), pp.155–159.

Biancone, L. et al., 2007. Magnetic resonance imaging of gadolinium-labeled pancreatic islets for experimental transplantation. *NMR in Biomedicine*, 20(1), pp.40–48.

Böhm-Sturm, P. et al., 2014. A multi-modality platform to image stem cell graft survival in the naïve and stroke-damaged mouse brain. *Biomaterials*, 35(7), pp.2218–2226.

Böhm-Sturm, P. et al., 2011. In Vivo Tracking of Human Neural Stem Cells with Magnetic Resonance Imaging. *PLoS ONE*, 6(12), p.e29040.

Bonetto, F. et al., 2012. A novel 19F agent for detection and quantification of human dendritic cells using magnetic resonance imaging. *Int J Cancer*, 129(2), pp.365–373.

Boomsma, R. & Geenen, D., 2012. Mesenchymal stem cells secrete multiple cytokines that promote angiogenesis and have contrasting effects on chemotaxis and apoptosis. *PLoS ONE*, 7(4), p.e35685.

Bornhop, D. et al., 2001. Advance in contrast agents, reporters, and detection. *J Biomed Opt*, 6(2), pp.106–10.

Brom, M. et al., 2014. Non-invasive quantification of the beta cell mass by SPECT with ^{111}In-labelled exendin. *Diabetologia*, 57(5), pp.950–9.

Bulte, J. et al., 2004. Chondrogenic differentiation of mesenchymal stem cells is inhibited after magnetic labeling with ferumoxides. *Blood*, 104(10), pp.3410–2.

Cai, K. et al., 2012. Magnetic Resonance imaging of glutamate. *Nature medicine*, 18(2), pp.302–6.

Cantarelli, E. & Piemonti, L., 2011. Alternative transplantation sites for pancreatic islet grafts. *Curr*

Diab Rep, 11(5), pp.364–74.

Cao, Y. et al., 2005. Human adipose tissue-derived stem cells differentiate into endothelial cells in vitro and improve postnatal neovascularization in vivo. *Biochemical and biophysical research communications*, 332(2), pp.370–9.

Delaune, V. et al., 2017. Intraportal islet transplantation: the impact of the liver microenvironment. *Transpl Int*, 30(3), pp.227–238.

Delli Castelli, D. et al., 2014. In vivo maps of extracellular pH in murine melanoma by CEST-MRI. *Magnetic resonance in medicine*, 71(1), pp.326–332.

Ding, D., Shyu, W. & Lin, S., 2011. Mesenchymal stem cells. *Cell Transplantation*, 20(1), pp.5–14.

Dixon, W. et al., 2010. A concentration-independent method to measure exchange rates in PARACEST agents. *Magn Reson Med*, 63(3), pp.625–632.

Eriksson, O. et al., 2014. Positron emission tomography ligand [11C]5-hydroxy-tryptophan can be used as a surrogate marker for the human endocrine pancreas. *Diabetes*, 63(10), pp.3428–37.

Eriksson, O. et al., 2016. Positron Emission Tomography to Assess the Outcome of Intraportal Islet Transplantation. *Diabetes*, 65(9), pp.2482–2489.

Evgenov, N. V et al., 2006. In vivo imaging of islet transplantation. *Nature medicine*, 12(1), pp.144–8.

Fabryova, E. et al., 2014. Effect of mesenchymal stem cells on the vascularization of the artificial site for islet transplantation in rats. *Transplantation proceedings*, 46(6), pp.1963–6.

Farrell, T., Patterson, M. & Wilson, B., 1992. A diffusion theory model of spatially resolved, steady-state diffuse reflectance for the noninvasive determination of tissue optical properties in vivo. *Med Phys*, 19(4), pp.879–88.

Ferrauto, G. et al., 2013. In vivo MRI visualization of different cell populations labeled with PARACEST agents. *Magnetic resonance in medicine*, 69(6), pp.1703–11.

Ferrauto, G. et al., 2014. Lanthanide-loaded erythrocytes as highly sensitive chemical exchange saturation transfer MRI contrast agents. *Journal of the American Chemical Society*, 136(2), pp.638–41.

Fiallo-Scharer, R. et al., 2011. Factors predictive of severe hypoglycemia in type 1 diabetes: analysis from the Juvenile Diabetes Research Foundation continuous glucose monitoring randomized control trial dataset. *Diabetes care*, 34(4), pp.586–90.

Figliuzzi, M. et al., 2009. Bone marrow-derived mesenchymal stem cells improve islet graft function in diabetic rats. *Transplantation proceedings*, 41(5), pp.1797–800.

Fink, C. et al., 2018. 19F-perfluorocarbon-labeled human peripheral blood mononuclear cells can be detected in vivo using clinical MRI parameters in a therapeutic cell setting. *Scientific Reports*, 8(1), p.590.

Foster, P. et al., 2005. Cellular imaging of individual pancreatic islets using electroporation and 3DFIESTA at 1.5 Tesla. *Proc Intl Soc Mag Reson Med*, 13, p.361.

Fowler, M. et al., 2005. Assessment of Pancreatic Islet Mass after Islet Transplantation Using In Vivo Bioluminescence Imaging. *Transplantation*, 79(7), pp.768–776.

Fröhlich, E., 2012. The role of surface charge in cellular uptake and cytotoxicity of medical nanoparticles. *Int J Nanomedicine*, 7, pp.5577–91.

Gala-Lopez, B.L. et al., 2016. Subcutaneous clinical islet transplantation in a prevascularized subcutaneous pouch – preliminary experience. *CellR4*, 4(5), p.e2132.

Gálisová, A. et al., 2016. Magnetic Resonance Visualization of Pancreatic Islets Labeled by PARACEST Contrast Agents at 4.7 T. *Journal of Molecular Imaging & Dynamics*, 6(1), pp.4–10.

Gálisová, A., Fábryová, E., Jirák, D., et al., 2017. Multimodal Imaging Reveals Improvement of Blood Supply to an Artificial Cell Transplant Site Induced by Bioluminescent Mesenchymal Stem Cells. *Molecular Imaging and Biology*, 19(1), pp.15–23.

Gálisová, A., Fábryová, E., Sticová, E., et al., 2017. The Optimal Timing for Pancreatic Islet Transplantation into Subcutaneous Scaffolds Assessed by Multimodal Imaging. *Contrast Media and Molecular Imaging*, p.5418495.

Gao, H., Shi, W. & Freund, L., 2005. Mechanics of receptor-mediated endocytosis. *Proc Natl Acad Sci USA*, 102(27), pp.9469–74.

Gaudet, J. et al., 2015. Tracking the Fate of Stem Cell Implants with fluorine-19 MRI. *PLoS ONE*, 10(3), p.e0118544.

Gotoh, M. et al., 1985. An improved method for isolation of mouse pancreatic islets. *Transplantation*, 40, pp.437–8.

de Graaf, R., 2007. In Vivo NMR Spectroscopy. *John Wiley & Sons*, ISBN 97804, pp.43–231.

Grad, J. & Bryant, R., 1990. Nuclear magnetic cross-relaxation spectroscopy. *J Magn Resonance*,

90(1), pp.1–8.

Di Gregorio, E. et al., 2013. Gd loading by hypotonic swelling: an efficient and safe route for cellular labeling. *Contrast media & molecular imaging*, 8(6), pp.475–86.

Hakamata, Y., Murakami, T. & Kobayashi, E., 2006. "Firefly rats" as an organ/cellular source for long-term in vivo bioluminescent imaging. *Transplantation*, 81(8), pp.1179–84.

Haris, M. et al., 2011. In vivo mapping of brain myo-inositol. *NeuroImage*, 54(3), pp.2079–85.

Harlan, D. et al., 2009. Current advances and travails in islet transplantation. *Diabetes*, 58(10), pp.2175–84.

Harlan, D., 2016. Islet Transplantation for Hypoglycemia: Unawareness/Severe Hypoglycemia: Caveat Emptor. *Diabetes care*, 39(7), pp.1072–1074.

Hathout, E. et al., 2009. In vivo imaging demonstrates a time-line for new vessel formation in islet transplantation. *Pediatr Transplant*, 13(7), pp.892–7.

Helfer, B. et al., 2010. Functional assessment of human dendritic cells labeled for in vivo (19)F magnetic resonance imaging cell tracking. *Cytotherapy*, 12(2), pp.238–50.

Hematti, P. et al., 2013. Potential role of mesenchymal stromal cells in pancreatic islet transplantation. *Transplantation reviews (Orlando)*, 27(1), pp.21–9.

Herynek, V. et al., 2011. Improved detection of pancreatic islets in vivo using double contrast. *Contrast Media and Molecular Imaging*, 6(4), pp.308–13.

Herynek, V. et al., 2017. Pre-Microporation Improves Outcome of Pancreatic Islet Labelling for Optical and 19F MR Imaging. *Biological Procedures Online*, 19, p.6.

Chaikof, E., 1999. Engineering and material consideration in islet cell transplantation. *Annual Reviews of Biomedical Engineering*, 1, pp.103–127.

Chen, X. et al., 2006. In vivo bioluminescence imaging of transplanted islets and early detection of graft rejection. *Transplantation*, 81(10), pp.1421–7.

Chen, X. & Kaufman, D.B., 2009. Bioluminescence Imaging of Transplanted Islets P. B. Rich & C. Douillet, eds. *Methods in Molecular Biology*, 574, pp.1–10.

Ishimaru, A., 1978. Wave propagation and Scattering in Random Media. *Elsevier*, ISBN: 978-.

Ito, T. et al., 2010. Mesenchymal stem cell and islet co-transplantation promotes graft revascularization and function. *Transplantation*, 89(12), pp.1438–45.

Jacoby, C. et al., 2014. Probing different perfluorocarbons for in vivo inflammation imaging by 19F MRI: Image reconstruction, biological half-lives and sensitivity. *NMR in Biomedicine*, 27(3), pp.261–271.

Jirák, D. et al., 2009. Monitoring the survival of islet transplants by MRI using a novel technique for their automated detection and quantification. *Magnetic Resonance Materials in Physics, Biology and Medicine*, 22(4), pp.257–65.

Jirák, D. et al., 2004. MRI of transplanted pancreatic islets. *Magnetic resonance in medicine*, 52(6), pp.1228–33.

Johansson, U. et al., 2008. Formation of Composite Endothelial Cell – Mesenchymal. *Diabetes*, 57(10), pp.2393–2401.

Kagiwada, H. et al., 2008. Human mesenchymal stem cells as a stable source of VEGF-producing cells. *Journal of Tissue Engineering and Regenerative Medicine*, 2(4), pp.184–189.

Kawahara, T. et al., 2011. Portal vein thrombosis is a potentially preventable complication in clinical islet transplantation. *American journal of transplantation*, 11(12), pp.2700–2707.

Kerby, A. et al., 2013. Co-transplantation of islets with mesenchymal stem cells in microcapsules demonstrates graft outcome can be improved in an isolated-graft model of islet transplantation in mice. *Cytotherapy*, 15(2), pp.192–200.

Kim, H. et al., 2007. Registration of Sheep Brain MR Images for Cell Tracking Using Ferrite-Composite Micro-Beads as Markers. In *Engineering in Medicine and Biology Society*.

Kim, J., Kalimuthu, S. & Ahn, B., 2015. In vivo cell tracking with bioluminescence imaging. *Nuclear Medicine and Molecular Imaging*, 49(1), pp.3–10.

Kim, M. et al., 2009. WAter Saturation Shift Referencing (WASSR) for chemical exchange saturation transfer experiments. *Magnetic Resonance in Medicine*, 61(6), pp.1441–1450.

Kingsley, P. & Monahan, W., 2000. Effects of off-resonance irradiation, cross-relaxation, and chemical exchange on steady-state magnetization and effective spin-lattice relaxation times. *J Magn Reson*, 143(2), pp.360–75.

Koblas, T. et al., 2005. Magnetic resonance imaging of intrahepatically transplanted islets using paramagnetic beads. *Transplantation proceedings*, 37(8), pp.3493–5.

Kogan, F. et al., 2014. In vivo CEST Imaging of Creatine (CrCEST) in Skeletal Muscle at 3T. *J Magn Reson Imaging*, 40(3), pp.596–602.

Korsgren, O. et al., 2008. Optimising islet engraftment is critical for successful clinical islet transplantation. *Diabetologia*, 51(2), pp.227–32.

Kotková, Z. et al., 2010. Cyclodextrin-based bimodal fluorescence/MRI contrast agents: an efficient approach to cellular imaging. *Chemistry*, 16(33), pp.10094–102.

Krchová, T. et al., 2013. Lanthanide(III) complexes of aminoethyl-DO3A as PARACEST contrast agents based on decoordination of the weakly bound amino group. *Dalton transactions*, 42(44), pp.15735–47.

Krock, B., Skuli, N. & Simon, M., 2011. Hypoxia-induced Angiogenesis. *Genes Cancer*, 2(12), pp.1117–33.

Kříž, J., Greg, V., et al., 2012. A novel technique for the transplantation of pancreatic islets within a vascularized device into the greater omentum to achieve insulin independence. *American journal of surgery*, 203(6), pp.793–7.

Kříž, J., Jirák, D., et al., 2012. Detection of pancreatic islet allograft impairment in advance of functional failure using magnetic resonance imaging. *Transplant international : official journal of the European Society for Organ Transplantation*, 25(2), pp.250–60.

Largiader, F., Kolb, E. & Binswanger, U., 1980. A long-term functioning human pancreatic islet allotransplant. *Transplantation*, 29(1), pp.76–7.

Liang, S. et al., 2017. Comparison of different compressed sensing algorithms for low SNR 19F MRI applications — Imaging of transplanted pancreatic islets and cells labeled with perfluorocarbons. *NMR in Biomedicine*, 30(11), p.e3776.

Liang, S. et al., 2016. In vivo and ex vivo 19-fluorine magnetic resonance imaging and spectroscopy of beta-cells and pancreatic islets using GLUT-2 specific contrast agents. *Contrast Media and Molecular Imaging*, 11(6), pp.506–513.

Lim, F. & Sun, A., 1980. Microencapsulated islets as bioartificial endocrine pancreas. *Science*, 210(4472), pp.908–10.

Lim, J.Y. et al., 2010. Microporation is a valuable transfection method for efficient gene delivery into human umbilical cord blood-derived mesenchymal stem cells. *BMC Biotechnology*, 10, p.38.

Liu, G. et al., 2010. High-throughput screening of chemical exchange saturation transfer MR contrast agents. *Contrast Media and Molecular Imaging*, 5(3), pp.162–170.

Liu, G. et al., 2012. In vivo multicolor molecular MR imaging using diamagnetic chemical exchange

saturation transfer liposomes. *Magn Reson Med*, 67(4), pp.1106–1113.

Liu, G. et al., 2013. Nuts and bolts of chemical exchange saturation transfer MRI. *NMR in biomedicine*, 26(7), pp.810–28.

Liu, G. et al., 2009. PARACEST MRI with improved temporal resolution. *Magnetic resonance in medicine*, 61(2), pp.399–408.

Longoni, B. et al., 2010. Mesenchymal stem cells prevent acute rejection and prolong graft function in pancreatic islet transplantation. *Diabetes Technol Ther*, 12(6), pp.435–46.

Lu, Y. et al., 2004. Bioluminescent monitoring of islet graft survival after transplantation. *Molecular Therapy*, 9(3), pp.428–435.

Ludwig, B. et al., 2012. Improvement of islet function in a bioartificial pancreas by enhanced oxygen supply and growth hormone releasing hormone agonist. *Proceedings of the National Academy of Sciences of the United States of America*, 109(13), pp.5022–7.

Luker, G.D. & Luker, K.E., 2008. Optical imaging: current applications and future directions. *Journal of nuclear medicine*, 49(1), pp.1–4.

Major, J. et al., 2007. The synthesis and in vitro testing of a zinc-activated MRI contrast agent. *Proc Natl Acad Sci USA*, 104(35), pp.13881–13886.

Martens, T. et al., 2006. Mesenchymal lineage precursor cells induce vascular network formation in ischemic myocardium. *Nat Clin Pract Cadriovasc Med*, 3, pp.S18-22.

Mc Crimmon, R. & Sherwin, R., 2010. Hypoglycemia in type 1 diabetes. *Diabetes*, 59(10), pp.2333–9.

Meiringeng, Q. et al., 2009. Human Pancreatic Islet Isolation: Part II: Purification and Culture of Human Islets. *J Vis Exp*, 27, p.1343.

Merbach, A., Helm, L. & Toth, E., 2001. The chemistry of the contrast agents in medical magnetic resonance imaging. *Wiley*, ISBN: 978-.

Minteer, D., Marra, K. & Rubin, J., 2013. Adipose-derived mesenchymal stem cells: biology and potential applications. *Adv Biochem Eng Biotechnol*, 129, pp.59–71.

Miranville, A. et al., 2004. Improvement of postnatal neovascularization by human adipose tissue-derived stem cells. *Circulation*, 110(3), pp.349–55.

Moassessfar, S. et al., 2015. A Comparative Analysis of the Safety, Efficacy, and Cost of Islet Versus

Pancreas Transplantation in Nonuremic Patients With Type 1 Diabetes. *American journal of transplantation*, 16(2), pp.518–526.

Moats, R., Fraser, S. & Meade, T., 1997. A "Smart" Magnetic Resonance Imaging Agent That Reports on Specific Enzymatic Activity. *Angewandte Chemie*, 36(7), pp.726–728.

Mutavdžic, D. et al., 2011. Determination of the size of quantum dots by fluorescence spectroscopy. *Analyst*, 136(11), pp.2391–6.

Naziruddin, B. et al., 2014. Evidence for Instant Blood-Mediated Inflammatory Reaction in Clinical Autologous Islet Transplantation. *American journal of transplantation*, 14, pp.428–437.

Nicholls, F.J. et al., 2015. Simultaneous MR imaging for tissue engineering in a rat model of stroke. *Scientific reports*, 5, p.14597.

Nivorozhkin, A., Kolodziej, A. & Caravan, P., 2001. Enzyme-activated Gd(3+) magnetic resonance imaging contrast agents with a prominent receptor-induced magnetization enhancement. *Angew Chem Int Ed Engl*, 40, pp.2093–6.

Ntziachristos, V., 2010. Going deeper than microscopy: the optical imaging frontier in biology. *Nature Methods*, 7, pp.603–614.

Oh, N. & Park, J., 2014. Endocytosis and exocytosis of nanoparticles in mammalian cells. *International journal of nanomedicine*, 9, pp.51–63.

Olokoba, A., Obateru, O. & Olokoba, L., 2012. Type 2 Diabetes Mellitus: A Review of Current Trends. *Oman Medical Journal*, 27(4), pp.269–273.

Park, K. et al., 2010. Trophic molecules derived from human mesenchymal stem cells enhance survival, function, and angiogenesis of isolated islets after transplantation. *Transplantation*, 89(5), pp.509–17.

Park, S.-Y. et al., 2005. Optical imaging of pancreatic beta cells in living mice expressing a mouse insulin I promoter-firefly luciferase transgene. *Genesis*, 43(2), pp.80–6.

Pattou, F., 2010. GLP-1–Receptor Scanning for Imaging of Human Beta Cells Transplanted in Muscle. *The New England journal of medicine*, 363, pp.1289–1290.

Pepper, A.R., Gala-Lopez, B., et al., 2015. A prevascularized subcutaneous device-less site for islet and cellular transplantation. *Nature biotechnology*, 33(5), pp.518–23.

Pepper, A.R., Pawlick, R., et al., 2015. Diabetes Is Reversed in a Murine Model by Marginal Mass Syngeneic Islet Transplantation Using a Subcutaneous Cell Pouch Device. *Transplantation*,

99(11), pp.2294–300.

Pileggi, A. et al., 2006. Reversal of diabetes by pancreatic islet transplantation into a subcutaneous, neovascularized device. *Transplantation*, 81(9), pp.1318–24.

Pill, K. et al., 2015. Vascularization mediated by mesenchymal stem cells from bone marrow and adipose tissue: a comparison. *Cell Regen*, 4(8).

Pongrac, I.M. et al., 2016. Improved biocompatibility and efficient labeling of neural stem cells with poly(L-lysine)-coated maghemite nanoparticles. *Beilstein Journal of Nanotechnology*, 7, pp.926–936.

Pyzdrowski, K. et al., 1992. Preserved insulin secretion and insulin independence in recipients of islet autografts. *The New England journal of medicine*, 327(4), pp.220–6.

Rezende, L. et al., 2007. Ciliary neurothrophic factor promotes survival of neonatal rat islets via BLC-2 anti-apoptotic pathway. *J endocrinol*, 195(1), pp.157–68.

Rheinheimer, J. et al., 2015. Human pancreatic islet transplantation: an update and description of the establishment of a pancreatic islet isolation laboratory. *Arch Endocrinol Metab*, 59(2).

Ribeiro, R.S.G. et al., 2018. Improved Labeling of Pancreatic Islets Using Cationic Magnetoliposomes. *Journal of Personalized Medicine*, 8(1), p.12.

Rice, B.W., Cable, M.D. & Nelson, M.B., 2001. In vivo imaging of light-emitting probes. *Journal of Biomedical Optics*, 6(4), p.432.

Ricordi, C., Lacy, P. & Scharp, D., 1989. Automated islet isolation from human pancreas. *Diabetes*, 38, pp.140–2.

Ruiz-Cabello, J. et al., 2010. Fluorine (19F) MRS and MRI in biomedicine. *NMR in Biomedicine*, 24(2), pp.114–129.

Sakata, N. et al., 2013. Imaging of transplanted islets by positron emission tomography, magnetic resonance imaging, and ultrasonography. *Islets*, 5(5), pp.179–187.

Sakata, N. et al., 2012. Intraoperative ultrasound examination is useful for monitoring transplanted islets. *Islets*, 4(5), pp.339–342.

Sakata, N. et al., 2014. Strategy for clinical setting in intramuscular and subcutaneous islet transplantation. *Diabetes Metab Res Rev*, 30(1), pp.1–10.

Sakata, N. et al., 2011. Utility of co-transplanting mesenchymal stem cells in islet transplantation.

World Journal of Gastroenterology, 17(47), pp.5150–5155.

Saudek, F. et al., 2010. Magnetic Resonance Imaging of Pancreatic Islets Transplanted Into the Liver in Humans. *Transplantation*, 90(12), pp.1602–1606.

Shapiro, A., Pokrywczynska, M. & Ricordi, C., 2017. Clinical pancreatic islet transplantation. *Nat Rev Immunol*, 13(5), pp.268–277.

Shapiro, E. et al., 2007. Antibody-mediated cell labeling of peripheral T cells with micron-sized iron oxide particles (MPIOs) allows single cell detection by MRI. *Contrast Media and Molecular Imaging*, 2(3), pp.147–53.

Shapiro, J.A.M. et al., 2000. Islet transplantation in seven patients with type 1 diabetes mellitus using glucocorticoid-free immunosuppresive regimen. *The New England journal of medicine*, 343(4), pp.230–238.

Schleich, C. et al., 2016. Glycosaminoglycan chemical exchange saturation transfer at 3T MRI in asymptomatic knee joints. *Acta Radiol*, 57(5), pp.627–32.

Smink, A.M. et al., 2017. The Efficacy of a Prevascularized, Retrievable Poly(D,L-lactide-co-ε-caprolactone) Subcutaneous Scaffold as Transplantation Site for Pancreatic Islets. *Transplantation*, 101(4), pp.e112–e119.

Solari, M.G. et al., 2009. Marginal mass islet transplantation with autologous mesenchymal stem cells promotes long-term islet allograft survival and sustained normoglycemia. *Journal of Autoimmunity*, 32(2), pp.116–124.

Solomon, I., 1955. Relaxation process in a system of two spins. *Phys Rev*, 99(559–65).

Speier, S. et al., 2008. Noninvasive in vivo imaging of pancreatic islet cell biology. *Nature Medicine*, 14(5), pp.574–8.

Srinivas, M., Heerschap, A., et al., 2010. (19)F MRI for quantitative in vivo cell tracking. *Trends in biotechnology*, 28(7), pp.363–70.

Srinivas, M., Cruz, L., et al., 2010. Customizable, multi-functional fluorocarbon nanoparticles for quantitative in vivo imaging using 19F MRI and optical imaging. *Biomaterials*, 31(27), pp.7070–7077.

Srinivas, M. et al., 2007. Fluorine-19 MRI for Visualization and Quantification of Cell Migration in a Diabetes Model. *Magnetic Resonance in Medicine*, 58(4), pp.725–734.

Srinivas, M. et al., 2012. Labeling cells for in vivo tracking using (19)F MRI. *Biomaterials*, 33(34),

pp.8830–40.

Srinivas, M. et al., 2015. PLGA-encapsulated perfluorocarbon nanoparticles for simultaneous visualization of distinct cell populations by 19F MRI. *Nanomedicine*, 10(15), pp.2339–48.

Sun, P., Farra, C. & Sorensen, A., 2007. Correction for artifacts induced by B0 and B1 field inhomogeneities in pH-sensitive chemical exchange saturation transfer (CEST) imaging. *Magnet Reson Med*, 58(6), pp.1207–1215.

Sunderkötter, C. et al., 1994. Macrophages and angiogenesis. *J Leukoc Biol*, 55(3), pp.410–22.

Swider, E. et al., 2018. Design of triphasic poly(lactic-co-glycolic acid) nanoparticles containing a perfluorocarbon phase for biomedical applications. *RSC Adv.*, 8(12), pp.6460–6470.

Tai, J. et al., 2006. Imaging islets labeled with magnetic nanoparticles at 1.5 Tesla. *Diabetes*, 55(11), pp.2931–2938.

Tang, Y.L. et al., 2004. Autologous mesenchymal stem cell transplantation induce VEGF and neovascularization in ischemic myocardium. *Regulatory Peptides*, 117(1), pp.3–10.

Terreno, E. et al., 2006. Effect of the intracellular localization of a Gd-based imaging probe on the relaxation enhancement of water protons. *Magnetic resonance in medicine*, 55(3), pp.491–7.

Terrovitis, J. et al., 2008. Magnetic resonance imaging overestimates ferumoxide-labeled stem cell survival after transplantation in the heart. *Circulation*, 117(12), pp.1555–1562.

Toso, C. et al., 2008. Clinical magnetic resonance imaging of pancreatic islet grafts after iron nanoparticle labeling. *American journal of transplantation*, 8(3), pp.701–6.

Tsourkas, A. & Josephson, L., 2010. Magnetic Nanoparticles. *Molecular Imaging: Principles and practice*, ISBN-13 97, pp.523–541.

Vaithilinqam, V., 2011. Islet transplantation and encapsulation: an update on recent developments. *The rewiev of diabetic studies*, 8(1), pp.51–67.

Vargas, E. & Chen, J., 2010. Magnetic Resonance Imaging Agents. In *Molecular Imaging: Principles and practice*. pp. 389–404.

Wang, J. et al., 2016. Magnetic Resonance Imaging of Glucose Uptake and Metabolism in Patients with Head and Neck Cancer. *Scientific reports*, 6(30618).

Wang, P. et al., 2014. GLP-1R–Targeting Magnetic Nanoparticles for Pancreatic Islet Imaging. *Diabetes*, 63(5), pp.1465–1474.

Weissleder, R., 2002. Scaling down imaging: molecular mapping of cancer in mice. *Nature Reviews Cancer*, 2(1), pp.1–8.

Wolf, U., 2006. Subsecond fluorine-19 MRI of the lung. *Magn Reson Med*, 55(4), pp.948–51.

Wolf, W., Presant, C. & Waluch, V., 2000. 19F-MRS studies of fluorinated drugs in humans. *Adv Drug Deliv Rev*, 41(1), pp.55–74.

Yuan, B., Chen, N. & Zhu, Q., 2004. Emission and absorption properties of indocyanine green in Intralipid solution. *J Biomed Opt*, 9, pp.497–503.

Zhou, J. et al., 2004. Quantitative description of proton exchange processes between water and endogenous and exogenous agents for WEX, CEST, and APT experiments. *Magn Reson Med*, 51(5), pp.945–952.

van Zijl, P.C.M. & Yadav, N.N., 2011. Chemical Exchange Saturation Transfer (CEST): what is in a name and what isn't? *Magnetic Resonance in Medicine*, 65(4), pp.927–948.